LASER INTERFEROMETRIC INVESTIGATION OF MICROLAYER EVAPORATION FOR VARIOUS LEVELS OF SUBCOOLING AND HEAT FLUX

LASER INTERFEROMETRIC INVESTIGATION OF MICROLAYER EVAPORATION FOR VARIOUS LEVELS OF SUBCOOLING AND HEAT FLUX

by

COSMOS M. VOUTSINOS B.Sc. (ENG.)

A Thesis

submitted to the School of Graduate Studies
in partial fulfillment of the requirements
for the degree

Master of Engineering
McMaster University

March 1976

TO DONNA

MASTER OF ENGINEERING
(Mechanical Engineering)

McMASTER UNIVERSITY
Hamilton, Ontario

TITLE : Laser Interferometric Investigation of Microlayer Evaporation for Various Levels of Subcooling and Heat Flux

AUTHOR : COSMOS M. VOUTSINOS
B.Sc. (Mech. Eng.)
(University of Waterloo, Ontario, Canada)

SUPERVISOR : Dr. Ross L. Judd

NUMBER OF PAGES : 116

SCOPE AND CONTENTS :

An experimental study of the growth and evaporation of the microlayer, underlying a bubble during nucleate boiling heat transfer to dichloromethane, is presented. The influence of heat flux (8000 Btu/hr ft^2 - 20,000 Btu/hr ft^2) and subcooling (0^oF - 13.5^oF) upon the rates of growth and evaporation, have been studied using laser interferometry and high speed photography through the glass heater surface on which bubbles were nucleated.

The results presented indicate that the microlayer thickness is of the order of 5 μm. The analysis of these results confirms that the microlayer evaporation phenomenon is a significant heat transfer mechanism representing approximately 25% of the total nucleate boiling heat transfer rate for the conditions investigated.

As subcooling is increased from saturation, the contribution of the microlayer evaporation to the total heat transfer rate varies in accordance with two interacting processes in the region investigated. This variation appears as an initial decrease followed by an increase.

TABLE OF CONTENTS

ACKNOWLEDGEMENTS

The author gratefully acknowledges the assistance of Professor Ross L. Judd, who provided guidance and advice in planning and performing the research investigation.

The author also expresses his appreciation to Professors J.H.T. Wade, J. N. Siddall and J.V. Vlachopoulos for their interest and cooperation in serving as members of the Committee.

Special thanks are due to Mr. Thomas Efthimiopoulos who assisted in the design of the apparatus.

The financial support of the National Research Council is gratefully acknowledged.

LIST OF FIGURES

LIST OF TABLES

LIST OF APPENDICES

NOMENCLATURE

A = area

C_ℓ = specific heat of liquid

D = diameter

d = microlayer thickness

E = supplied voltage

F = average number of frames between bubble emission

f = frequency of bubble emmission

Gr = Grashof number

h_{fg} = latent heat

I = supplied current

I_i = intensity of reflected light from i^{th} surface

L = total film length

m = number of fringe

N = number of active sites

Nu = Nusselt number

N/A = active site density

n = average number of frames

n_i = refractive index of i^{th} component

P_{sat} = saturation pressure

Q = power supplied (3.414EI)

q_E = heat transferred by microlayer evaporation

q_{Loss} = heat lost

q_T = total heat transferred

q/A = heat flux

$R(t)$	=	bubble radius
r	=	bubble radius
r_i	=	reflectivity of i^{th} surface
$\bar{T}$	=	average time elapsed between bubbles (F $\bar{t}$)
T_{sat}	=	saturation temperature
T_w	=	temperature of heater surface
T_∞	=	liquid bulk temperature
$(T_w - T_{sat})$	=	superheat
$(T_{sat} - T_\infty)$	=	subcooling
t	=	time
$\bar{t}$	=	average time per frame
V_E	=	evaporated microlayer volumes
v	=	frequency of film markings

<u>GREEK LETTERS</u>

β	=	bulk modulus
$\delta_o(r)$	=	initial microlayer thickness
$\delta(r, t)$	=	instantaneous microlayer thickness
η	=	total film markings
θ	=	angle of incidence
λ	=	laser wavelength
μ	=	viscosity of liquid
ν_ℓ	=	kinematic viscosity of liquid
ρ_ℓ	=	density of liquid
τ	=	departure time
Φ	=	bubble flux density

CHAPTER I

CHAPTER I

INTRODUCTION

A. Purpose

Nucleate boiling is a complex heat transfer phenomenon that has been the subject of many publications in the last 25 years. Any interpretation of this phenomenon must be capable of explaining the abrupt increase in heat flux observed when boiling begins and many models have been postulated to predict the nucleate boiling heat transfer rate. None, however, has proven sufficient especially at significant levels of subcooling (1). The heat transfer mechanisms that have formed the basic blocks of some of these models are the following :

1) Latent Heat Transport during which a bubble absorbs energy equivalent to one bubble volume of vapour. As this bubble disconnects itself from the heater surface it transports along the latent heat it contains as seen in Figure 1A. Where nucleation is not present, energy is transferred from the surface by natural convection as seen in Figure 1B.

2) Bubble Agitation during which fluid mixing occurs near the heated surface by the presence, growth and departure of bubbles. Three bubbles are seen in Figure 1A. Their fast growth displaces the fluid and causes microconvection currents which enhance the heat transfer.

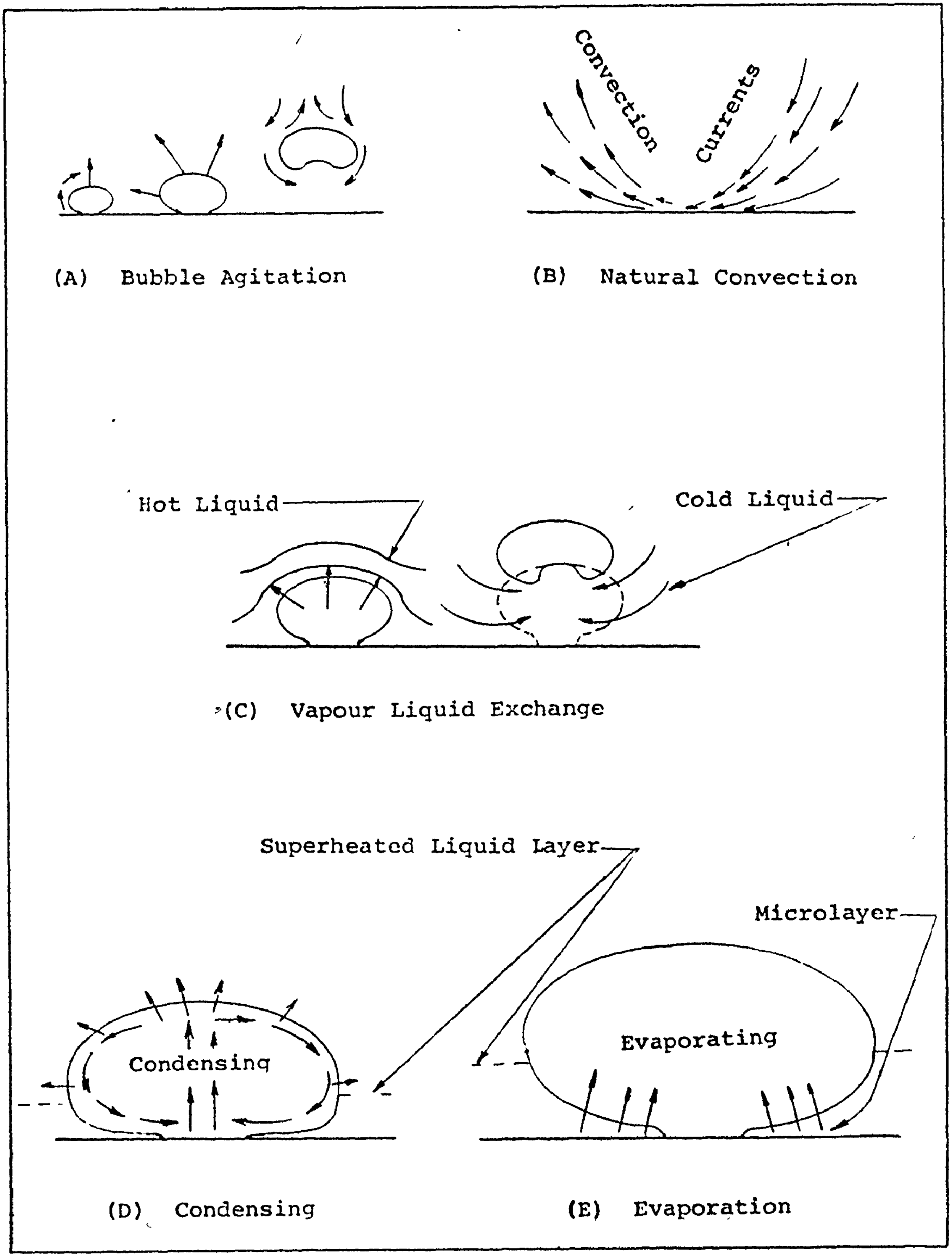

Figure 1. SCHEMATIC DIAGRAM OF HEAT TRANSFER MECHANISMS.

3) Vapour-Liquid Exchange during which liquid equivalent to one bubble volume picks up heat from the heater surface and is transported away while colder liquid replaces an equal volume adjacent to the wall. Figure 1C shows the cold liquid rushing toward the heater surface in order to replace the departing volume.

4) Condensing Action during which vapour currents inside the bubble condenses at the vapour-liquid interface, thus transferring heat into the bulk of the liquid (Figure 1D). This mechanism has not been proven as yet; however, it appears to be very reasonable.

5) Microlayer Evaporation by which energy is transferred away from the heated surface into the bubble by evaporation of a thin layer of superheated liquid underneath the bubble (Figure 1E). Considerable evidence is produced in the present research about the role of this heat transfer mechanism, and is discussed further.

Additional and as yet unknown mechanisms contributing to the nucleate boiling heat transfer may exist. However, the significance of microlayer evaporation is becoming increasingly important in recent years. This mechanism relates the evaporative process at the base of the bubble with the bubble growth and its omission is thought to be the possible explanation of the deficiency of the existing models. The purpose of the present investigation is to present an experimental study of the microlayer evaporation phenomenon in which the rates of evaporation and heat transfer for various levels of subcooling and heat flux were determined.

B. Literature Survey

The concept of evaporation of a thin layer of liquid at the base of the bubble is based on the existence of a thin liquid layer. Such an assumption was originally made by Snyder and Edwards (2). Until that time, the usual hypothesis of nucleate boiling was that the bubble agitates the liquid thus promoting the increase in heat transfer. Moore and Mesler (3) were the first to obtain indirect evidence of the existence of the microlayer underneath the bubble. In their experiments, they recorded the rapid fluctuations in the temperature of the surface on which nucleate boiling was occurring. Their observations could not be explained in terms of the bubble agitation model. The only hypothesis that appeared to be consistent was the one by Snyder and Edwards which proposed vapourization at the base of the bubble. Hendricks and Sharp (4) provided a confirmation of these hypotheses by correlating high speed photographic data with surface temperature - time profiles under the growing bubble. With similar techniques, Rogers and Messler (5) also managed to show that the large temperature drop noted by Moore and Messler occurred when the perimeter of the bubble base passes over the thermocouple junction.

A more direct evidence of the microlayer existence during nucleate boiling was originally provided by Sharp (6), who used interferometry to record the evaporation and dry out of a thin film of liquid at the base of each bubble. Shortly after, the microlayer thickness $\delta_o(r)$ was deduced by Cooper and Lloyd (7) who performed simultaneous measurements of temperature fluctuations at various points over which a bubble was allowed to grow. From these temperature variations, Cooper and Lloyd were able to deduce the local enthalpy extraction at the location of each of the thermometers. Their main conclusion was that $\delta_o(r)$ is of the order of 10 micrometers for toluene and isopropyl alcohol . They also obtained indication that the radius of the evaporated volume of the microlayer is about half the maximum radius of the bubble. Jawurek (8) performed a photographic investigation based on the destructive interference patterns between reflections of the vapour-liquid interface beneath the bubble and the heated glass surface on which nucleate boiling occurred and determined that for boiling methanol, the microlayer thickness $\delta(r, t)$ was no more than 1 micrometer.

Several additional experiments and mathematical models were presented, based on the above investigations. One of these models describing the transient temperature of a heater surface as dictated by the evaporation of a liquid microlayer was derived by Dzakowic and Frost (9). Although this mathematical model was based on the assumption that the liquid microlayer temperature is always uniform and equal to the heater surface temperature, it appears to be in agreement with the experimental data obtained by Moore and Messler. Another analytical prediction of the size and shape of the microlayer was presented by Olander and Watts (10). This mathematical model was based on the solution of the boundary layer momentum and continuity equations. Their results indicate that $\tilde{\delta}_o(r)$ varies linearly with radial position.

Copper and Lloyd (11) presented an empirical correlation which predicts that the thickness of the microlayer $\tilde{\delta}_o(r)$ is $0.8\sqrt{\nu t}$ where "t" is the time required for the bubble to grow to radius r. This correlation was supported by experimental data based on observations of the growth and departure of individual vapour bubbles and on temperature measurements of the solid surface beneath it. Another model for bubble dynamics in nucleate boiling was derived by Robin and Snyder (12). Based on the assumption of mass transfer through the growing bubble, they derived a second order unsteady partial differential equation. This equation was solved with numerical approximation and provided reasonable results.

More recently, Judd and Merte (1) presented experimental results by which they were able to test several of the existing models for various levels of subcooling and acceleration. There was indication that none of the basic models could adequately predict nucleate boiling heat flux for other than saturated boiling conditions and at standard gravity. All of the models predicted a decreasing value of heat flux as subcooling and acceleration increased. This observation was given the interpretation that some additional mechanism may exist that would be inoperative under saturated boiling conditions, but very sensitive to the level of subcooling. Microlayer evaporation might well be the missing mechanism.

CHAPTER II

CHAPTER II

EXPERIMENTAL APPARATUS

A. Introduction

The design specifications of the apparatus were dictated by the experimental requirements which included the investigation of the microlayer thickness $\delta(r, t)$ as a function of radius and time at various levels of liquid temperature and heat flux. The precision required however, in measuring the microlayer thickness was very important; firstly, because the magnitude of change that might take place by varying the heat flux or the level of subcooling was not known and secondly, because the thickness data were to be used for the determination of the total volume of liquid evaporated from the microlayer during nucleate boiling for all the above conditions. The latter would be used to determine the significance of heat transfer by microlayer evaporation.

An interferometric investigation was to be used in order to obtain the microlayer thickness measurements, similar to the investigation undertaken by Jawurek. However, it was decided that in order to obtain a higher precision, the illuminating source used in the interferometer should have the highest possible spectral purity. A Helium-Neon laser was used to illuminate the microlayer through a glass heater surface on which nucleate boiling was taking place. Figure 2 shows the difference in spectral purity among white light, monochromatic light and laser light. The use of the laser light source dictated that all the surfaces of the specimens, prisms, and lens should be coated with antireflective coating with an exception of the ones which were needed to reflect. In this manner, the unnecessary interference patterns were eliminated leaving a very clear image of the interference fringes resulting from the presence of the microlayer thickness.

In addition, the experiment required the ability to be able to vary the amount of heat supplied and the liquid temperature independently using an appropriate liquid selected so that it would boil at temperatures that would provide safe experimental conditions and yield reasonable sized bubbles which could be readily analysed photographically.

B. Test Assembly

An existing test assembly described in Reference (14) was modified in accordance with the special requirements of the present investigation.

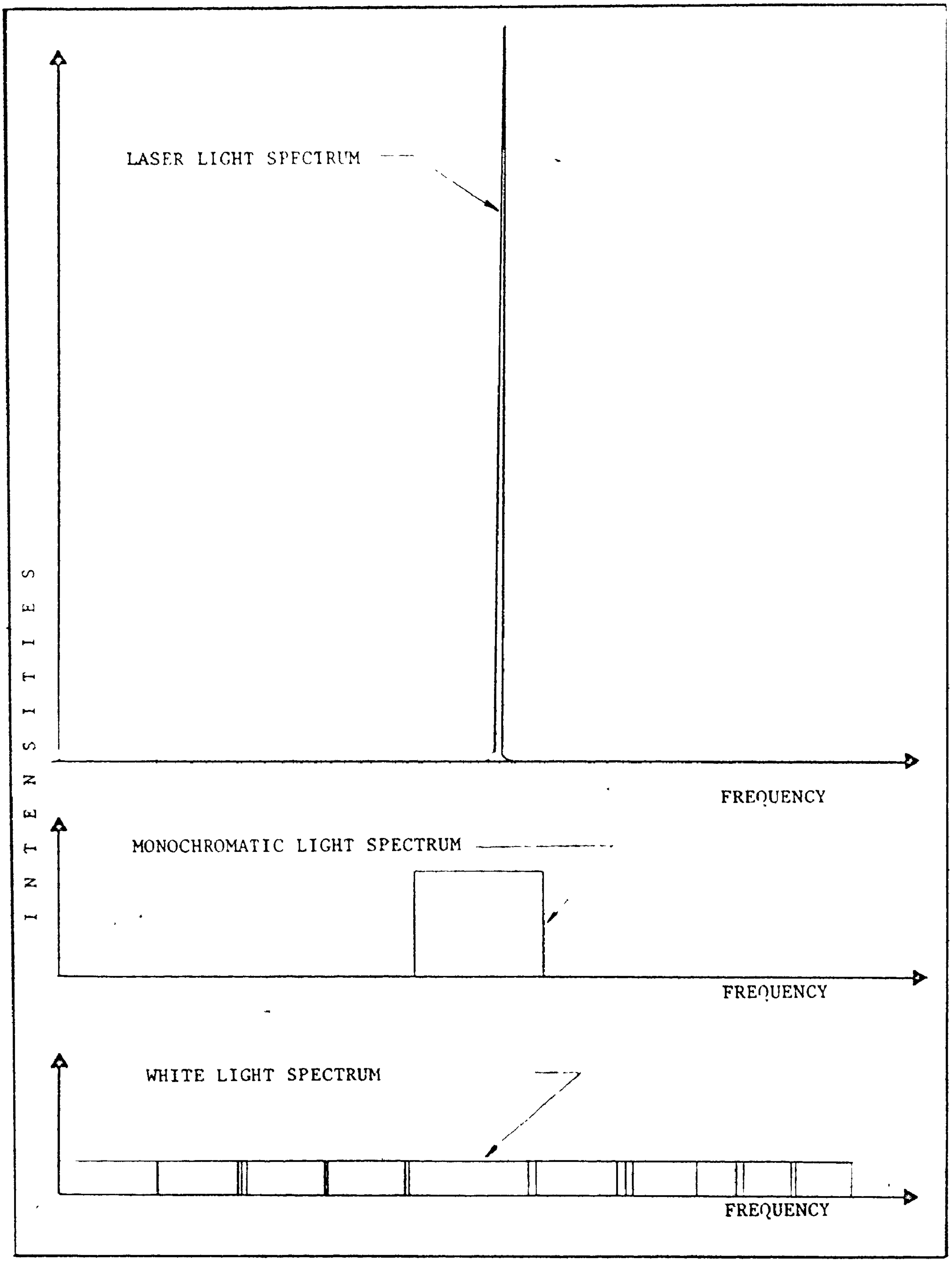

Figure 2. LIGHT SPECTRA

It provided a test platform on which the specimens could be mounted in a controlled environment in which nucleate boiling tests could be performed. Figure 3 is a detailed drawing and Figure 4 is a photograph of the test assembly.

The basic component of the assembly was a test vessel which was constructed on a 6" diameter type 304 stainless steel pipe. This pipe formed the side walls of the vessel which had machined flanges of the same material resting on gaskets at each end. The upper flange contained threaded holes for the bus-bars, the subcooling coil, the condenser coil, the pressure control system (vacuum), and the thermocouples. Eight tie down bolts connected the upper flange (cover plate) to the lower flange (base plate) and provided vacuum tight seals.

The fluid tested was dichloromethane (methylene/chloride) which was boiled on a borosilicate glass heater surface coated with a half wavelength thickness of stannic oxide which conducted electric current and generated the required heat for boiling. This glass heater specimen was arranged within the test assembly on the base plate of the vessel in order to ensure normal axes of observation of the nucleate boiling phenomenon as required by the research investigation. The oxide coated surface of the specimen was in contact with the dichloromethane, while the other surface was coated with one quarter wavelength thickness of antireflective coating for He-Ne laser light and it was exposed to the air.

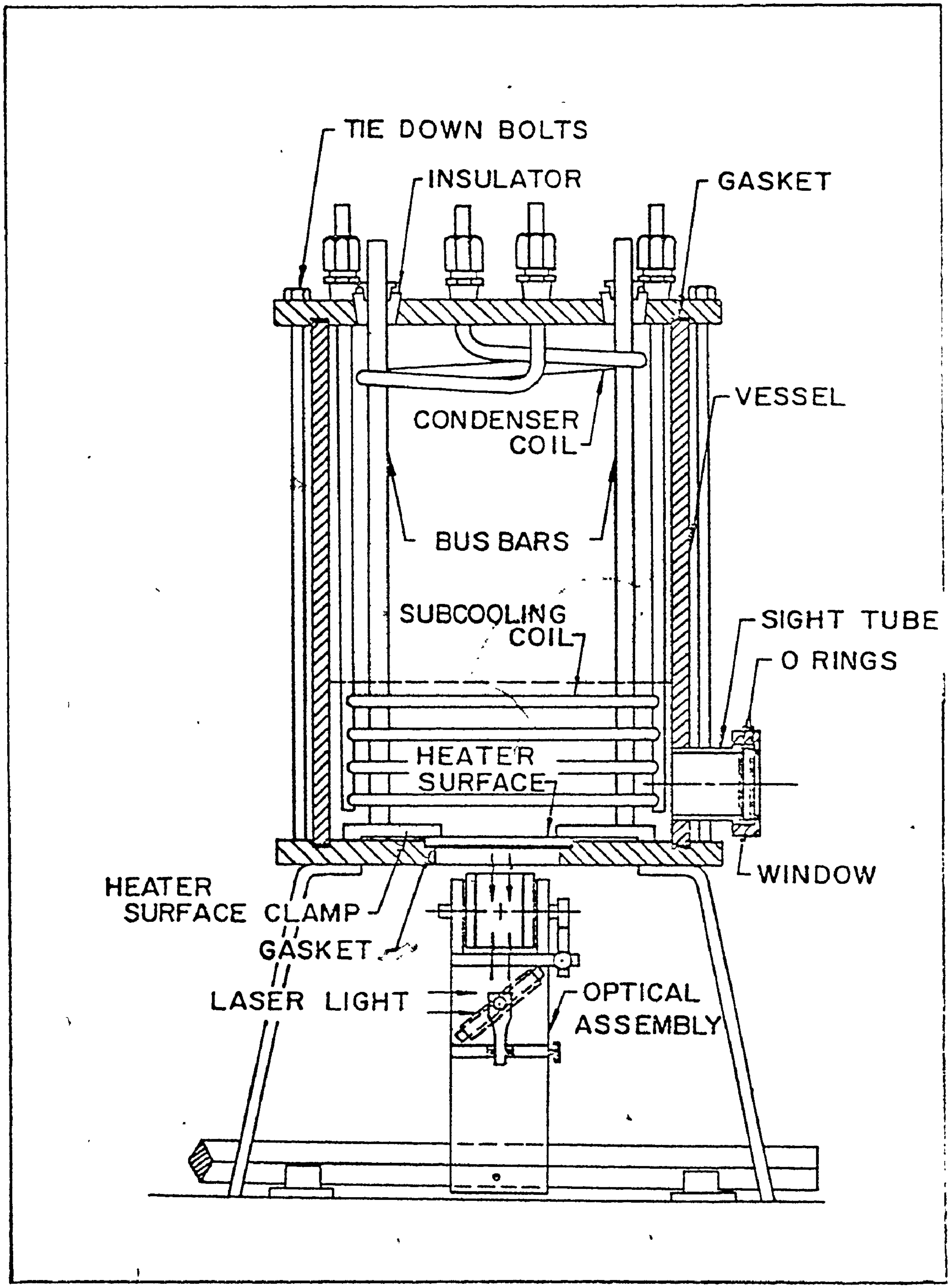

Figure 3. DETAIL DRAWING OF THE TEST ASSEMBLY

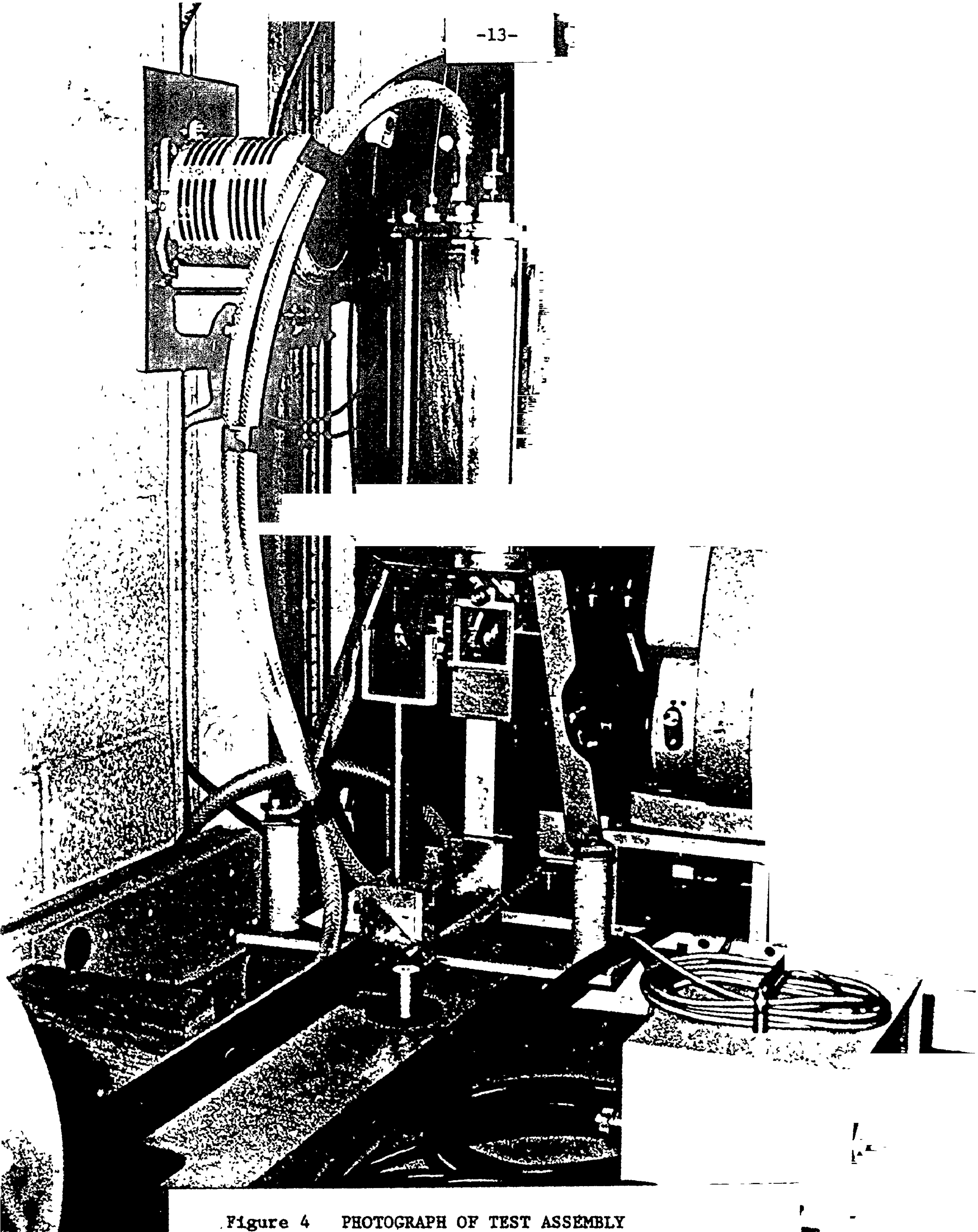

Figure 4 PHOTOGRAPH OF TEST ASSEMBLY

Figure 5 shows the details of one specimen of the oxide film heater surface. Each one was cut to size 2 7/16" x 1 5/16" ± 1/32" from sheets of 1/8" thick oxide coated borosilicate glass and after the corners were rounded to 1/8" radius. A layer of metallic silver was deposited on each end leaving an effective heat transfer surface of 2" x 1 5/16" ± 1/32". The silver bands facilitated the electrical contact between the bus-bars and the oxide coating. Since it was not possible to evaluate local heat flux values, it had to be assumed that the oxide coating had been deposited uniformly and that the heat was generated uniformly over the heat transfer surface. Judd (13) discussed this assumption in his doctoral thesis and found it to be quite reasonable. Since boiling occurred at randomly located nucleation sites in the oxide coating, it was also assumed that any 1mm x 1mm square of heater surface should contain the same number of nucleation sites.

At the base of the cylindrical test assembly an optical sight tube 2 1/2" diameter of stainless steel pipe was provided. A Viton "O" ring set in an internal groove formed the seal between the sight tube wall and the observation glass window.

The requirements of the research investigation dictated that subcooling be varied at constant pressure. This variation

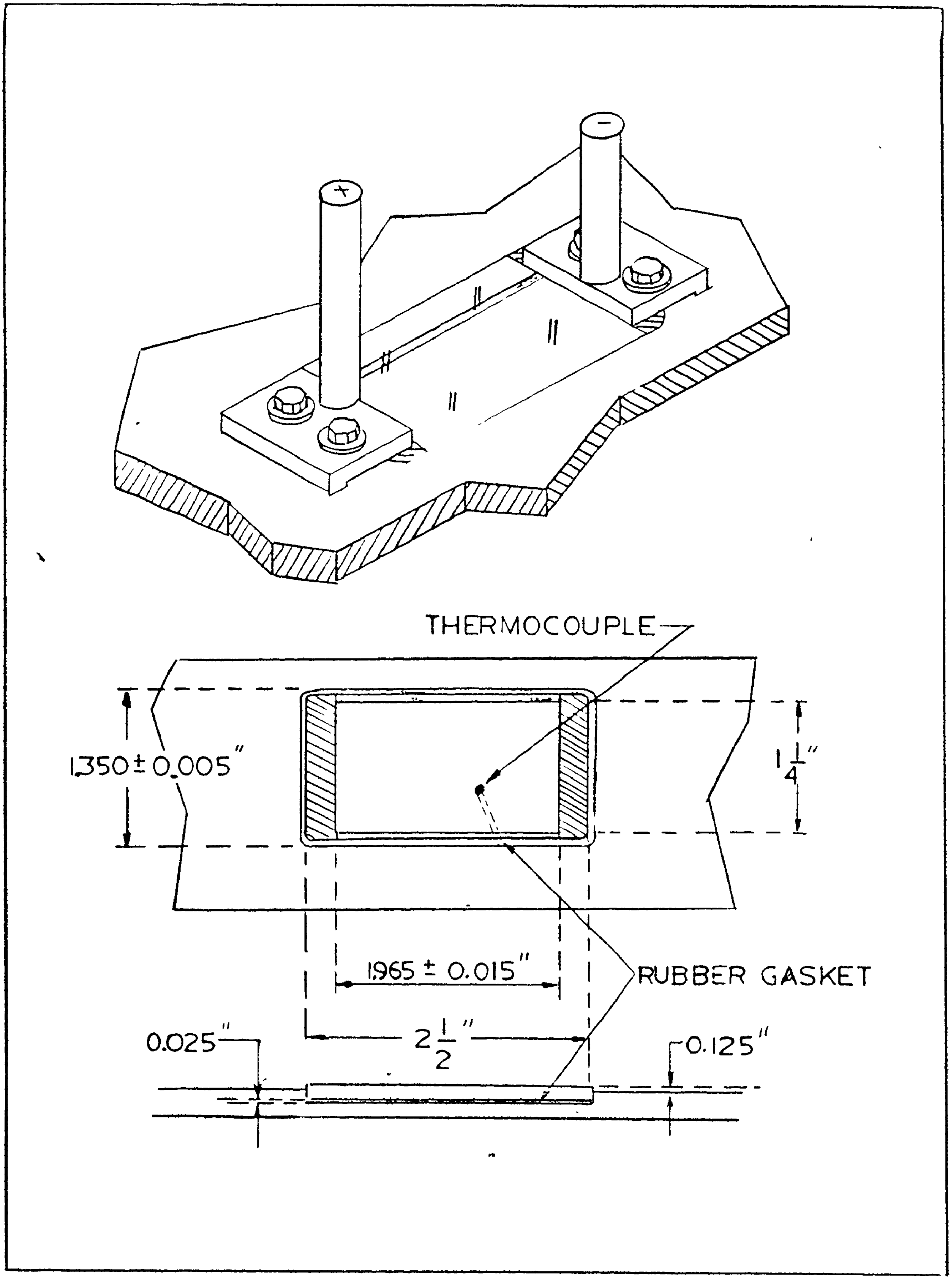

Figure 5.. SPECIMEN OF HEATER SURFACE

could only be accomplished by changing the temperature of the test fluid which was accomplished with a single pass heat exchanger shown in Figure 6, constructed as an integral part of the internal components of the test assembly. The tubes were bent into a hollow form providing clearance for the bus-bars (electrical conductors).

A vapour condenser was mounted 1 1/2" beneath the top flange in order to condense the vapour formed during testing. The vapour condenser was constructed of 1/4" diameter stainless steel tubing wound in a spiral fashion. A reflux condenser was constructed outside of the test vessel along the line that draws vacuum in the test assembly. The two vapour condensers and the subcooling heat exchanger were connected in parallel with valves installed for purposes of controlling the relative flow rates. The vapour condensers are shown in Figure 7.

C. Power Supply

The power supply which furnished power to the coated glass surface (test specimen) was comprised of six 12 volt DC batteries which could be connected either in series or parallel by means of various knife switches. Finer voltage control was achieved through a large rheostat connected in series between the bank of batteries and the heater surface in the test vessel. This source provided a very steady

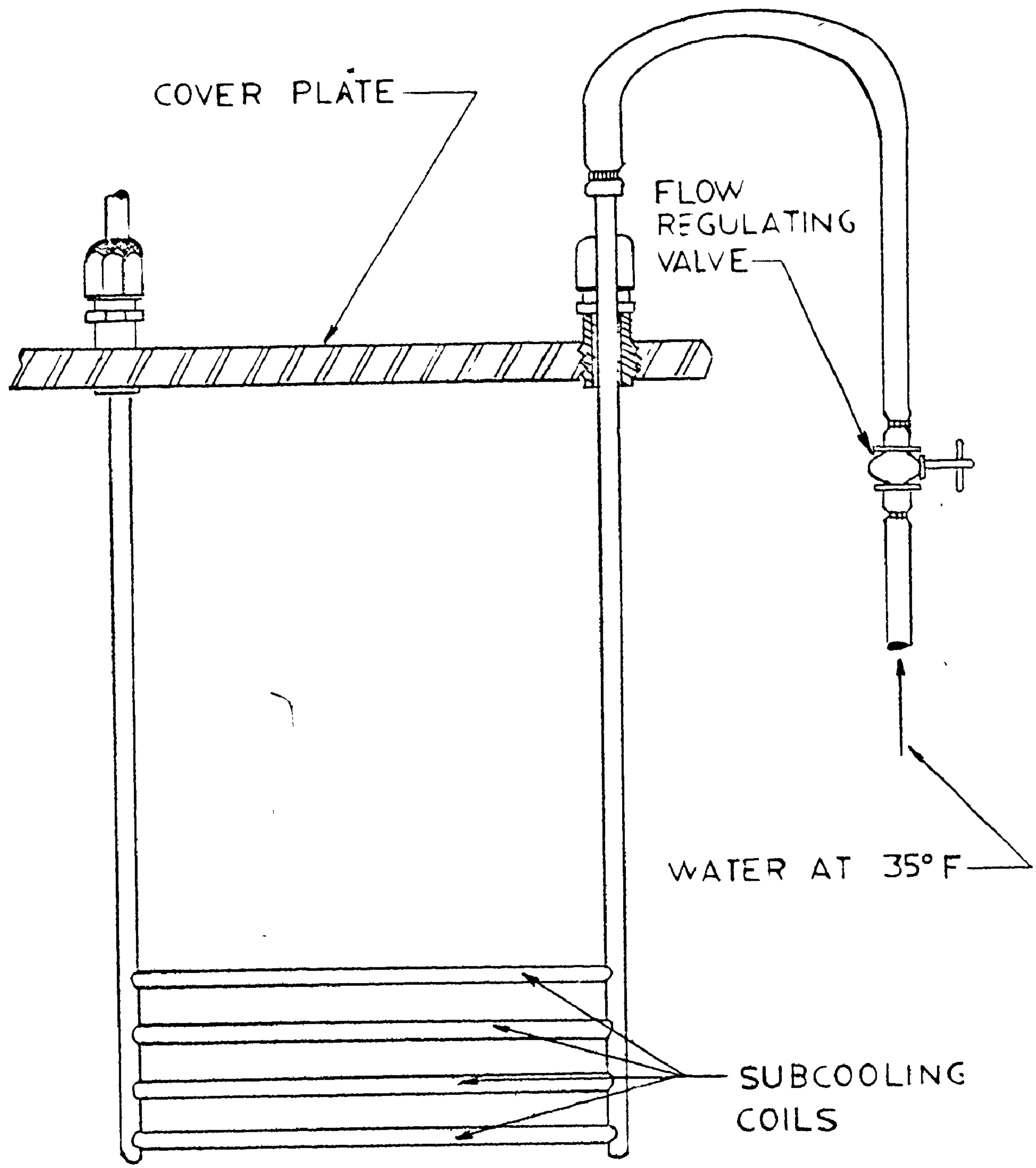
COVER PLATE
FLOW
REGULATING
VALVE
WATER AT 35° F
SUBCOOLING
COILS

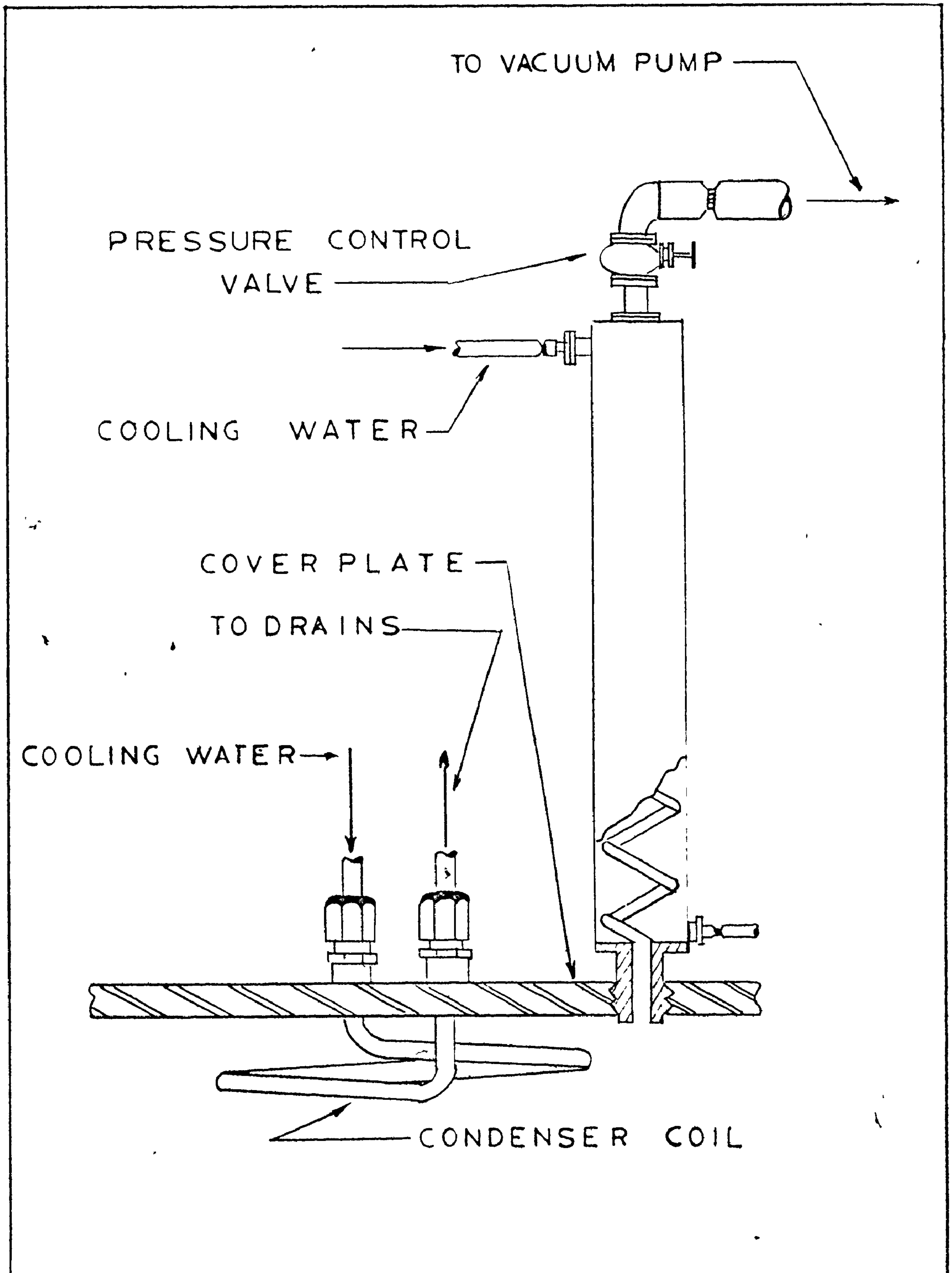
TO VACUUM PUMP
PRESSURE CONTROL VALVE
COOLING WATER
COVER PLATE
TO DRAINS
COOLING WATER
CONDENSER COIL

power ranging from 0 to 72 volts. The power flow to the heater was continuously monitored by means of a voltmeter and an ammeter mounted on the power supply shown in Figure 8.

D. Pressure Control

In order to maintain a constant saturation temperature at the heat transfer surface throughout the research investigation, the pressure inside the test vessel had to remain constant. During each experiment, comprised of a number of tests at different levels of heat flux and degrees of subcooling, the pressure in the test vessel was maintained constant at approximately 1/2 atmosphere, in order to decrease the number of active nucleation sites and to increase the size of the vapour bubbles, thereby simplifying the photographic analysis. Subatmospheric pressure was achieved with an Edwards rotary vacuum pump and an atmospheric bleed valve which enabled the pressure in the vessel to be adjusted to a predetermined value. The pressure control was achieved manually with a Nupro fine threaded metering valve which was installed on the cover plate of the test vessel and the pressure was continuously monitored by a mercury manometer. Although such a pressure control appears very difficult, it proved to be quite satisfactory. Before each test, power was supplied to the heater surface in order to initiate boiling. The pressure control valve then

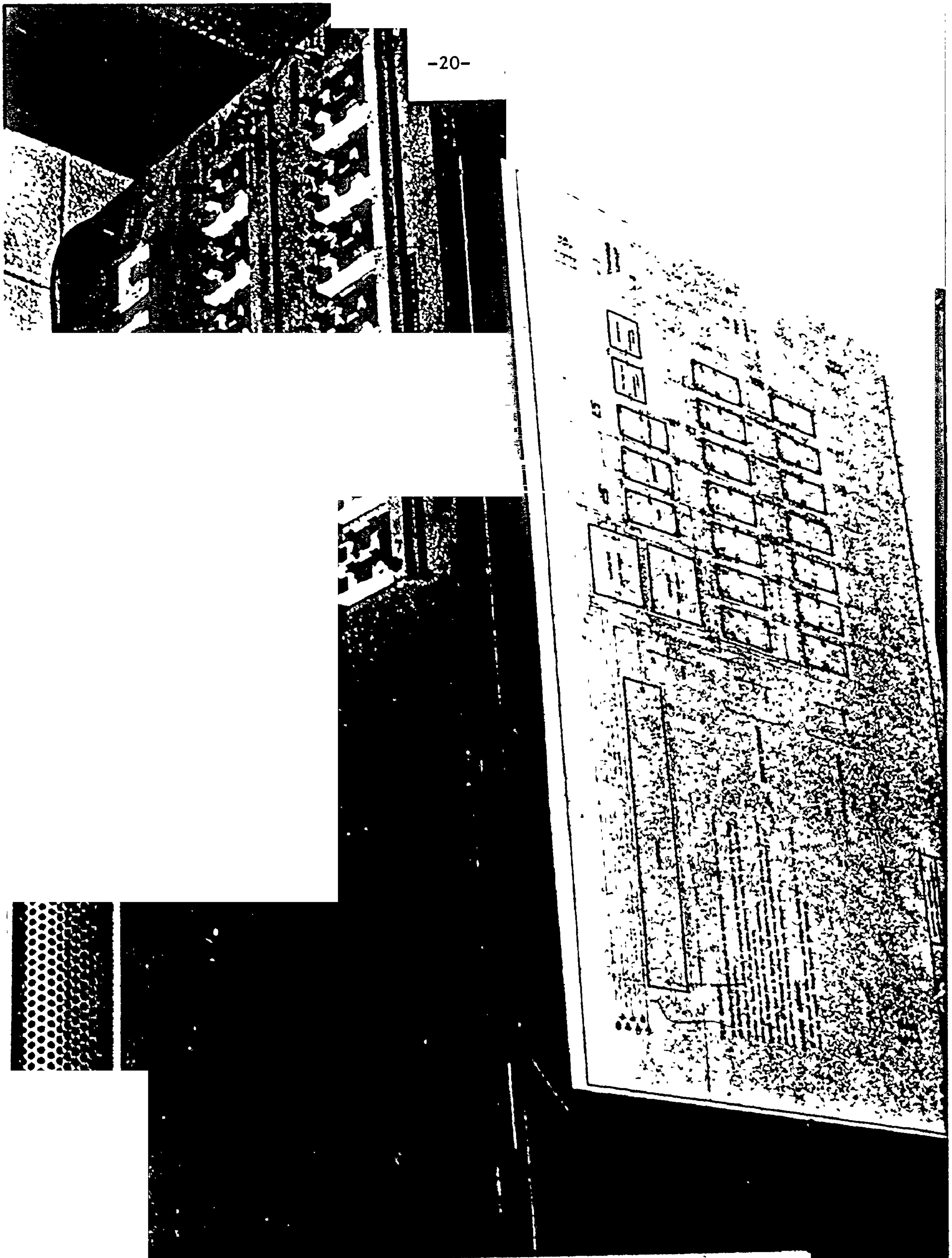

Figure 8 PHOTOGRAPH OF POWER SUPPLY

was manually adjusted to the desired level. As the system reached equilibrium the adjustments became finer and finer to the point that the pressure reading on the mercury monometer remained visually unchanged.

E. Temperature Measuring System

Four chromel - constantan thermocouples were used in the present investigation. Three of them were used to measure the bulk liquid temperature and the other one was used to measure the temperature of the heater surface. Figure 9 shows a photograph of the temperature measuring system. Each of the three thermocouples measuring the bulk liquid temperature was a Thermoelectric "Ceramo" thermocouple mounted in the cover plate, while the one measuring the heater surface temperature was "epoxied" on the underside of the heater plate. Chromel - constantan thermocouples were selected for their E.M.F. characteristic which is 36 microvolts/^{o}F. Their output signals were fed into a switch box from which each output signal could be directed either to a high resolution Guildline potentiometer or to a Minneapolis Honeywell recorder. The E.M.F. produced by each of the thermocouples was individually converted into temperature in degrees Fahrenheit by the use of a conversion table published by the National Bureau of Standards (15).

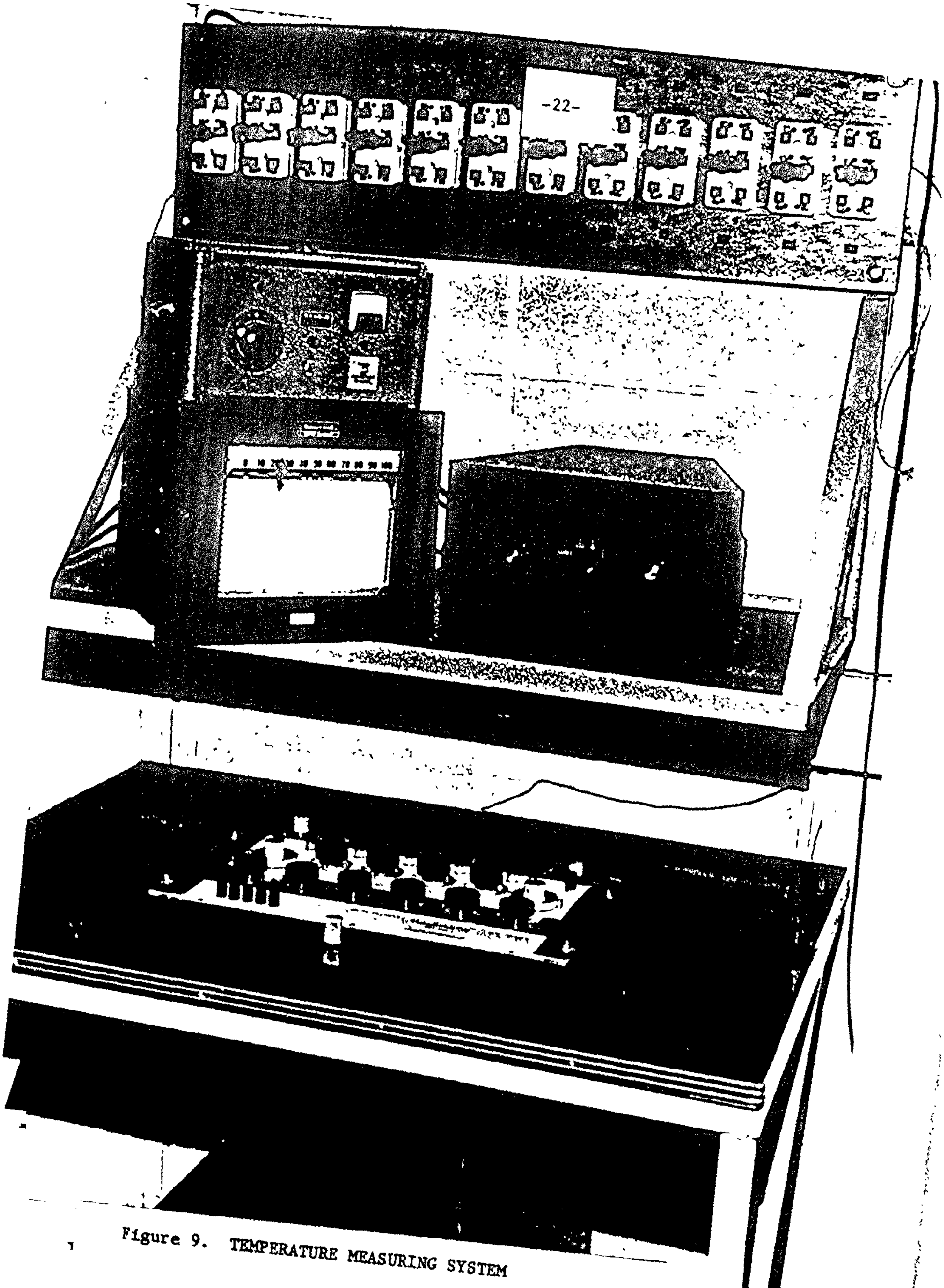

Figure 9. TEMPERATURE MEASURING SYSTEM

F. Optical System

An existing optical system was modified to accept a SPECTRA PHYSICS Helium-Neon laser (model 125A, λ = 0.6328 micrometers). This laser was specified by the manufacturer to produce a highly monochromatic beam at 50 mW; however, its actual power was measured directly using three different photocells and was found to be 62.5 mW.

A schematic diagram of the modified system is presented in Figures 10 and 11. The light emitted by the laser was reflected by a first surface mirror through two collimating lenses which together enlarged the beam diameter tenfold. The focal lengths of these lenses were selected to be as large as the available space allowed, in order to reduce the amount of light dispersion and ensure a parallel ray beam at the beginning of the interferometer. Both surfaces of each of these lenses were coated with 1/4 wavelength antireflective coating. The parallel, coherent, and highly monochromatic beam of light was then directed upward in the interferometer by means of a first surface mirror located beneath the heater surface of the test vessel.

Figure 10 shows the two schematic views of the interferometer and the schematics of the light path in it. After the light was deflected upward from the front surface mirror, it passed first through a rhomboidal prism and then through the

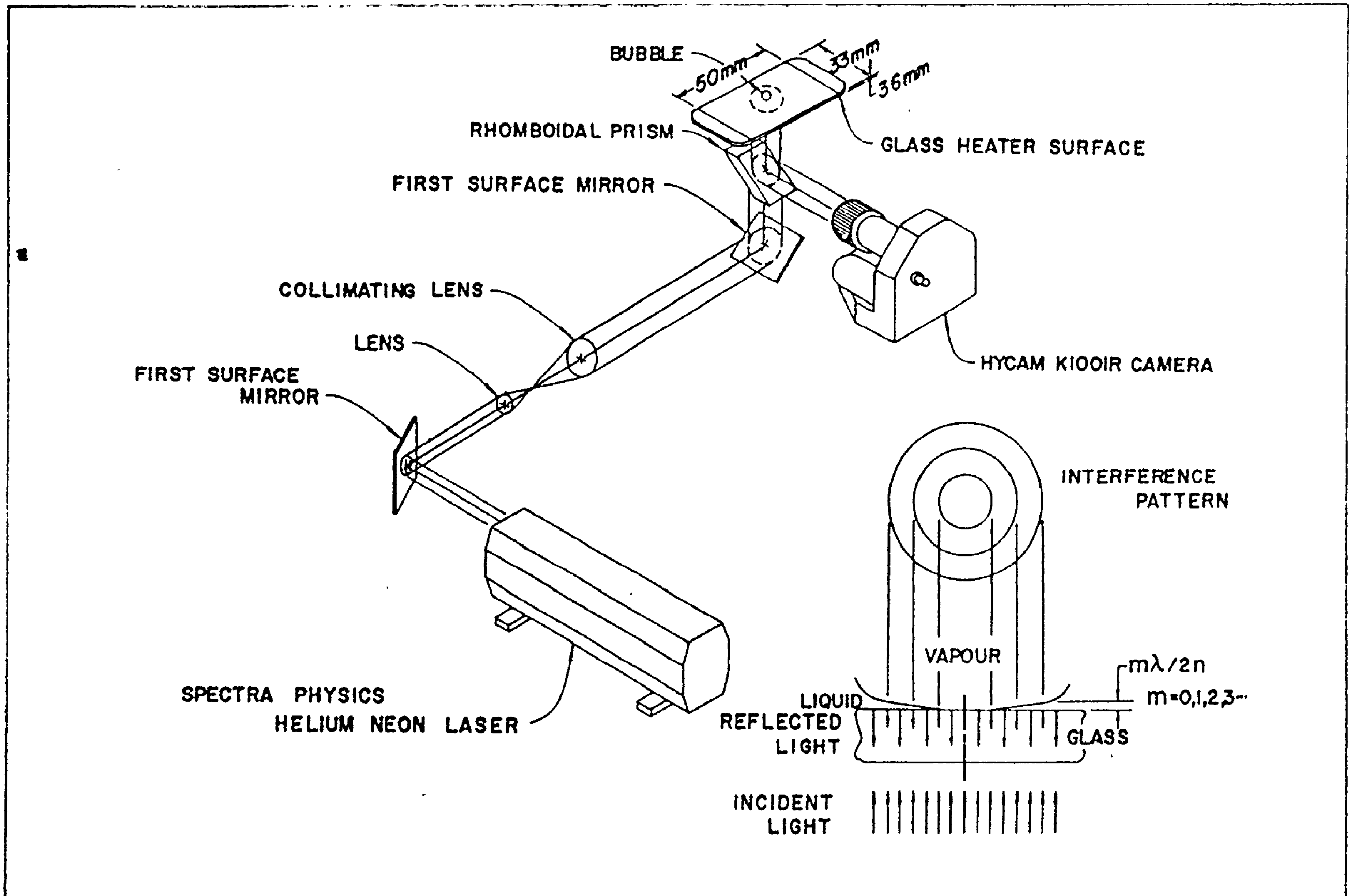

Figure 10. SCHEMATIC OF THE OPTICAL SYSTEM

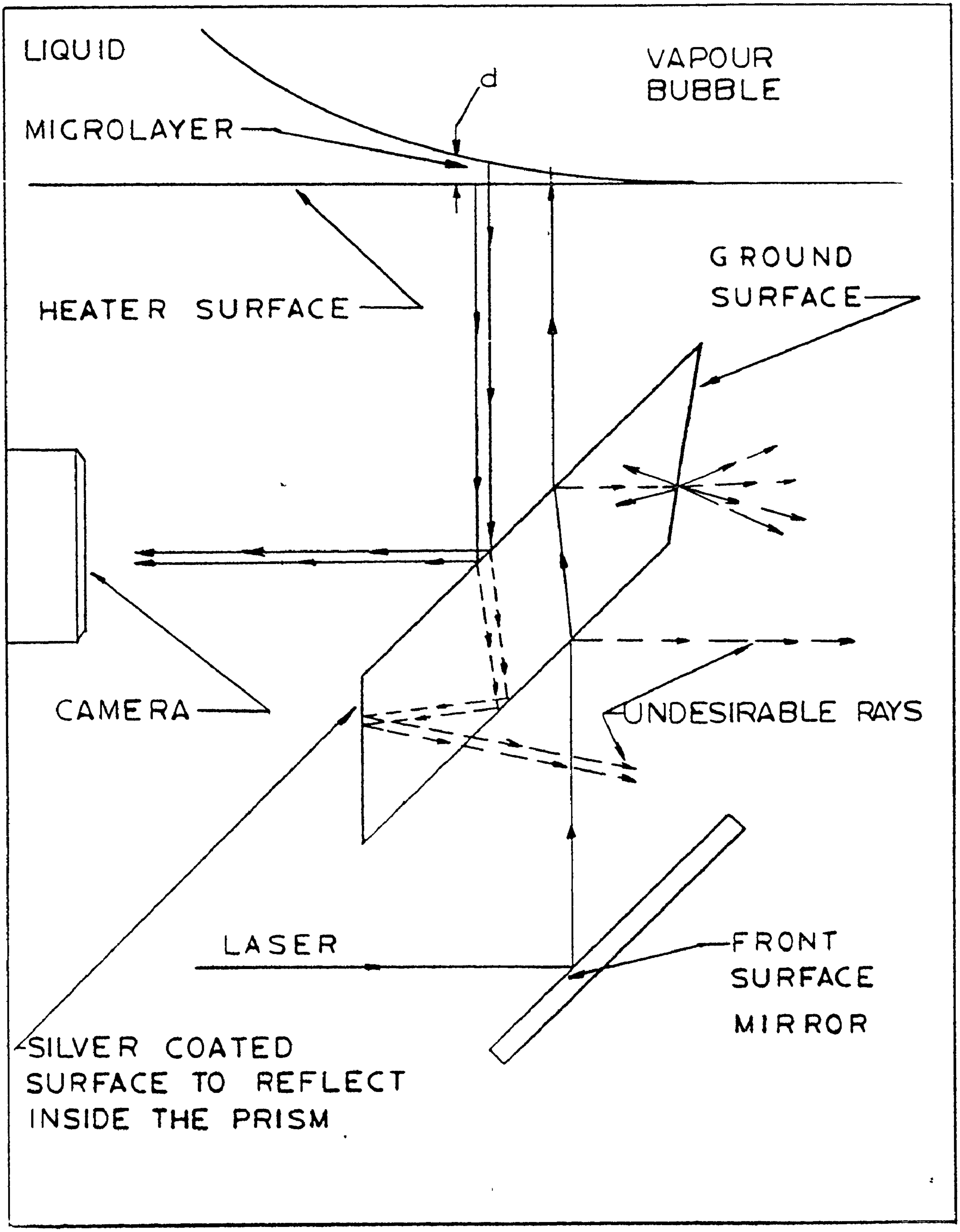

Figure 11. SCHEMATIC OF INTERFEROMETER

heater glass plate, thus illuminating the boiling phenomena occurring at the upper surface of the galss heater. The rhomboidal prism had its bottom surface coated with $1/\sqrt{2}$ wavelength thickness of antireflective coating. Since the light meets this surface at 45 degrees, $1/\sqrt{2}$ wavelength thickness would result in 1/4 wavelength of actual path length, thereby maximizing the antireflective effect. The front surface of the rhomboidal prism was coated with silver in such a manner that it would form a mirror that reflected inside the prism. This mirror was used to block the path of any reflection from the bottom surface of the prism thereby ensuring that the interferometer's output would contain interference patterns formed only by the boiling phenomena and the heater plate. Figure 10 also shows the method used in order to achieve fine adjustment of the first mirror at the base of the interferometer, and of the rhomboidal prism. By turning the fine threaded screws against the extended levers about the turning axes, one could made adjustments as fine as 1/100 of a degree.

Because of the high sensitivity of laser light to interference, the lower surface of the glass heater was also coated with 1/4 wavelength thickness antireflective coating. Table 1 presents the optical analysis of all the reflecting surfaces and Figure 12 shows the results of the analysis diagramatically. I_0 indicates the incident beam intensity after it had passed through the rhomboidal prism. This beam was used to illuminate the boiling phenomena. Each of the i surfaces reflected

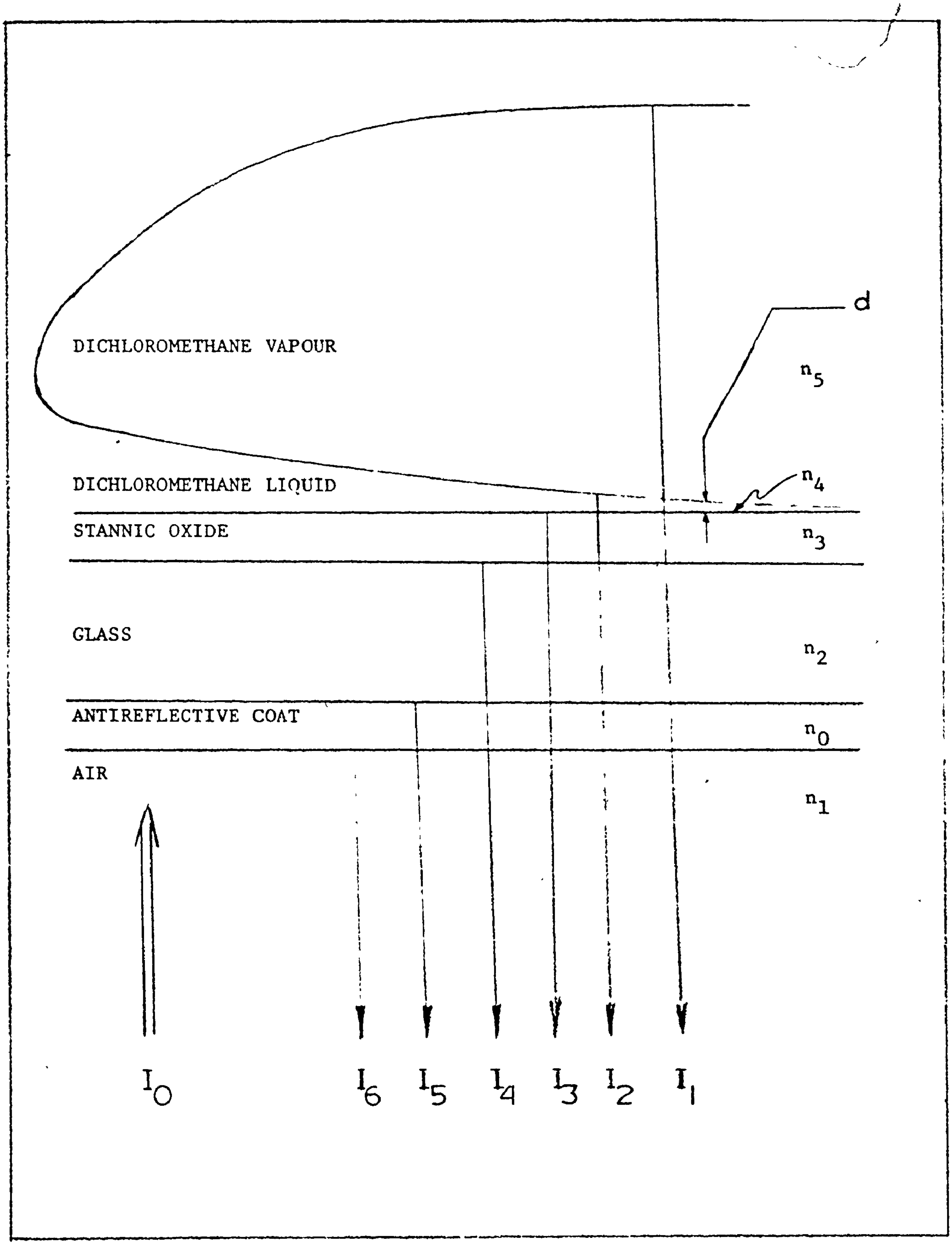

Figure 12. SPECIMEN OPTICS

TABLE 1

REFRACTIVE INDICES

n_0	1.283	Antireflective coat
n_1	1.000	Air
n_2	1.479	Glass
n_3	1.993	Stannic Oxide
n_4	1.356	Dichloromethane liquid
n_5	1.000	Dichloromethane vapour

CALCULATION OF RELATIVE INTENSITIES

$$\frac{I_6}{I_0} = \left(\frac{n_0 - n_1^2}{n_0 + n_1^2}\right)^2 = \left(\frac{1.283 - 1}{1.283 + 1}\right)^2 = 0.0153 \qquad 1.5\ \%$$

$$\frac{I_5}{I_0 - I_6} = \left(\frac{n_2 - n_0^2}{n_2 + n_0^2}\right)^2 = \left(\frac{1.479 - 1.283^2}{1.479 + 1.283^2}\right)^2 = 0.0028 \qquad 0.2\ \%$$

$$\frac{I_4}{I_0 - I_6 - I_5} = \left(\frac{n_3 - n_2^2}{n_3 + n_2^2}\right)^2 = \left(\frac{1.993 - 1.479^2}{1.993 + 1.479^2}\right) = 0.0021 \qquad 0.2\ \%$$

$$\frac{I_3}{I_0 - I_6 - I_5 - I_4} = \left(\frac{n_4 - n_3^2}{n_4 + n_3^2}\right)^2 = \left(\frac{1.356 - 1.993^2}{1.356 + 1.993^2}\right) = 0.2410 \qquad 24.1\ \%\ ***$$

$$\frac{I_2}{I_0 - I_6 - I_5 - I_4 - I_3} = \left(\frac{n_5 - n_4^2}{n_5 + n_4^2}\right)^2 = \left(\frac{1.000 - 1.356^2}{1.000 + 1.356^2}\right)^2 = 0.0872 \qquad 8.7\ \%\ ***$$

$$\frac{I_1}{I_0 - I_6 - I_5 - I_4 - I_3 - I_2} = \left(\frac{n_4 - n_5^2}{n_4 + n_5^2}\right)^2 = \left(\frac{1.356 - 1.000^2}{1.356 + 1.000^2}\right)^2 = 0.0228 \qquad 2.2\ \%$$

*** Note that the material selection is such that it maximizes the reflectivity back light of intensity I_i, which is the function of the combined effect of the refractive indices (n_{i-1} and n_i) of the media existing on each side of the surface.

$$\frac{I_i}{I_0} = \left(\frac{n_2 - n_1^2}{n_2 + n_1{}^2}\right)^2$$

By selecting the materials with the appropriate refractive index, it was possible to increase the intensity of I_2 and I_3 and reduce the intensity of the others. I_2 and I_3 were the important components of the whole research investigation, as interference between them gave the image that was photographed in order to determine and microlayer thickness.

The interferometer's output was photographed on Kodak 4X negative film, at the rate of 2500 frames per second, through a 16mm Hycam K1001 R high speed camera mounted outside the interferometer. The interference patterns produced whenever a bubble occurred were deflected into the objective lens of the camera by the upper surface of the rhomboidal prism.

Similarly to Jawurek (8), the mathematical formulae describing the microlayer thickness for the formation of fringes are given below. In the present investigation the fringes were produced by an interference action between I_2 and I_3. The physical meaning of the variable "d" is shown in Figures 11 and 12.

For bright fringes

$$d = (2m + 1) \left(\frac{\lambda}{4n_4}\right) \quad , \quad m = 0, 1, 2 \ldots\ldots$$

In this case the bright fringes indicated step wise that the microlayer thickness was;

$$1 \left(\frac{\lambda}{4n_4}\right) , \quad 3 \left(\frac{\lambda}{4n_4}\right) , \quad 5 \left(\frac{\lambda}{4n_4}\right) \quad \text{etc.}$$

For dark fringes

$$d = (2m) \left(\frac{\lambda}{4n_4}\right) \quad , \quad m = 0, 1, 2, \ldots\ldots$$

Since during the present investigation the interference patterns were recorded by negative films, the actual bright fringes appeared dark. Therefore, although the measured fringes were the dark ones, the relationship of the bright fringes applied.

For both cases, the reflected intensity was governed by the relation ;

$$I_r = (r_1^2 + r_2^2 + 2r_1 r_2 \cos \emptyset) I_o$$

For antireflective coating, the intensity reflected in terms of refractive indices is given by ;

$$I_r = \left(\frac{2(n_2 - n_1^2)}{(n_1 + n_2)^2} \right)^2 I_o$$

Where I_r is desired to be as small as possible. Hence in order for

$$I_r \longrightarrow 0$$

$$n_2 \longrightarrow n_1^2$$

Further improvements of the optical system might have been achieved using a spectrum analyser. The velocity of either the upper or the lower vapour-liquid interface of a bubble, could be measured. The existing interferometer has the potential to provide this data through optical heterodyning (Doppler effect) between I_1 and I_3 or I_2 and I_3 respectively.

CHAPTER III

CHAPTER III

TEST CONDITIONS

A. Test Fluid

The chosen test fluid was dichloromethane (methylene chloride). This fluid was selected because experimentation with water had indicated (13) that the stannic oxide coating was incompatible with boiling water. Boiling water tends to attack the oxide coated surface in an electrolytic manner and consequently eliminates its usefulness within a few minutes. Several workers have reported these results and in order to solve this problem they have used methanol, carbon tetrachloride, Freon 113, or dichloromethane. The preference to use dichloromethane for the present investigation was based on its considerably less hazardous properties i.e. non-poisonous and non-explosive. In addition, it boils at a low temperature and has a much desired refractive index. Figure 13 shows the vapour temperature saturation curve.

B. Temperature Measuring Locations

When experiments were performed the three thermocouple junctions were positioned at 0.05 inches, 0.45 inches and 0.50 inches from the heater surface. The selection of these locations for the thermocouple junctions provided information for the temperature variation within the bulk liquid and the boundary layer adjacent to the heat transfer surface. The bulk liquid temperature was defined as the average output of the two thermocouples that had their junctions positioned at o.45 inches and at 0.50 inches. Consequently, for the purpose of this research investigation

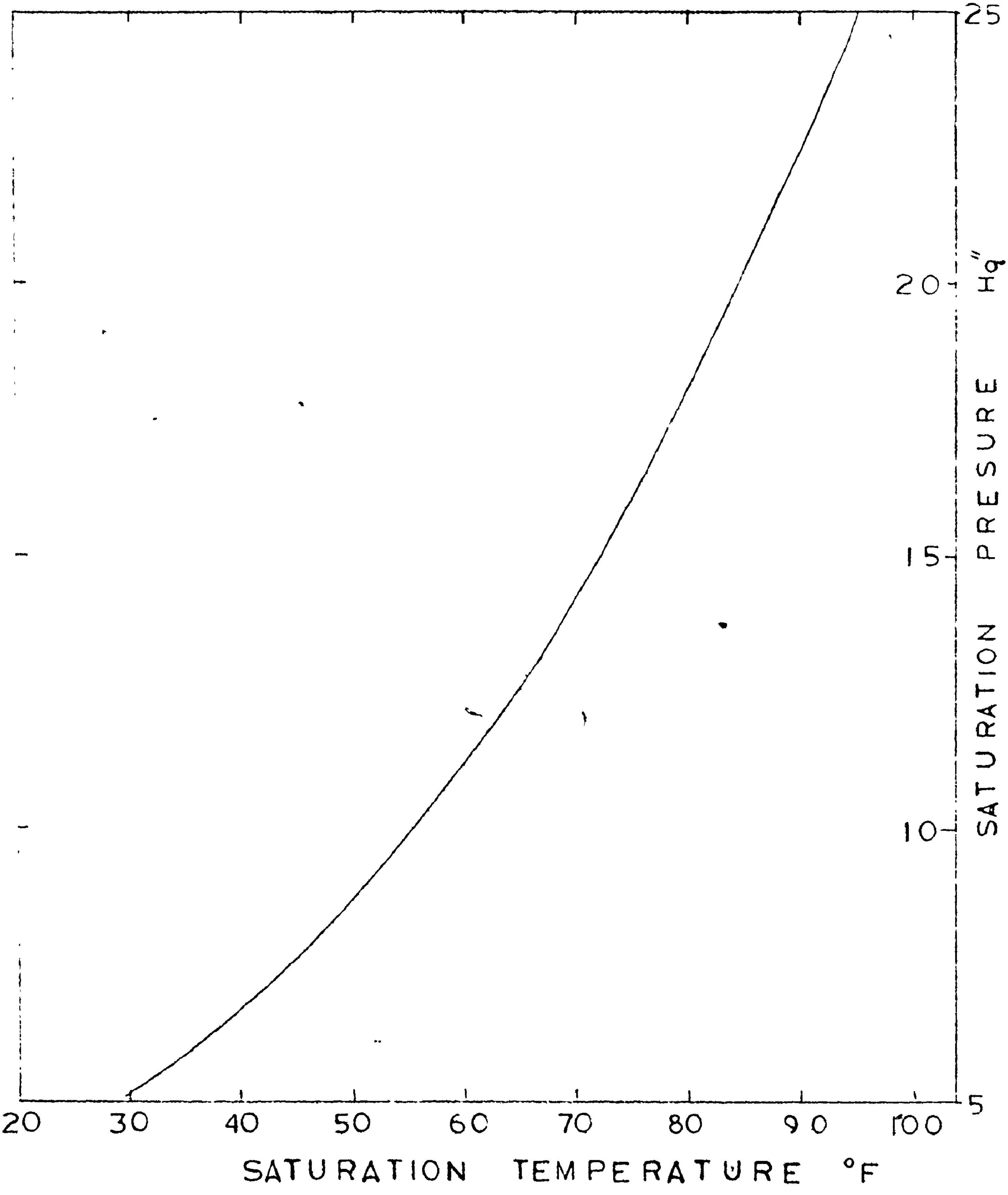

Figure 13. VAPOUR PRESSURE CURVE FOR DICHLOROMETHANE

the method used to define subcooling was to compute the difference between the saturation temperature at the heat transfer surface and the average temperature level at the two arbitrarily chosen positions in the bulk liquid.

C. Data Organization

Six levels of heat flux and four levels of subcooling were investigated for their combined influence upon nucleate boiling. For the purpose of being able to identity the data, these tests were grouped to form a matrix having a constant heat flux in every row and approximately constant subcooling in every column as shown in Table 2.

TABLE 2

DATA ORGANIZATION

Decreasing q/A ↓	Increasing (T_{sat} - T_{∞}) →			
	(1,1)	(1,2)	(1,3)	(1,4)
	(2,1)	(2,2)	(2,3)	(2,4)
	(3,1)	(3,2)	(3,3)	(3,4)
	(4.1)	(4,2)	(4,3)	(4,4)
	(5,1)	(5,2)	(5,3)	(5,4)
	(6,1)	(6,2)	(6,3)	(6,4)

The six levels of heat flux were q/A = 19,400, 13,500, 8,900, 5,100 2,300, and 1,300 Btu/hr ft^2. For every heat flux under investigation the subcooling temperature was varied from 0^oF (for saturated boiling) to the maximum possible obtainable value. The variations were taken in four increments by increasing the flow of water correspondingly in the subcooling heat exchanger. This procedure was continued until sufficient data was supplied for every point in the matrix. During these tests, temperature as well as photographic data were obtained and two complete matrices were recorded.

In addition to the above, one set of data was obtained through a different procedure where the flow through the subcooling heat exchanger was fixed, and the heat flux was changed. In this manner, the matrix of the experiment was scanned by columns rather than by rows as in the previous case. Carrying out the experiments with either one of the two procedures, the system was always given sufficient time to reach equilibrium.

The matrix grouping has organized the data in such a way that the variation of any recorded parameter with heat flux or subcooling could be obtained by plotting the data by columns or by rows respectively.

Motion pictures were obtained only for the three first rows of the matrix since no boiling was observed for the other three.

CHAPTER IV

CHAPTER IV

TEST PROCEDURE

Preliminary tests were conducted prior to the commencement of the research investigation during which the normal functioning of each component in the system was established.

Although the test vessel was disassembled and reassembled twice, only one charge of dichloromethane was used. Consequently, all the temperature data as well as the photographic data were obtained from boiling the same charge of dichloromethane (approximately 30 cm^3). Also, no replenishing was necessary during the investigating period due to the effectiveness of the condensing system.

The first pretest procedure was the adjustment of the two screws in the interferometer to position the light beam approximately in the middle of the heater surface. This procedure was followed by adjusting the camera's positioning and focussing on the illuminated section.

The atmospheric pressure was measured, and the appropriate manometer reading that would ensure the desired pressure in the test vessel was calculated. After both condensers had had their respective flows established, the vacuum pump and the direct current power supply were started. The pressure in the test vessel was slowly reduced to the desired value with the manual operation of the pressure control valve. The change of flow through the subcooling heat exchanger, whenever employed, always caused pressure transients in the test vessel which were continuously reduced with additional adjustment of the pressure control valve until a steady-state was achieved.

During the period of time in which steady-state boiling conditions were being established, the temperature recorder and the potentiometer were calibrated against a standard cell with known E.M.F. One of the thermocouples that measured the bulk liquid temperature was monitored by the recorder and the camera was loaded with film and set at a filming rate of 2,500 frames per second.

Steady-state test conditions were considered to have been reached when the manometer appeared visually unchanged and at the same time, the bulk liquid temperature thermocouple remained constant within $\pm$ 5% for a period of 5 minutes or longer. When these conditions were fulfilled, the thermocouple that was "epoxied" to the heater surface was connected to the recorder, and the steady-state values of each of the other three thermocouple outputs were measured sequentially. Once the temperature values had been obtained, the readings of the voltmeter and ammeter on the power supply were recorded. For those tests involving photography of the phenomena occurring on the heat teansfer surface, high speed motion pictures were obtained immediately following the potentiometer measurements. The framing rate chosen enabled a complete cycle of vapour bubble emission including active and inactive periods to be photographed. Each of the film strips obtained were later analyzed to determine the frequency of vapour bubble emission, the density of active nucleation side, and the volume of the microlayer evaporated for the particular combination of heat flux and subcooling investigated.

CHAPTER V

CHAPTER V

DATA REDUCTION

A. Thermometric Results

The following paragraphs describe the methods used in calculating the heat flux, the saturation temperature, the surface temperature, the liquid temperature, the subcooling and the superheat.

1. The heat transferred to the liquid at the heat transfer surface was calculated from the total power supplied to the oxide coating minus the sum of the heat losses.

$$q/A = 3.414 \ EI/A - \sum_{i=1}^{n} (q_{Loss}/A)_i$$

One of the heat losses in the above equation is the heat loss to the air space. This was computed by means of the correlation.

$$Nu = 0.27 \quad (Pr \ Gr)^{1/4}$$

which applied (13) for natural convection from a heater surface facing downward. For the purpose of computing an approximate value for this heat loss, the difference in temperature between the underside of the heater surface and the temperature of the air beneath it was taken to be the difference between the temperature measured by the "epoxied" thermocouple and the ambient temperature. Based on these data the total heat loss to the air space was computed to be 0.02 Btu/hr ft^2.

Another mode of heat loss was the heat conducted to the base plate through the rubber gasket that separated the heater surface from the base plate. This loss was approximated by an analysis based on one dimensional conduction. The temperature of the base plate was assumed to be the same as that of the bulk liquid in contact with it, thus giving an average temperature difference of 30°F. Using a rubber thermal conductivity of 0.07 Btu/hr ft°F the total heat loss to the base plate was computed to be 0.06 Btu/hr ft^2.

2. The saturation temperature of the liquid at the heat transfer surface could not be measured. Therefore, the saturation temperature was deduced from the measured pressure existing in the test vessel and from the saturation curve shown in Figure 13. No hydrostatic pressure corrections were made, however, since the pressure fluctuations in the test vessel were much greater than the additional pressure applied on the heater surface due to the weight of the 2.5" height of liquid.

3. The temperature at the heat transfer surface was assumed to be the same as that of the underside of the heat glass plate because heat conduction through the plate represented less than 2% of the heat dissipated at the boiling surface. In this case, no corrections were made for the temperature drop by conduction through the test specimen since the effect of the thermal conductivity (k plate = 0.6 Btu/ hr ft^{o}F) through a plate thickness of 0.125 in. would result in a very small temperature drop. Detailed calculations for this temperature drop have been performed by other workers (13) and the temperature correction was estimated to be approximately 0.48^{o}F.

4. The temperature of the liquid was computed by averaging the output of the two thermocouples that were positioned arbitrarily inside the liquid in the test vessel.

$$T_{\infty} = 1/2\ (T_1 + T_2)$$

5. The subcooling temperature was computed to be the difference between the saturation temperature as defined above and the liquid temperature .

$$\Delta T_{Subcooling} = (T_{sat} - T_{\infty})$$

6. The superheat was defined to be the temperature difference between the surface temperature and the saturation temperature.

$$\Delta T_{superheat} = (T_w - T_{sat})$$

B. Photographic Results

The paragraphs in this section describe the methods used in calculating the true film speed, the active site density, the bubble frequency, the maximum bubble size, the micro-layer thickness and the volume of evaporated liquid.

1. The framing rate was set at 2,500 frames per second on the HYCAM camera. However, in order to obtain the true speed of the film, the total number of frames was divided by the total number of seconds of filming. Allowances were made on each film strip for the first seven feet where acceleration effects were present and had to be excluded from the averaging process. Appendix A contains a summary of the framing rates for each film.

2. The active site density and average population density were determined by projecting each set of film strips containing the photographic data of the nucleate boiling phenomenon. The entire film strip was examined in the

enlarged projection, and each site was marked on the projection at the point where bubbles were initiated. No artificial sites existed, and since it had been assumed that the active sites were uniformly distributed over the total area of the heater surface, it is further assumed that the section of surface examined was representative. This assumption seemed to be quite reasonable for these tests in which active site density was large, although there is some question of the representativeness of the data for those tests in which the active site density was small.

3. The period of time between cycles of vapour bubble emmission was also determined by the detailed examination of the projected film strips. The growth of each single vapour bubble at each site was followed frame by frame until the bubble departed and another bubble was initiated at the same nucleation site. This interval of time has been designated as the period of time between cycles of bubble emission, whose reciprocal provides the frequency of vapour bubble emission. The frequency with which bubbles were produced, was averaged for each site, and finally the total number of active sites was summed up and the average frequency over all sites was obtained.

Although the entire film strip was examined, the procedure outlined above raised the question of representativeness as mentioned earlier because some of the sites produced only one or two bubbles while other sites produced as many as one hundred bubbles. Despite the uncertainties, however, it is believed that the determination of the average frequency provided relative indications of the influence of the parameters concerned. The histograms of the various frequencies are summarized in Appendix B. their mean value was taken as the average frequency over all the sites.

4. As employed here, the maximum bubble size is the diameter of the image projected in the plane of the heat transfer surface. The maximum diameter then, was determined by direct measurement on the screen, in which the film strips were projected. The magnification ratio of the projected screen size to the real size was 30:1 and similar magnification was transferred to the graduated measuring device used. Chapter VI summarizes the maximum bubble size in a matrix format, and gives a graphical representation of its changes with varying heat flux and subcooling.

5. The microlayer thickness was measured by means of the interference rings as shown in Figure 14. During film examination, the number of dark fringes (m) was counted starting from the center of the bubble. Also, the radius (r) of these fringes from the same center was measured and recorded. Then for every m^{th} dark fringe a step of height equivalent to $(2m + 1)$ $(\lambda / 4n_4)$ above the heater surface was plotted at a radius (r) from the bubble's center. In this manner the

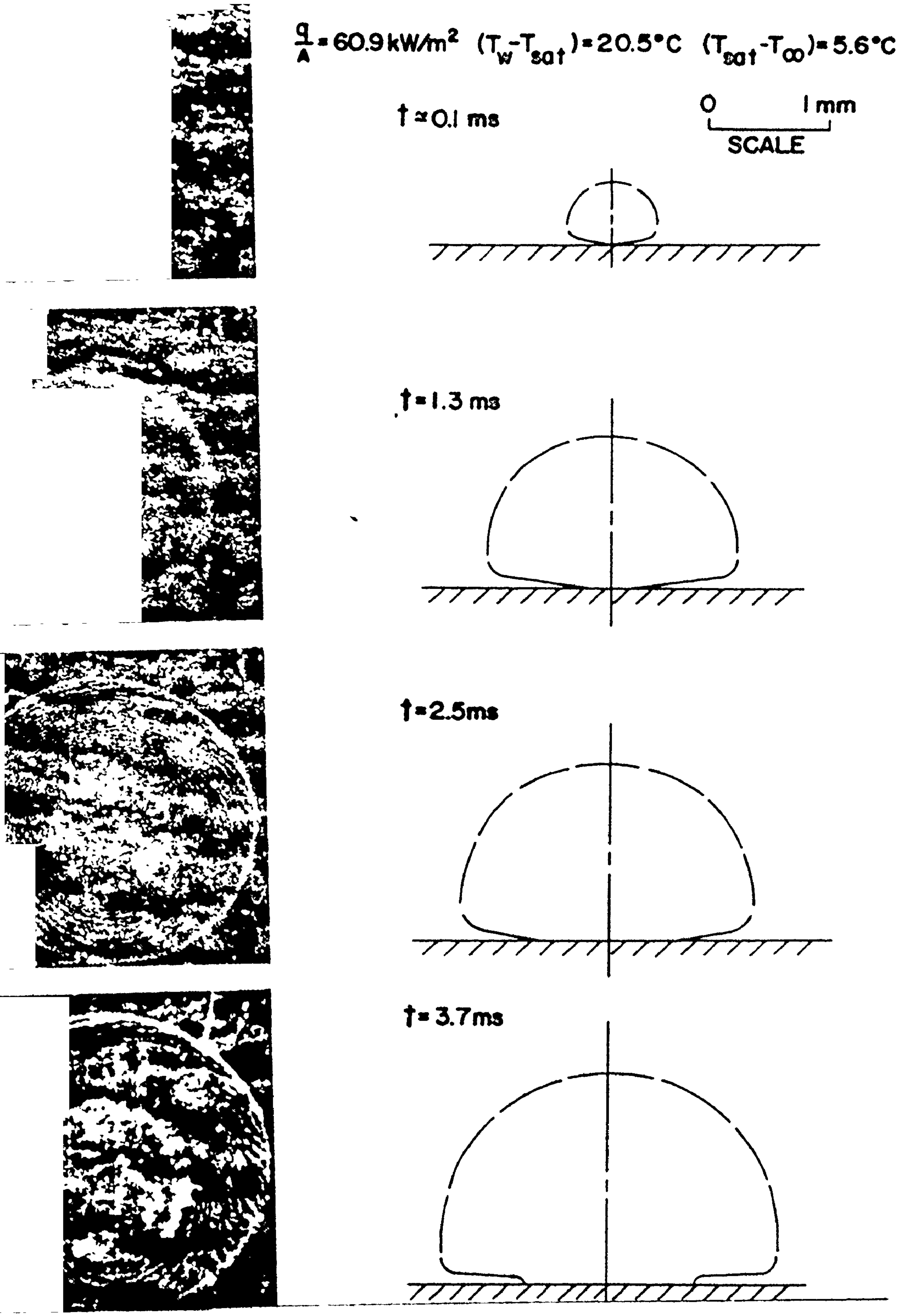

$\frac{q}{A}$ = 60.9 kW/m² $(T_w - T_{sat})$ = 20.5°C $(T_{sat} - T_\infty)$ = 5.6°C
t ≃ 0.1 ms
0 1 mm
SCALE
t = 1.3 ms
t = 2.5 ms
t = 3.7 ms

profiles of the bubble and the profiles of the microlayer thickness were obtained at all the growing stages of each bubble examined. A representative number of bubbles (3-8) were studied for each film strip and they all were examined frame by frame. Considering the time of growth given by the number of frames elapsed, the microlayer thickness as a function of radius and time $\tilde{\delta}(r, t)$ was obtained.

Because the bubble projections on the plate were not always circular, the radius along which measurements were made was selected to have the average length of the maximum and the minimum radii of the bubble.

Finally, $\tilde{\delta}_o(r)$ was plotted for each growing bubble as indicated in the diagrams of Figures 34 to 45.

6. Figure 15 shows the microlayer cross-sectional area bounded above by the line $\tilde{\delta}_o(r)$, below by the line representing the surface heater and on the side by the line plotted from the profile of the microlayer before departure. If this area were allowed to revolve about an axis that is perpendicular to the heater surface and which passes through the center of the bubble, it would produce a volume of revolution, approximately equivalent to the volume of liquid evaporated during the bubble's growing stages, which represents

$$V_E = 2\pi \int_0^{R(t)} \left[\tilde{\delta}_o(r) - \tilde{\delta}(r,t)\right] r\, dr$$

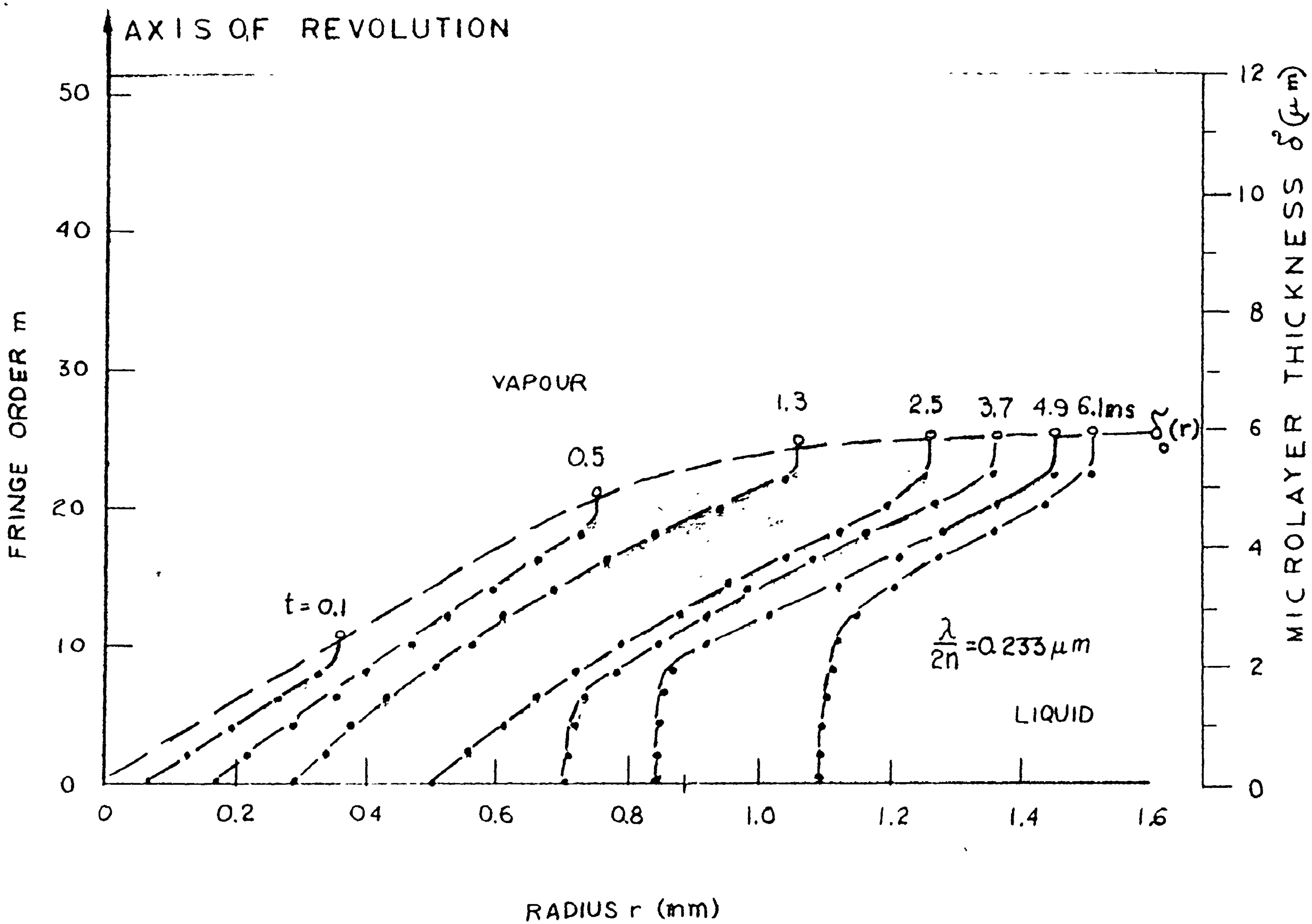

Figure 15 AREA OF REVOLUTION

Appendix C summarizes the results of these computations in matrix form and gives a graphical representation of changes with varying heat flux and degree of subcooling.

Finally, the total energy transported by microlayer evaporation was computed by :

$$q/A_{Microlayer} = 2\pi \rho_\ell h_{fg} \frac{N}{A} f \int_0^{R(t)} \left[\delta_o(r) - \delta(r, \tau) \right] r \, dr$$

where $\delta(r, \tau)$ represents the instantaneous microlayer profile at the instant of departure $t = \tau$.

CHAPTER VI

CHAPTER VI

RESULTS

The results obtained are presented in this section without comment. Most discussion and interpretations will be given in the following sections. The experimental results are categorized under the headings:

A. Heat transfer results

B. Microlayer evaporation results

The data is presented in a series of graphs showing the influence of heat flux and subcooling upon each one of the measured quantities. The numerical values plotted are tabulated in the Appendices.

A. Heat Transfer Results

The results of a series of tests performed to determine the characteristic boiling curve for dichloromethane boiling on the oxide coated glass surface is presented in Figure 16. These results which were obtained for various levels of heat flux under saturated and subcooled boiling conditions are presented as a plot of heat flux versus subcooling and superheat. Figure 16 also shows the transition from Natural Convection to Nucleate Boiling for both plots (saturated boiling and maximum subcooled boiling conditions.

Figure 17 summarizes the heat transfer results in the form of plots of superheat versus subcooling with levels of heat flux as parameters. This parametric form shows the influence of heat flux and subcooling upon the superheat.

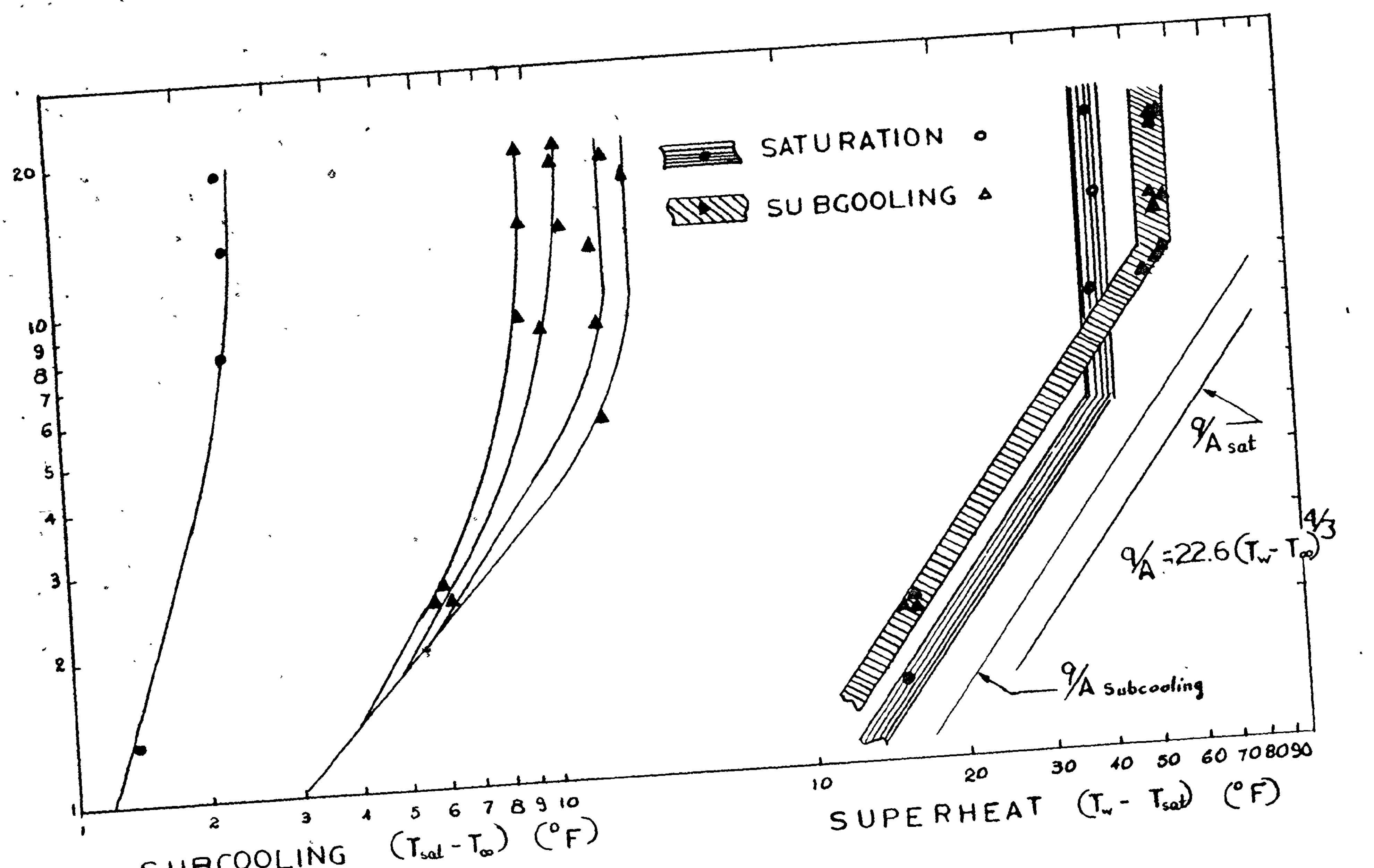

Figure 16 CHARACTERISTIC CURVES

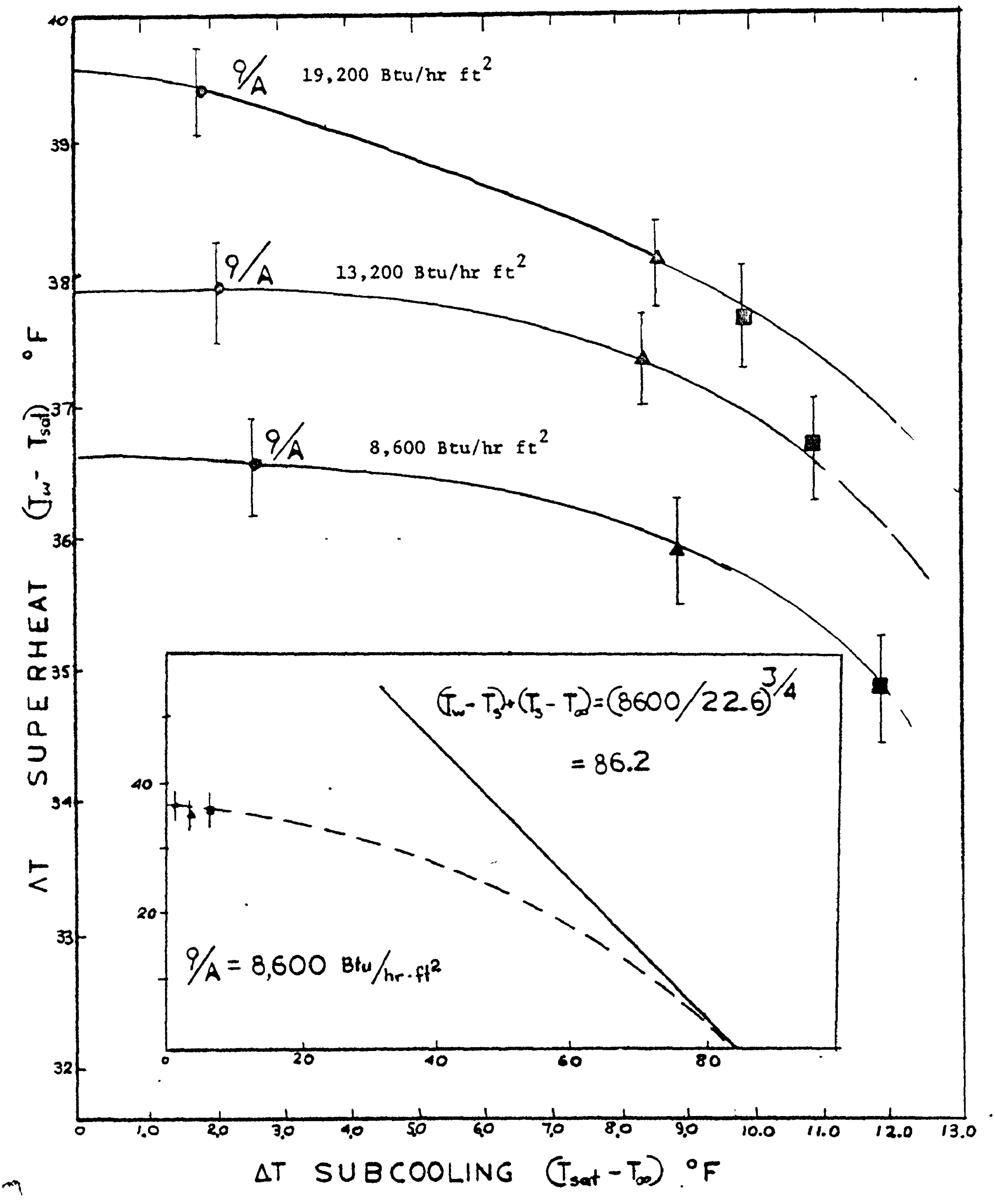

q/A 19,200 Btu/hr ft²
q/A 13,200 Btu/hr ft²
q/A 8,600 Btu/hr ft²
$(T_w - T_s) + (T_s - T_\infty) = (8600/22.6)^{3/4}$
= 86.2
q/A = 8,600 Btu/hr·ft²
ΔT SUPERHEAT $(T_w - T_{sat})$ °F
ΔT SUBCOOLING $(T_{sat} - T_\infty)$ °F

The tables contained in Appendix A summarize the data for the 12 combinations of heat flux and levels of subcooling investigated. Each table contains the experimental data for each point in the heat flux and subcooling matrix. The remaining Appendices contain all the pertinent experimental data.

B. Microlayer Evaporation Results

Figures 18 to 29 are presenting prints made from motion picture films. The interference rings as captured in the films can be clearly seen in these prints. Each figure presents the growth stages of a bubble, by means of four prints adjacent to the plot of the instantaneous microlayer profile as deduced from the interferograms. Also each figure contains prints from different combinations of heat flux and subcooling level.

Figures 30 to 52 present the results of the study which determined the total heat transferred by microlayer evaporation, and the influence exerted upon it by varying heat flux and level of subcooling.

The results of the active site density N/A are presented in figure 30 in the form of plots of average population density versus subcooling for various values of constant heat flux. The values presented in this plot represent the bubble population on the surface at a given instant of time. The bubble frequency averaged over all active sites is given in figure 31. The plot shows the effect of subcooling and heat flux upon the frequency with which bubbles were produced. Figure 32 presents results in the form of plots of bubble flux density versus subcooling, again with the levels of heat flux as parameters. The values presented in this plot, indicate the number of bubbles that departed from the heater surface per unit time at specified levels of heat flux and subcooling.

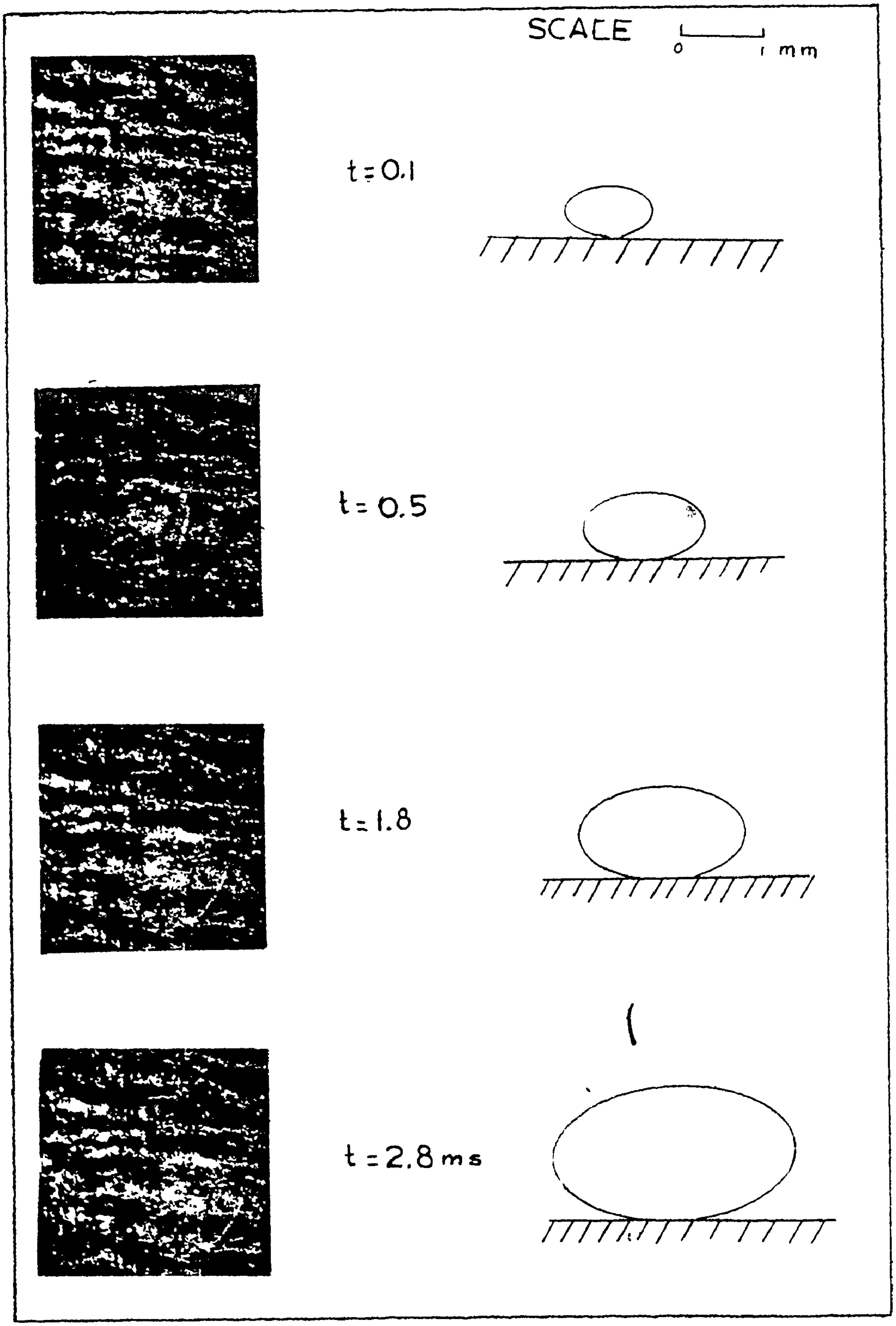

Figure 18

THE OF THE (1.1)

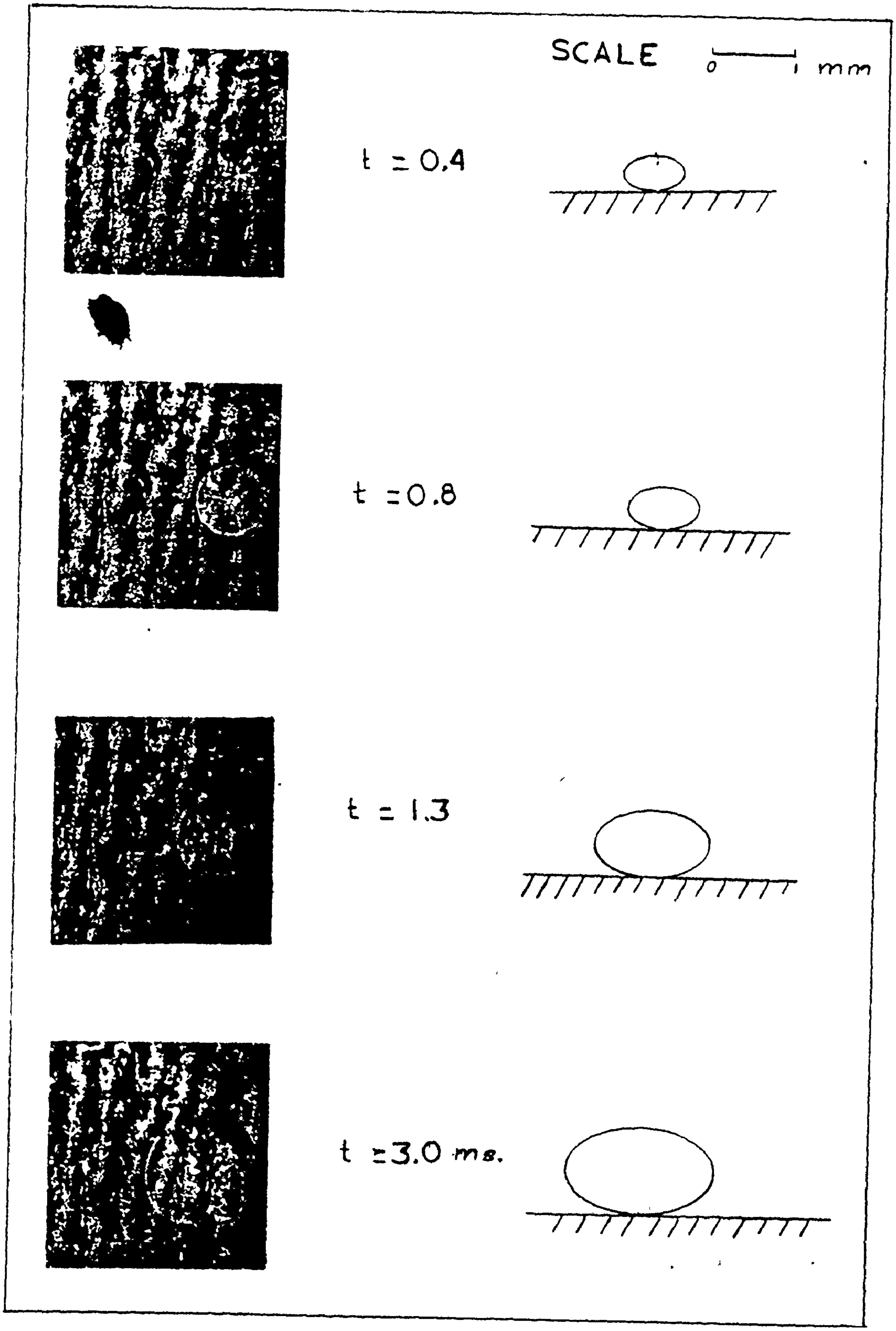

Figure 19

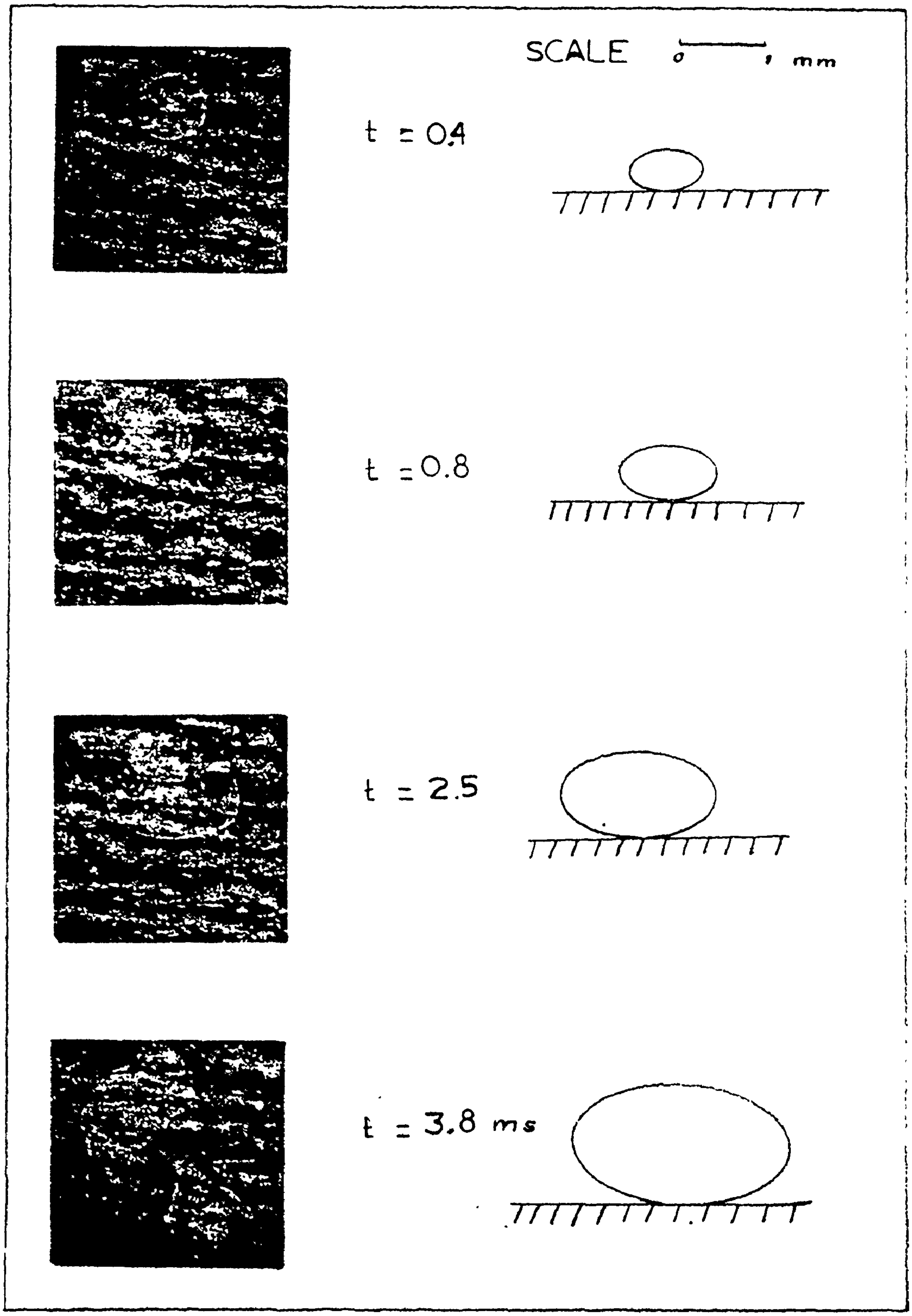

Figure 20

OF THE OF THE DATA (1,3)

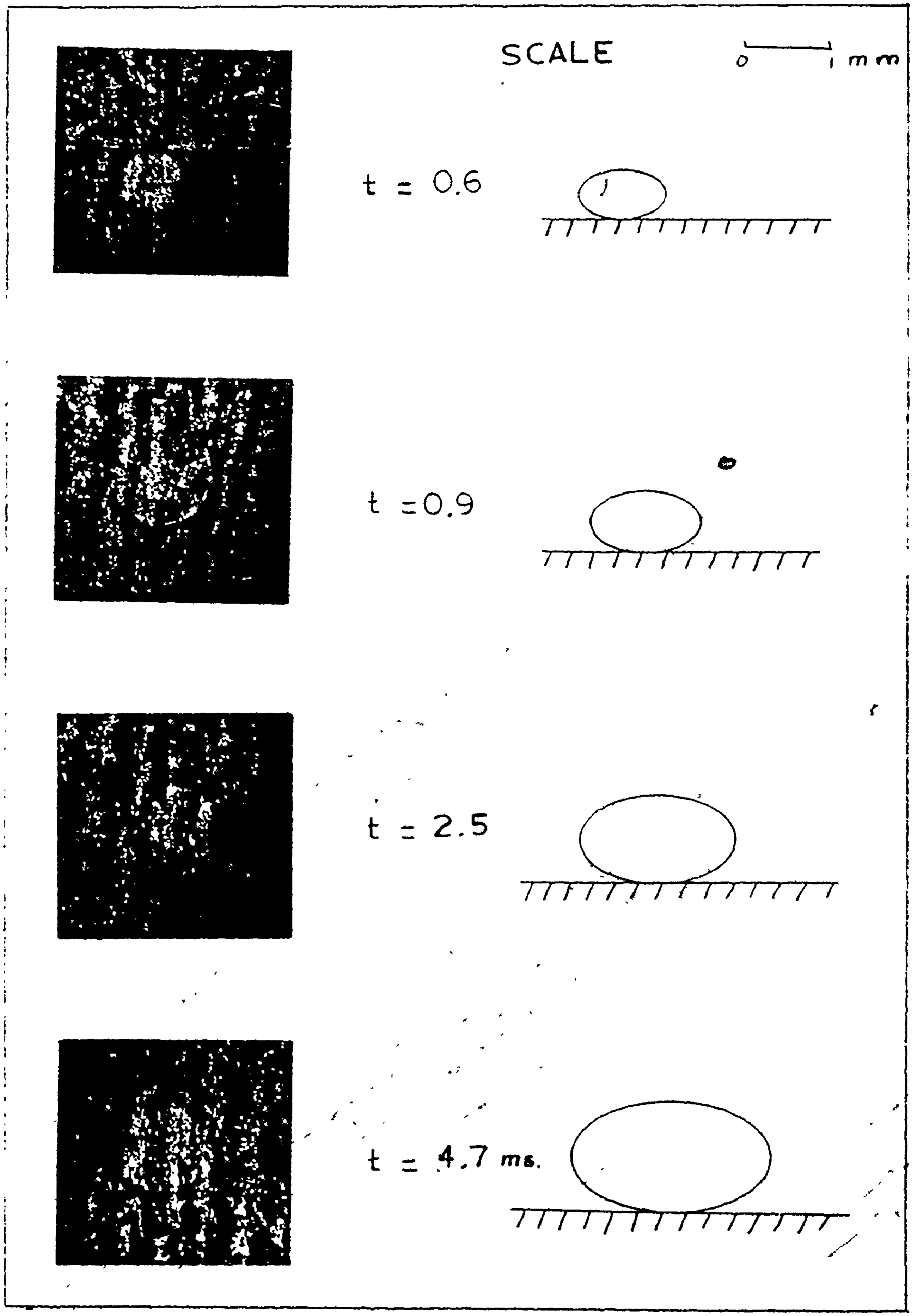

Figure 21

PRINTS OF THE INTERFEROGRAMS OF THE DATA POINT (1,4)

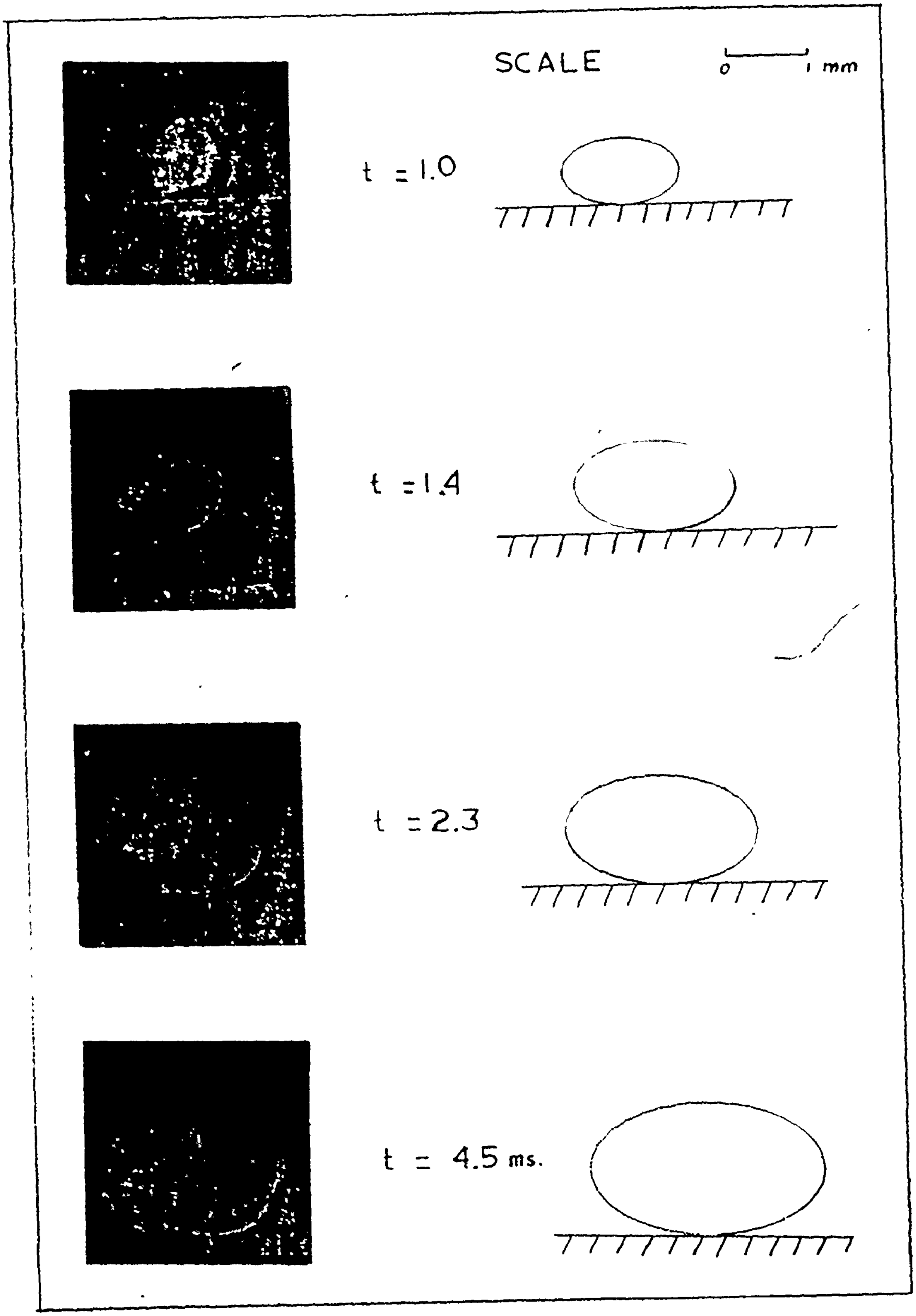

Figure 22

PRINTS OF THE INTERFEROGRAMS OF THE DATA POINT (2,1)

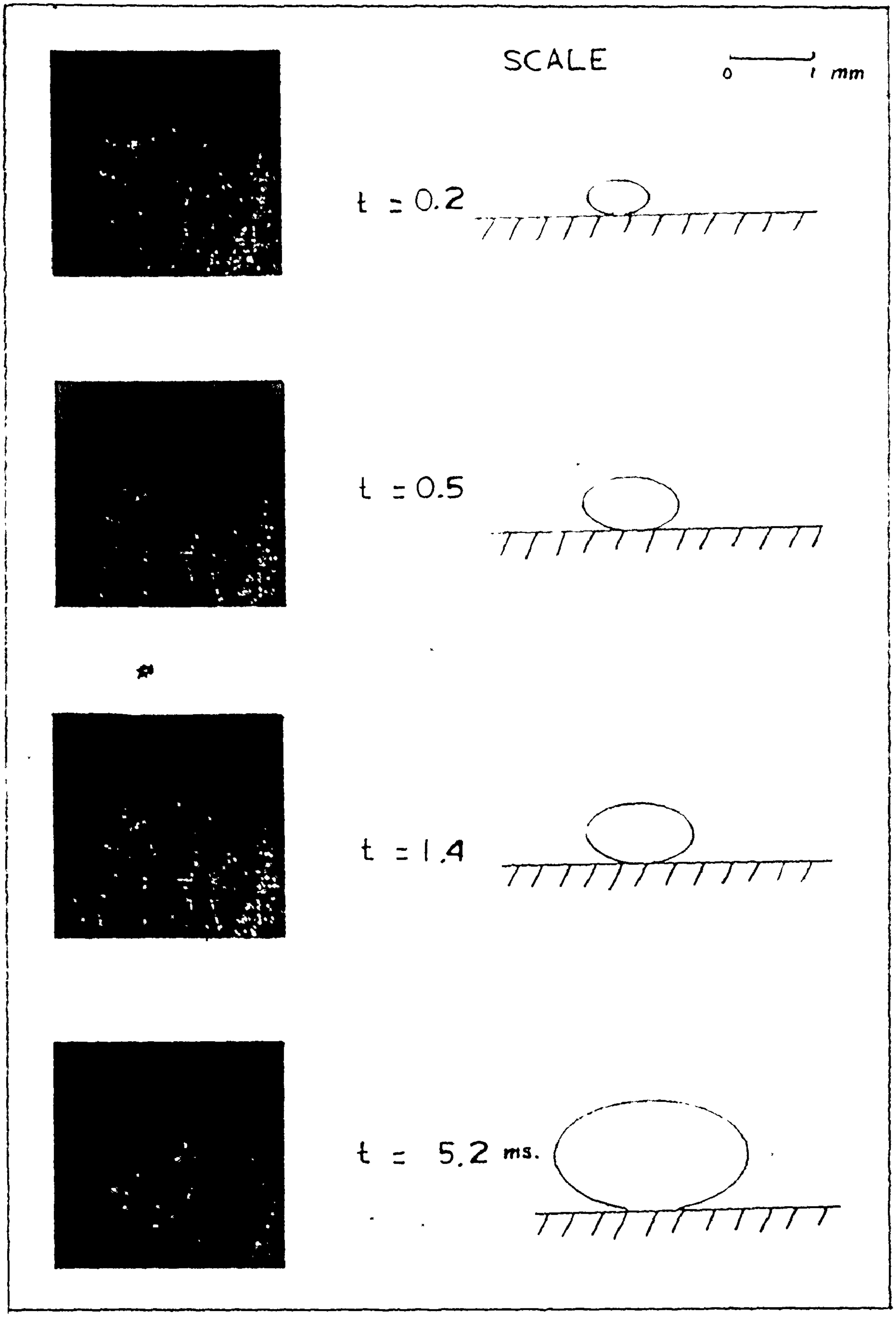

Figure 23
PRINTS OF THE INTERFEROGRAMS OF THE DATA POINT (2,2)

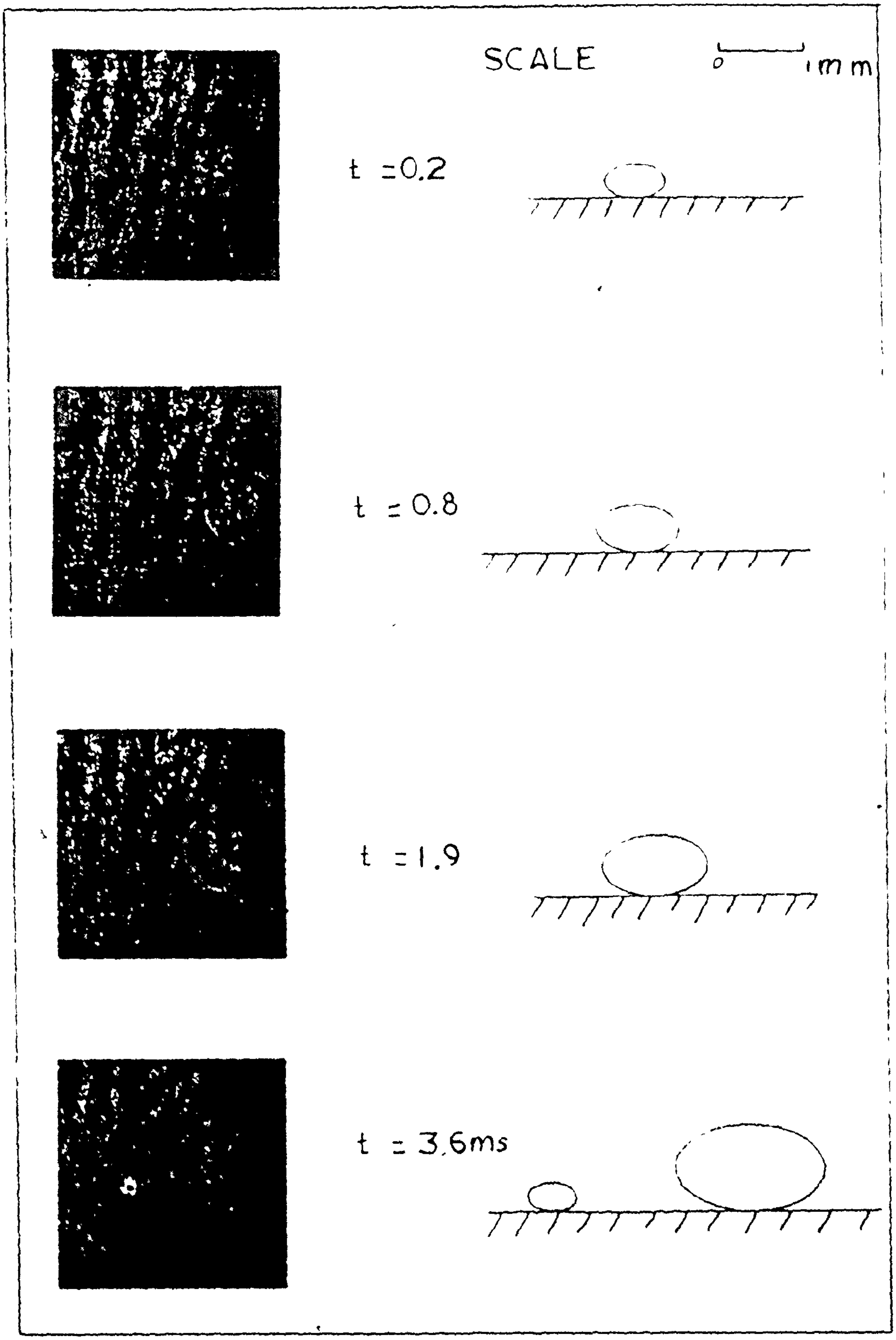

Figure 24

PRINTS OF THE INTERFEROGRAMS OF THE DATA POINT (2,3)

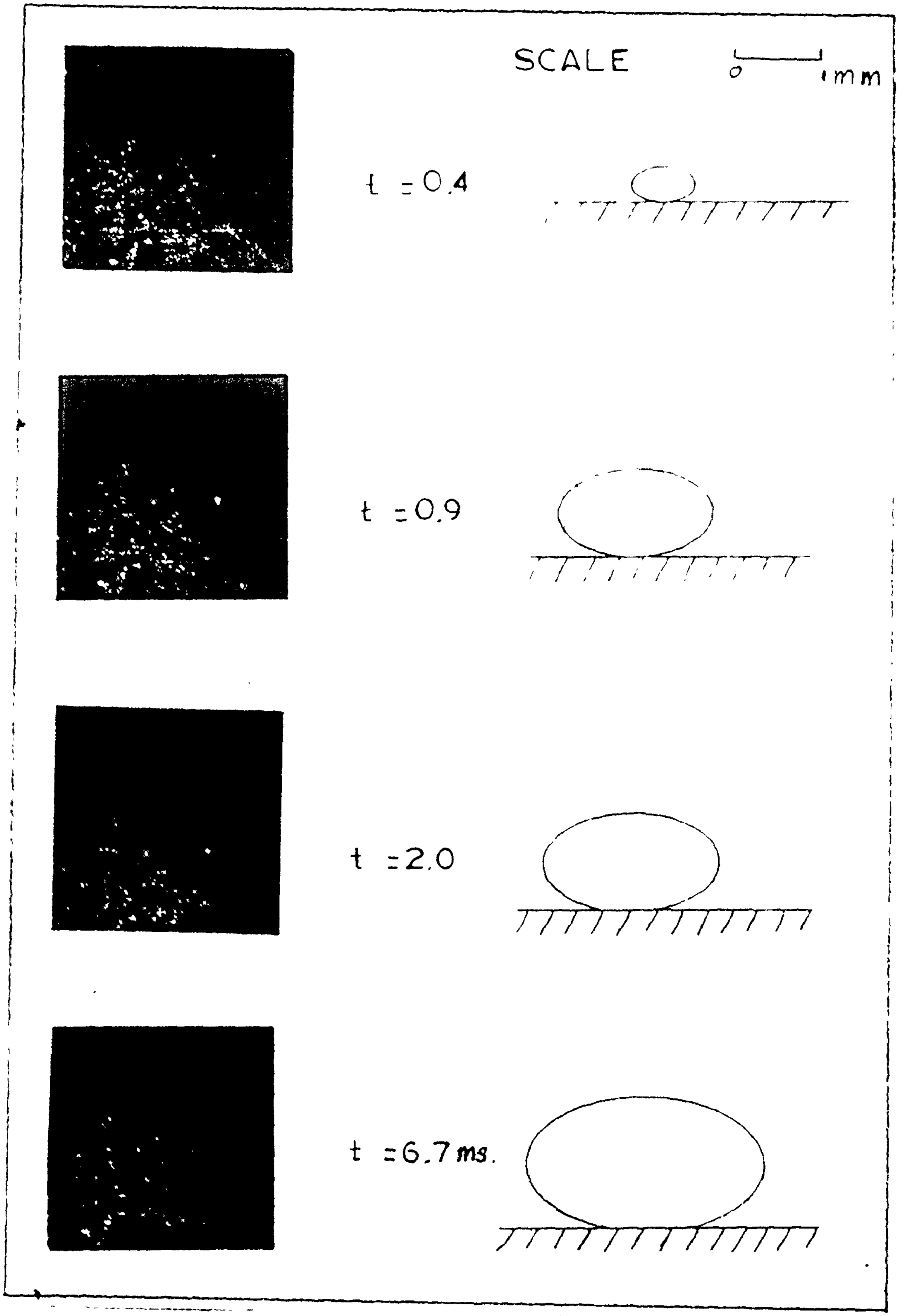

Figure 25

PRINTS OF THE INTERFEROGRAMS OF THE DATA POINT (2,4)

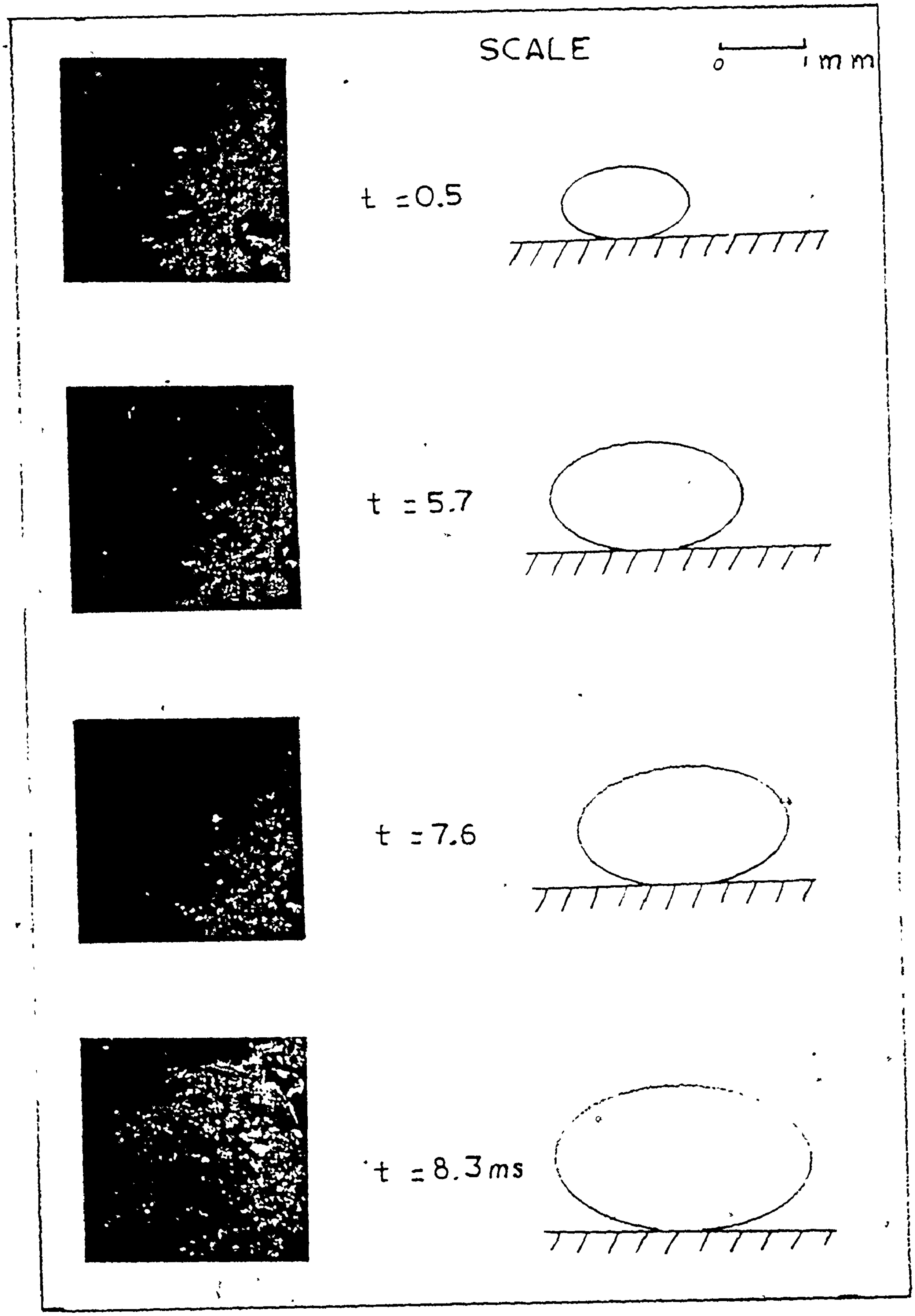

Figure 26

PRINTS OF THE INTERFEROGRAMS OF THE DATA POINT (3,1)

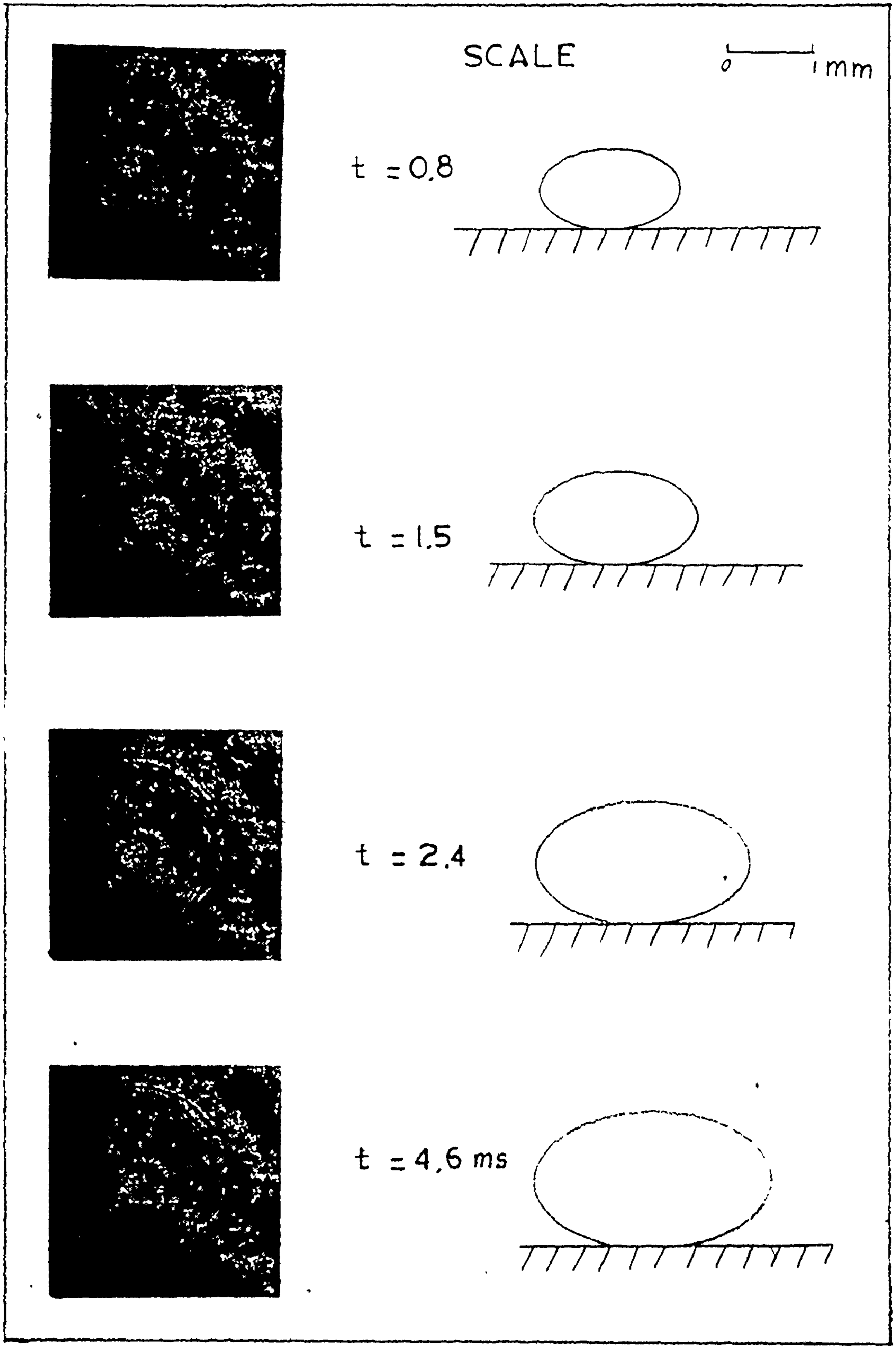

Figure 27

PRINTS OF THE INTERFEROGRAMS OF THE DATA POINT (3,2)

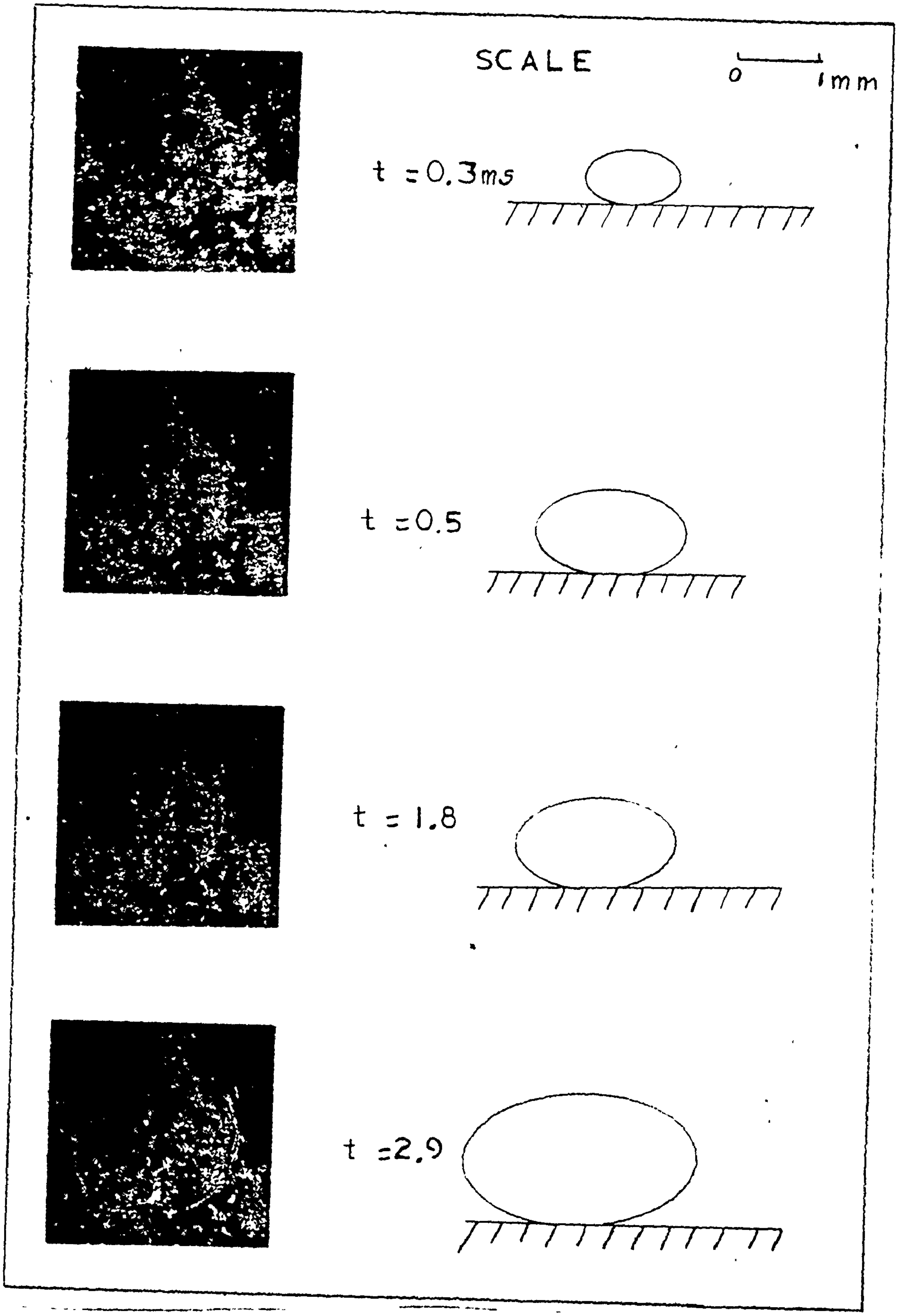

Figure 28
PRINTS OF THE INTERFEROGRAMS OF THE DATA POINT (3,3)

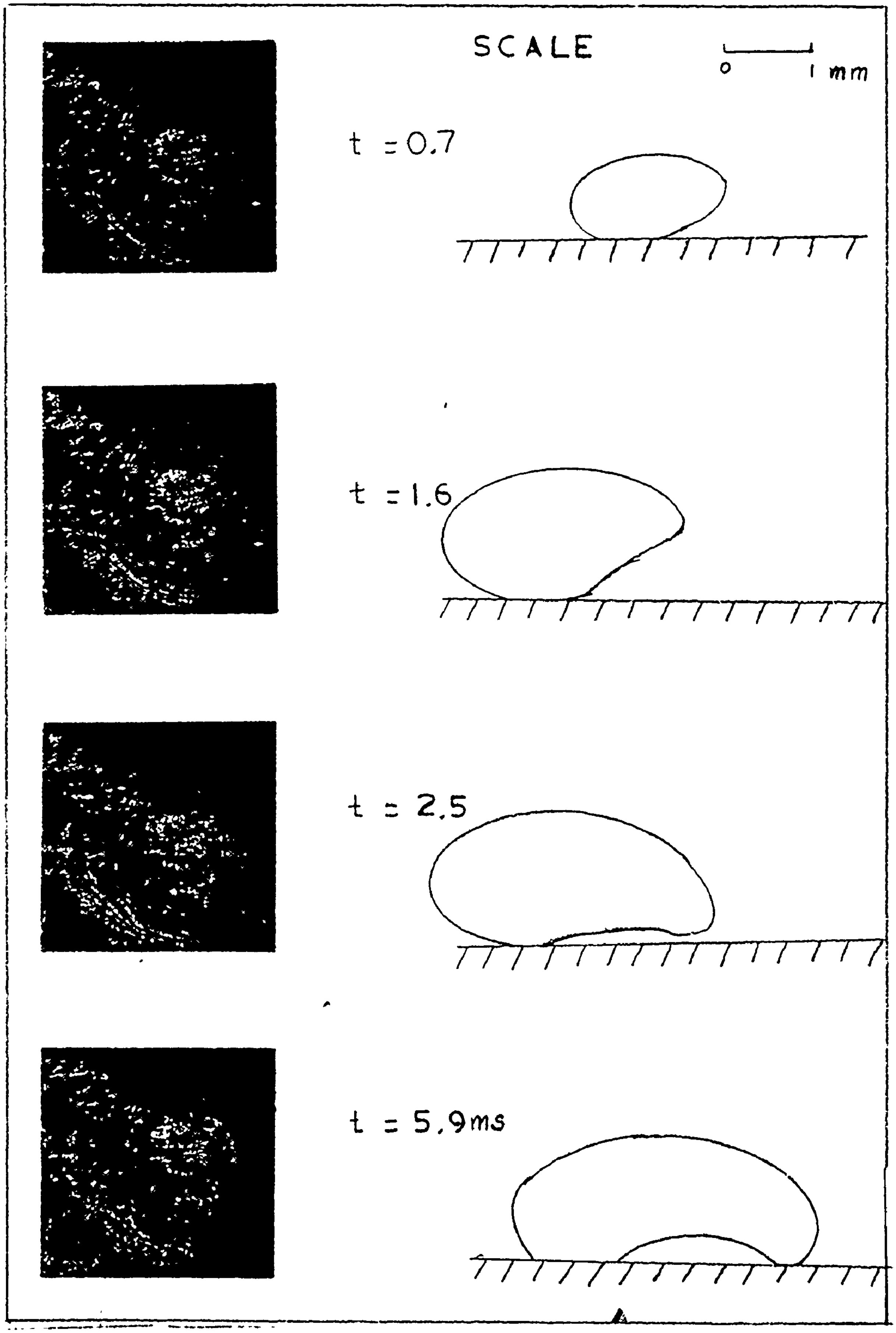

Figure 29

PRINTS OF THE INTERFEROGRAMS OF THE DATA POINT (3,4)

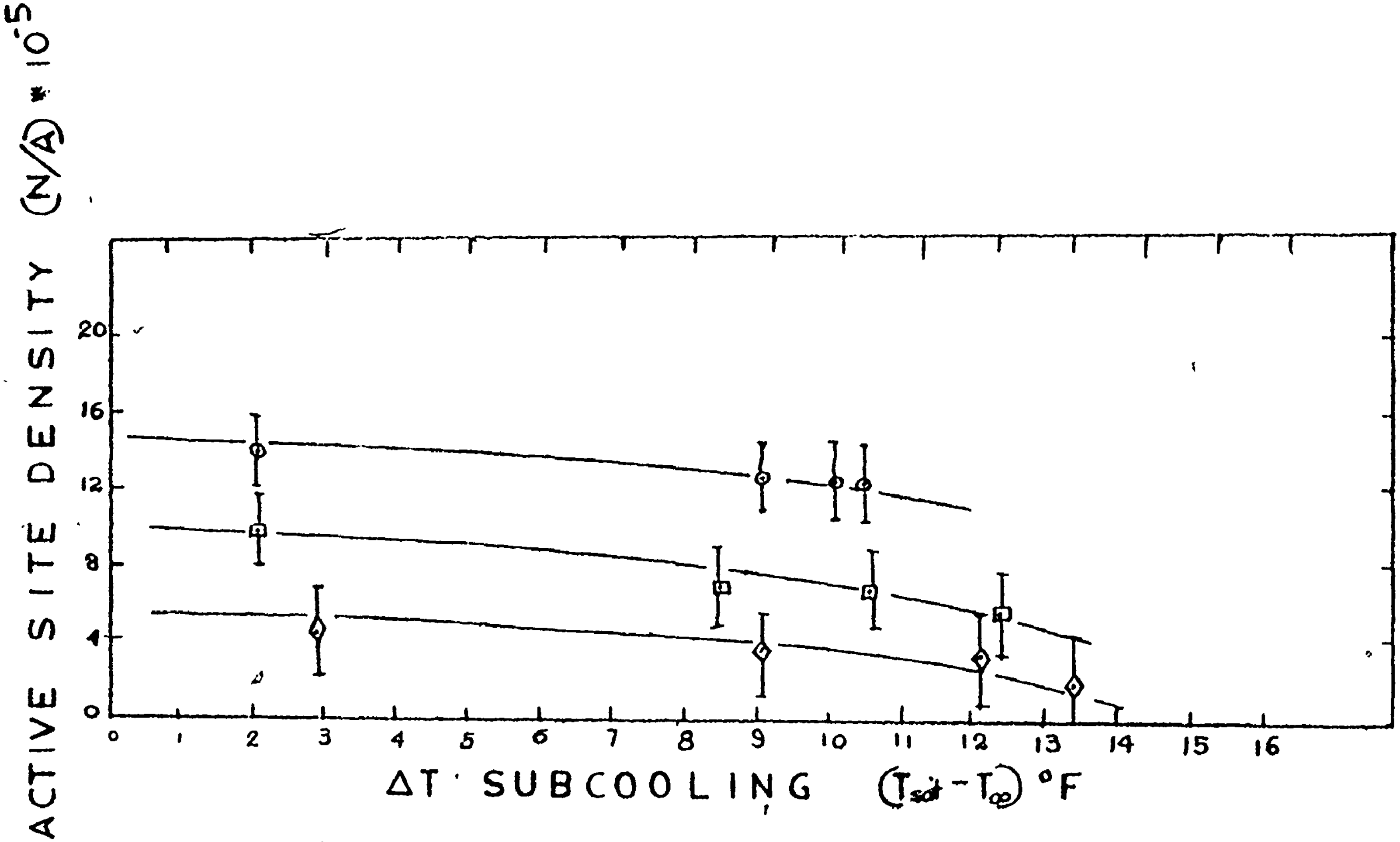

⊙ q/A = 19,000 Btu/hr ft^2
⊡ q/A = 13,200 Btu/hr ft^2
◇ q/A = 8,600 Btu/hr ft^2

Figure 30 ACTIVE SITE DENSITY

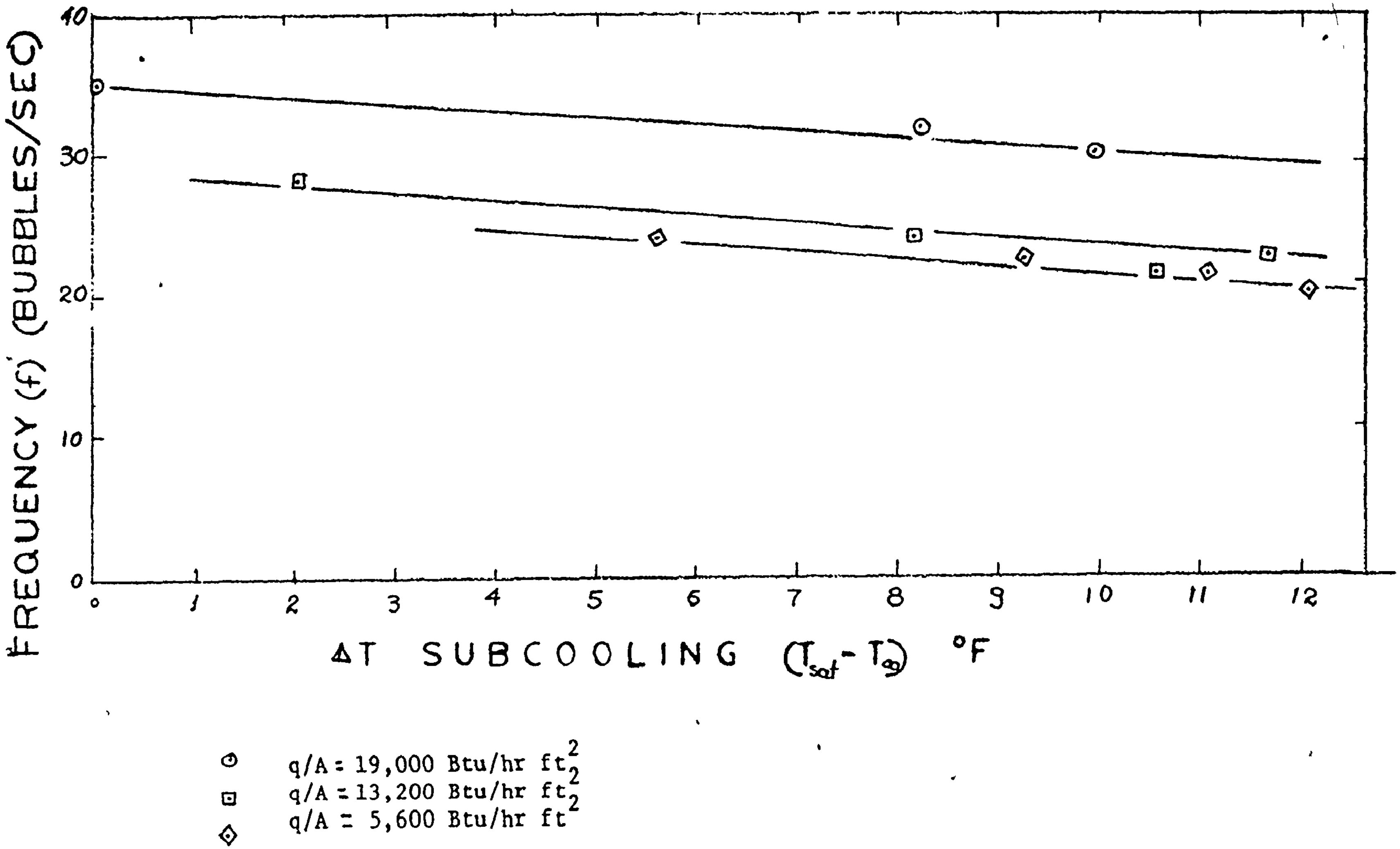

Figure 31 BUBBLE FREQUENCY

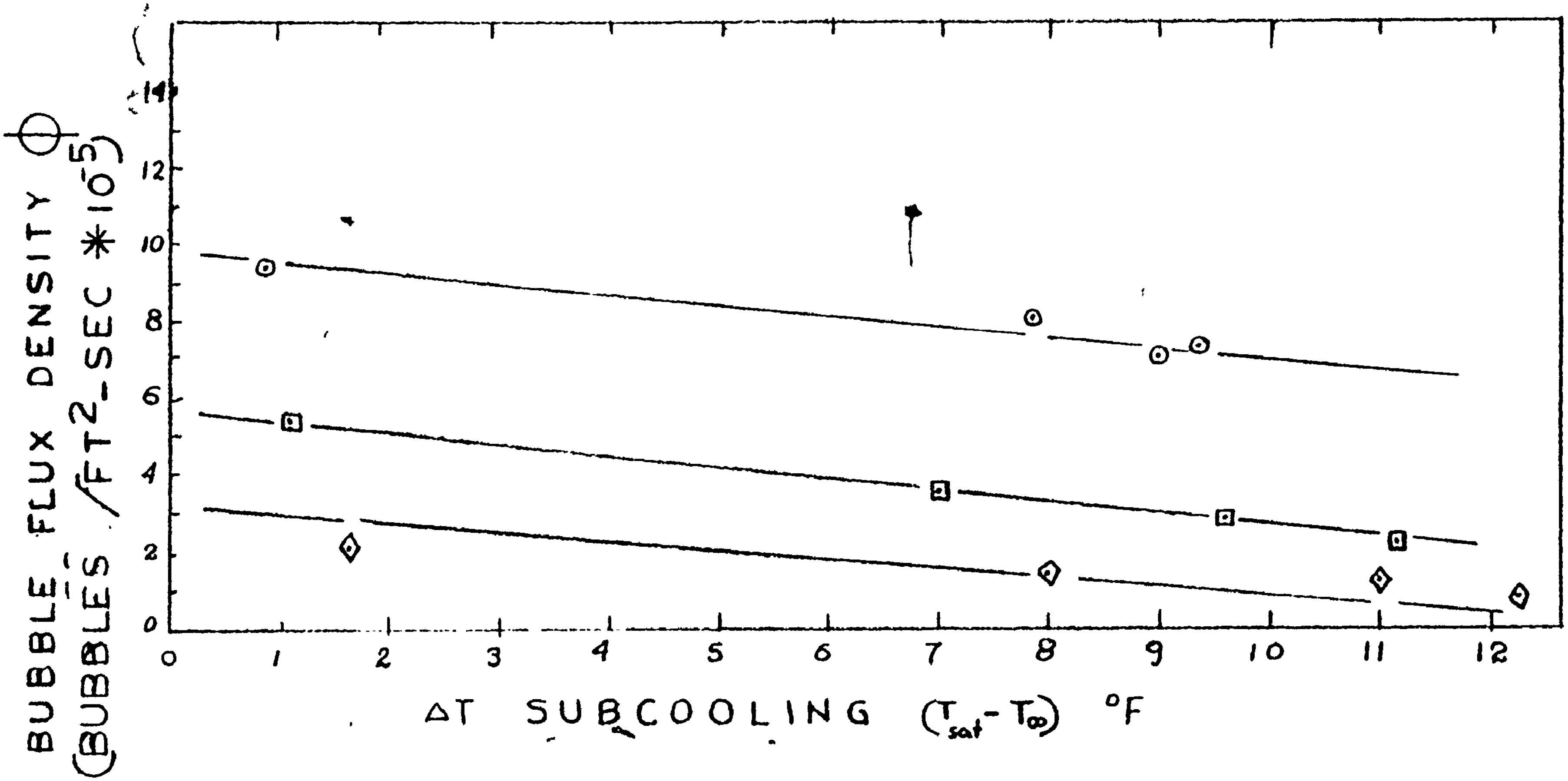

⊙ q/A 19,000 Btu/hr ft^2
⊡ q/A 13,200 Btu/hr ft^2
◇ q/A 8,600 Btu/hr ft^2

Figure 32 BUBBLE FLUX

The results of the analysis of the maximum bubble size, are summarized in Figure 33. The maximum size is obtained by measuring the maximum diameter attained by the vapour bubbles while attached to the heat transfer surface. Care has been taken to distinguish between vapour bubbles which departed from the heat transfer surface, and those which collapsed in order to exclude the later. The maximum bubble size results are presented as a function of subcooling for various values of constant heat flux.

Figures 34 to 45 illustrate the variation of the instantaneous microlayer thickness $\delta(r,t)$ with elapsed time and depicts the initial microlayer thickness $\delta_o(r)$ obtained by plotting the locus of points at which the gradient $\partial\delta(r,t)/\partial r$ approaches infinity. Each one of these figures contains microlayer profiles for one specific combination of heat flux and subcooling.
Boiling did occur only for the three higher heat flux values for all levels of subcooling. Therefore, the microlayer evaporation data included here contains only 12 combinations of heat flux and subcooling, out of 24 combinations that were examined.

Each of figures 46, 47 and 48 illustrate the influence of subcooling upon the initial microlayer thickness $\delta_o(r)$ for a constant heat flux.

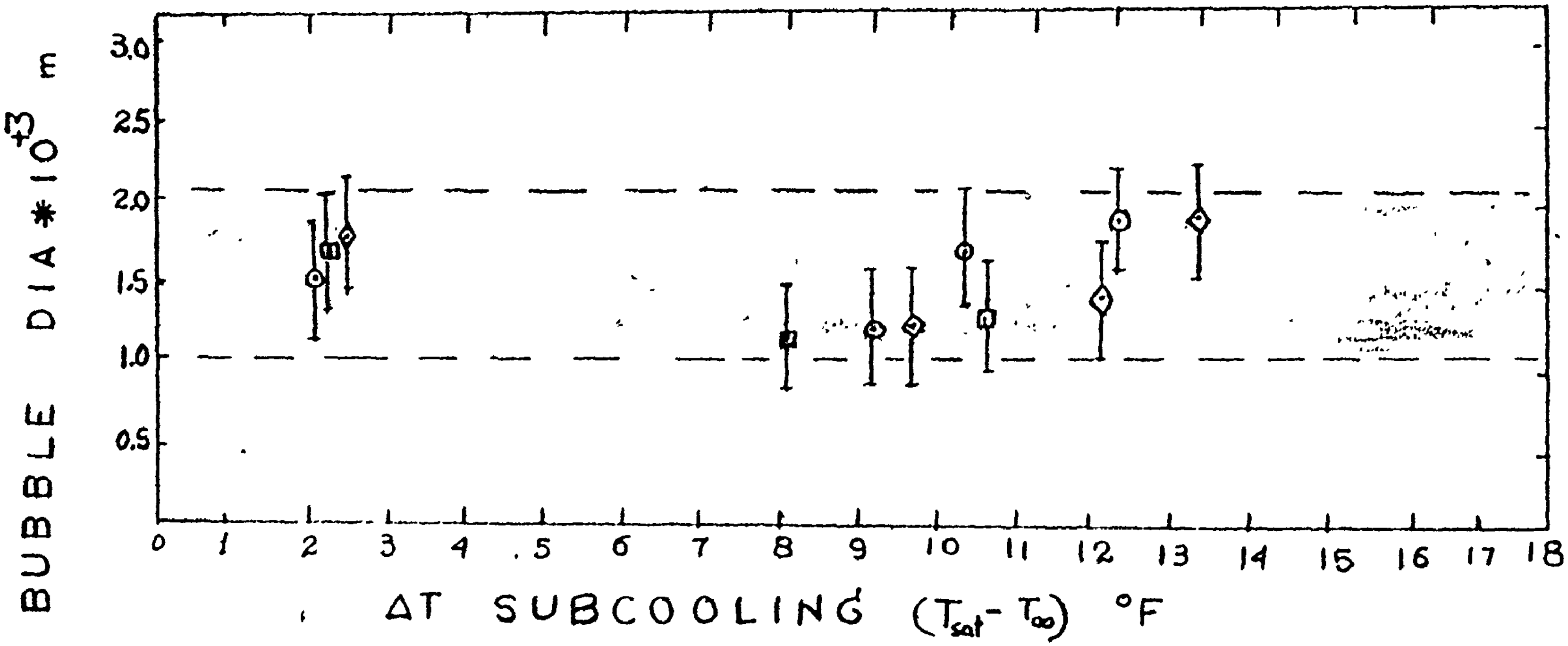

⊙ q/A 19,000 Btu/hr ft^2
⊡ q/A 13,200 Btu/hr ft^2
◇ q/A 8,600 Btu/hr ft^2

Figure 33 MAXIMUM BUBBLE SIZE

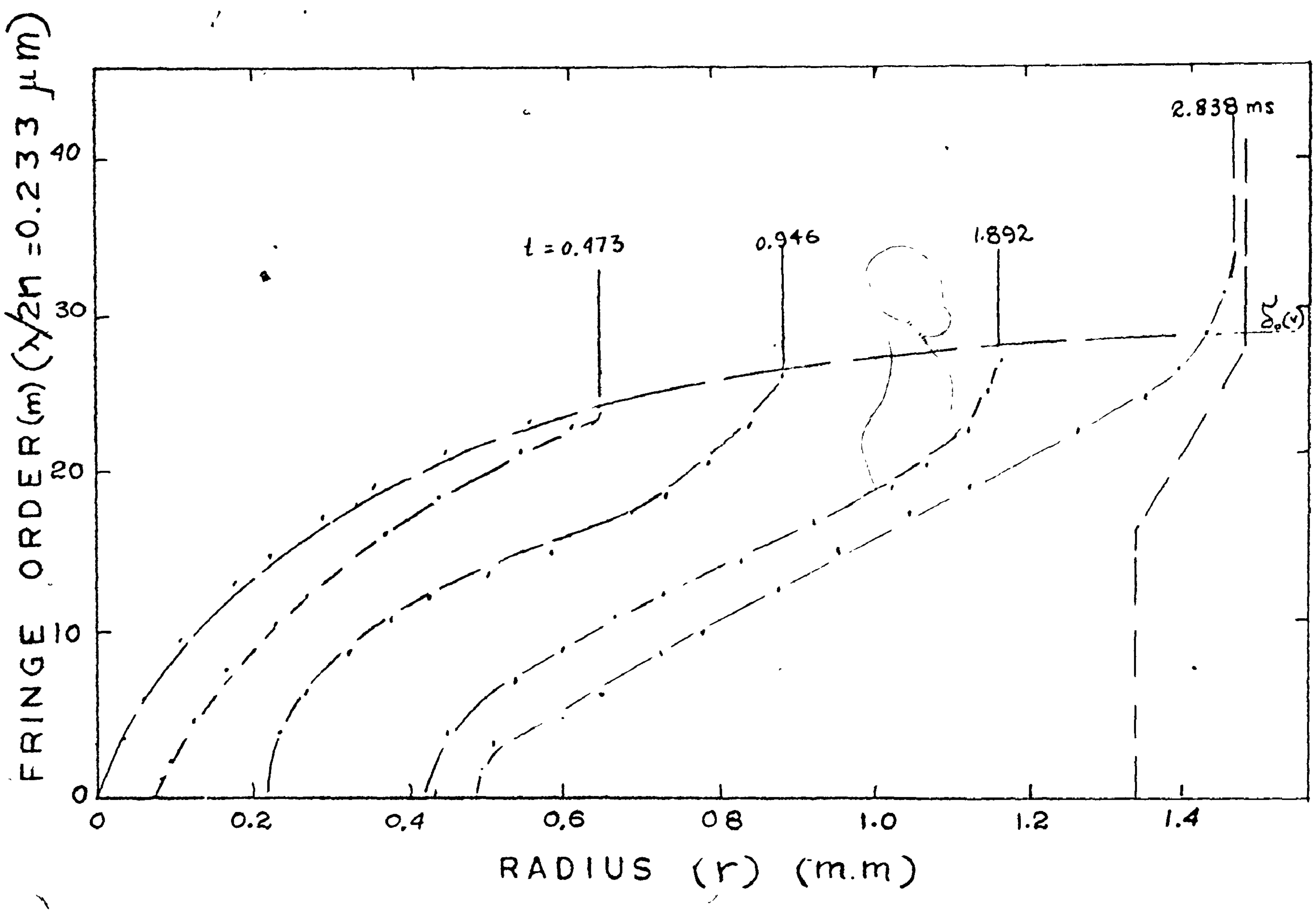

Figure 34 MICROLAYER PROFILE FOR DATA POINT (1,1)

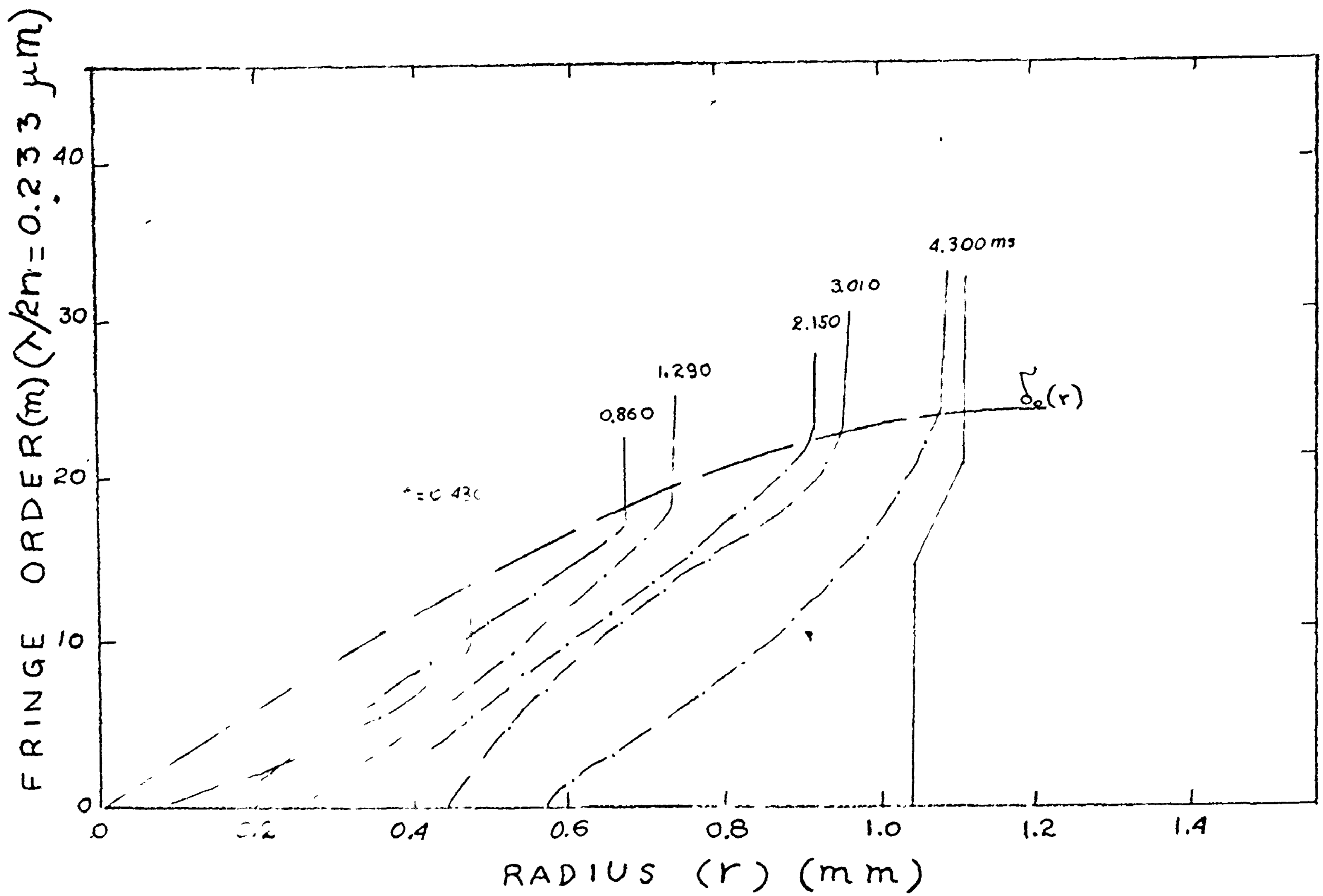

Figure 35 MICROLAYER PROFILE FOR DATA POINT (1,2)

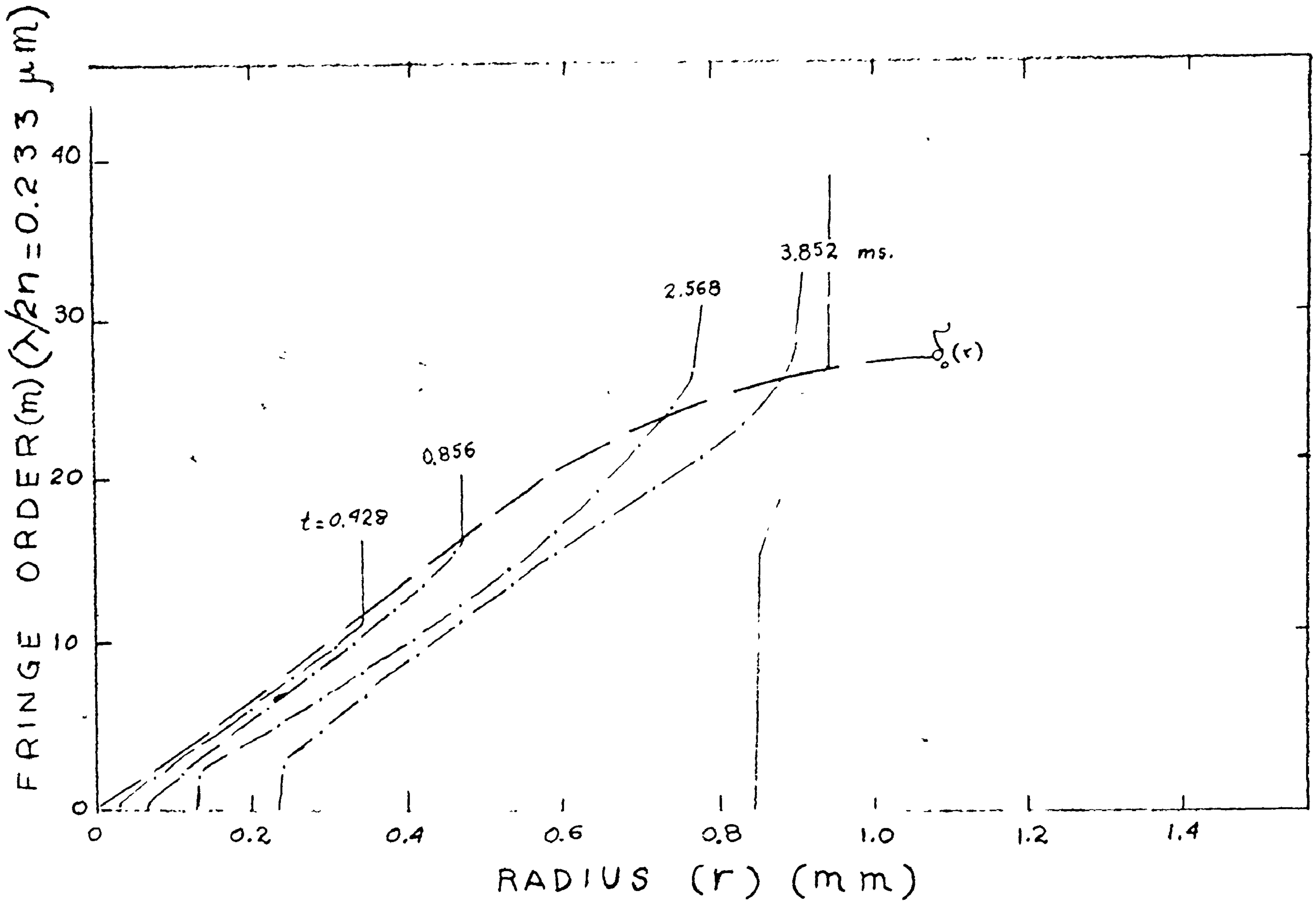

Figure 36 MICROLAYER PROFILE FOR DATA POINT (1,3)

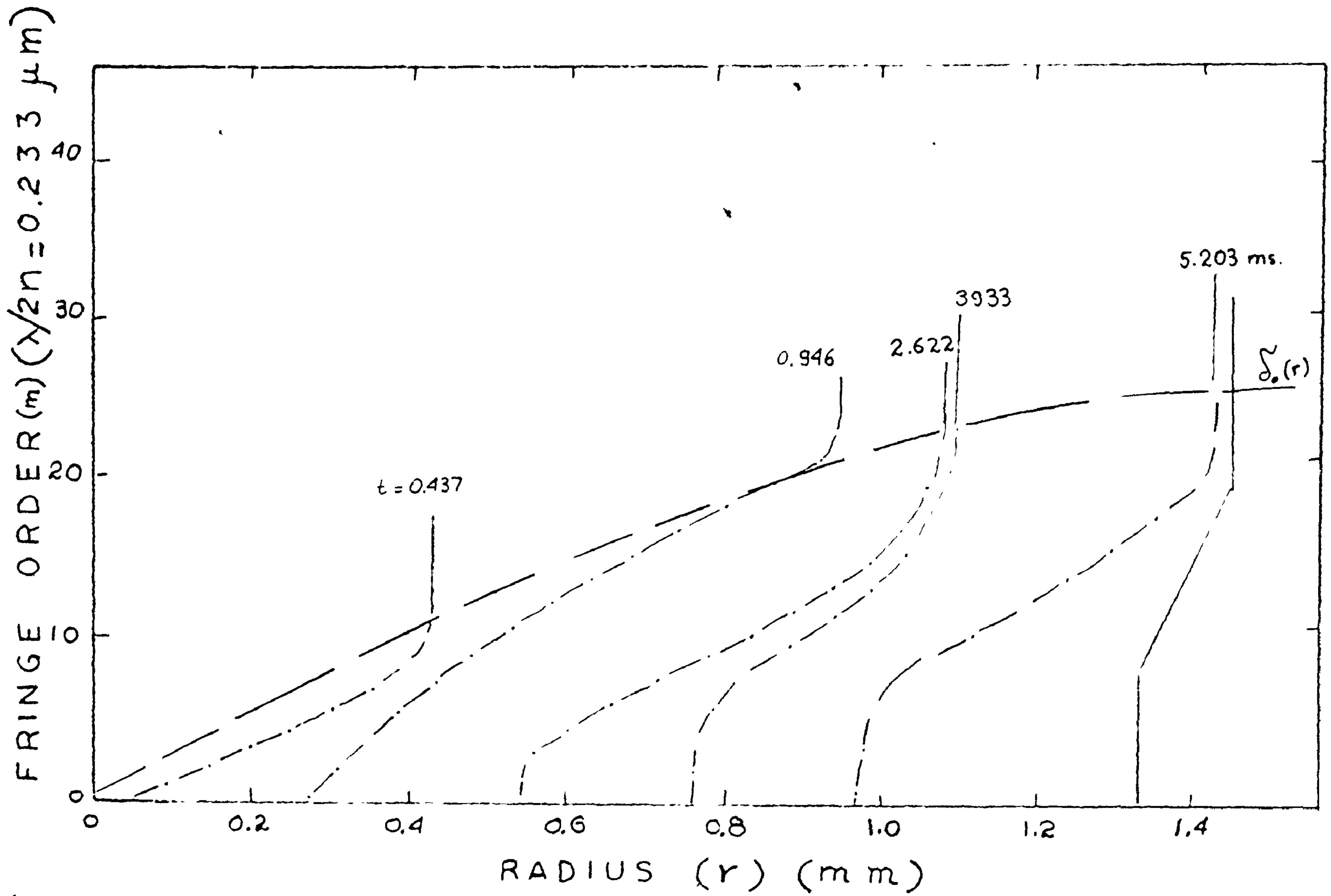

Figure 37 MICROLAYER PROFILE FOR DATA POINT (1,4)

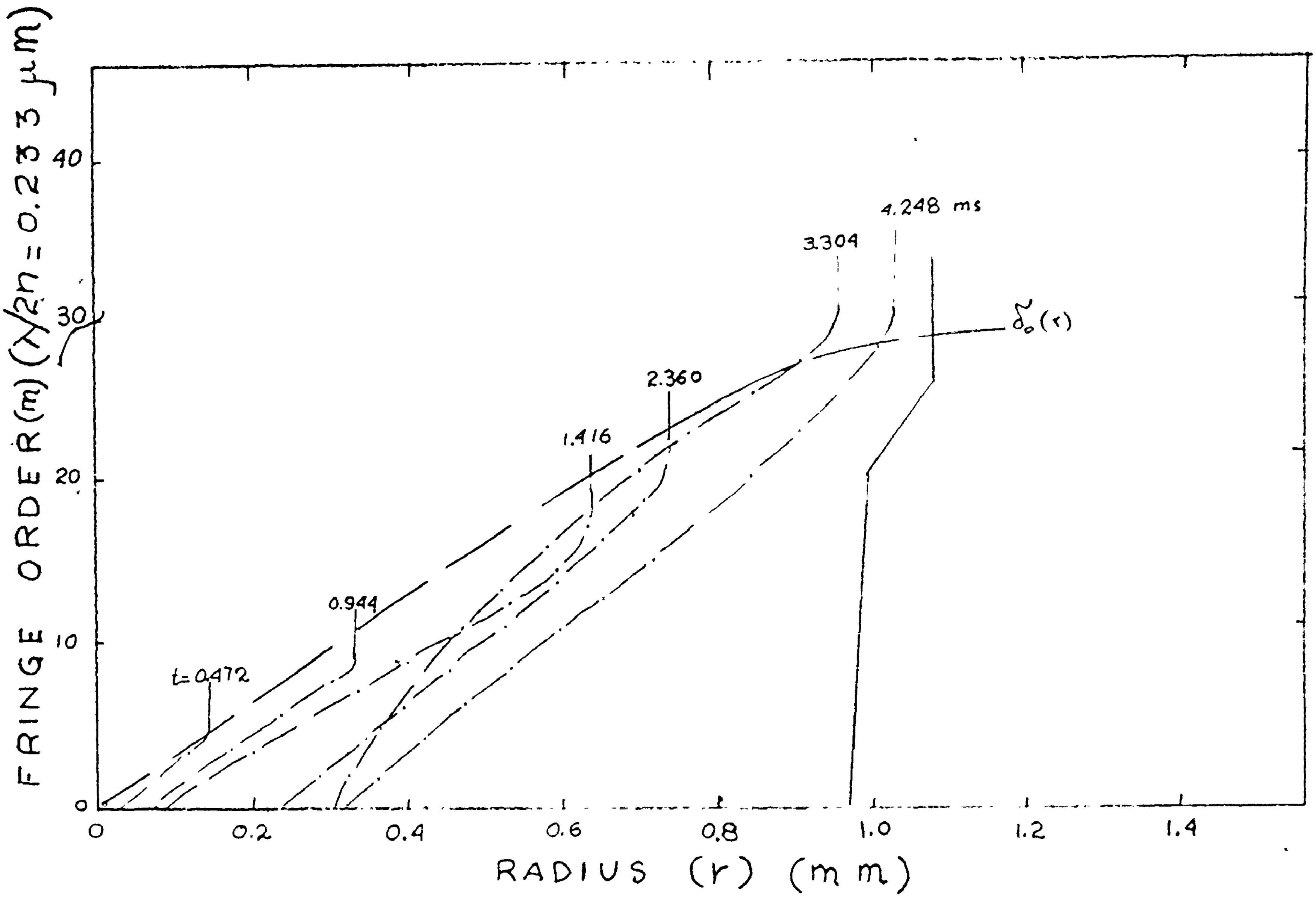

Figure 38 MICROLAYER PROFILE FOR DATA POINT (2,1)

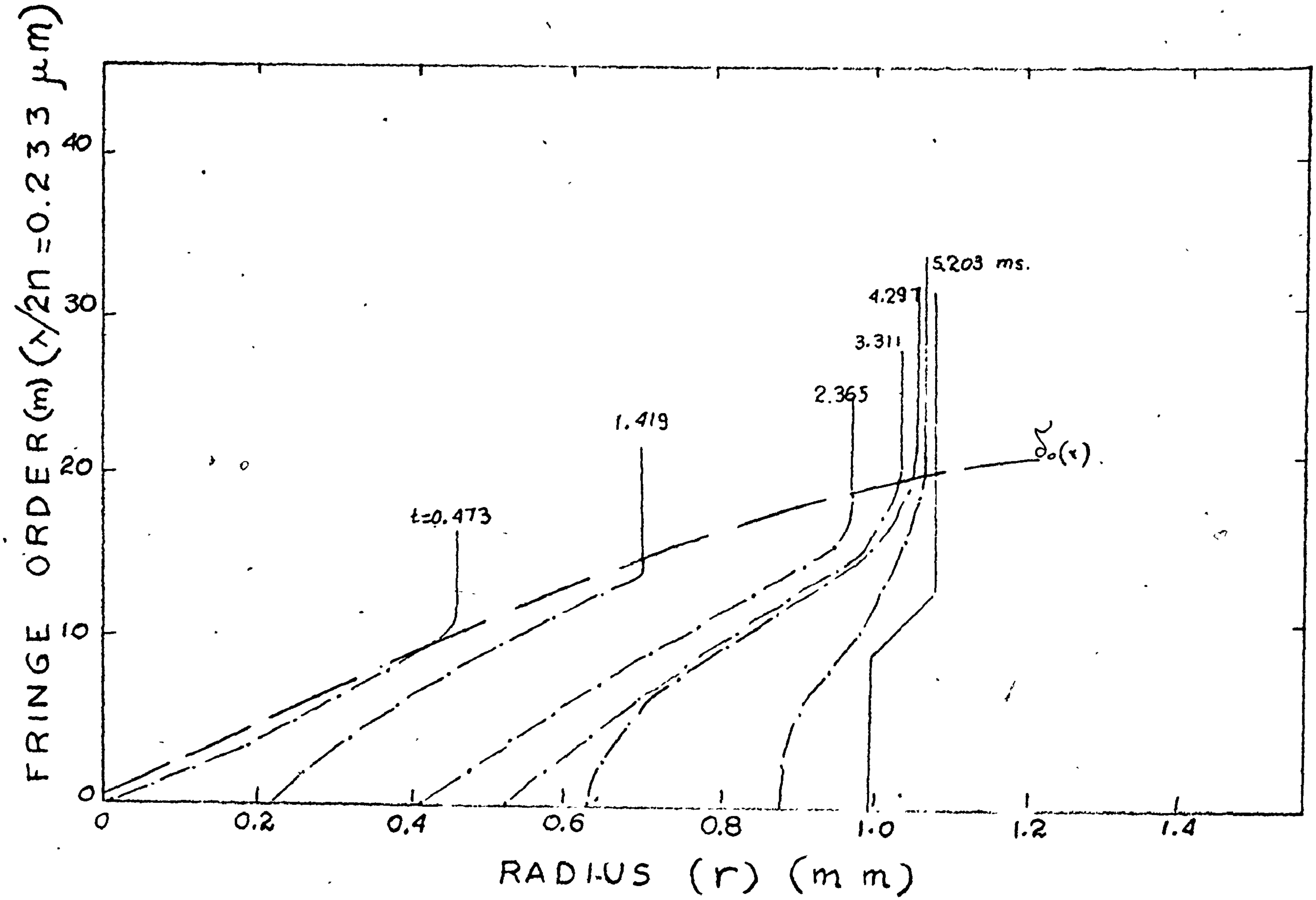

Figure 39 MICROLAYER PROFILE FOR DATA POINT (2,2)

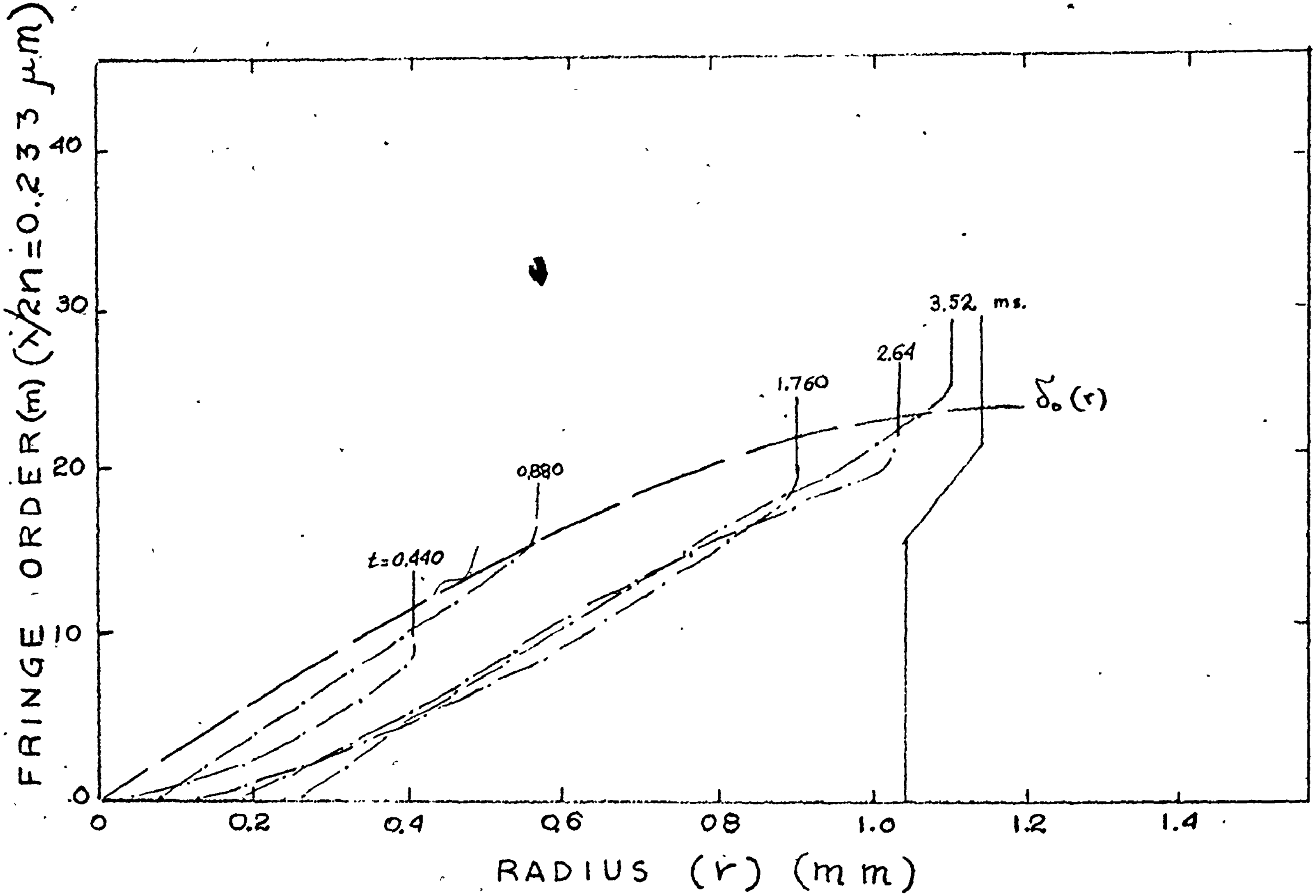

Figure 40 MICROLAYER PROFILE FOR DATA POINT (2,3)

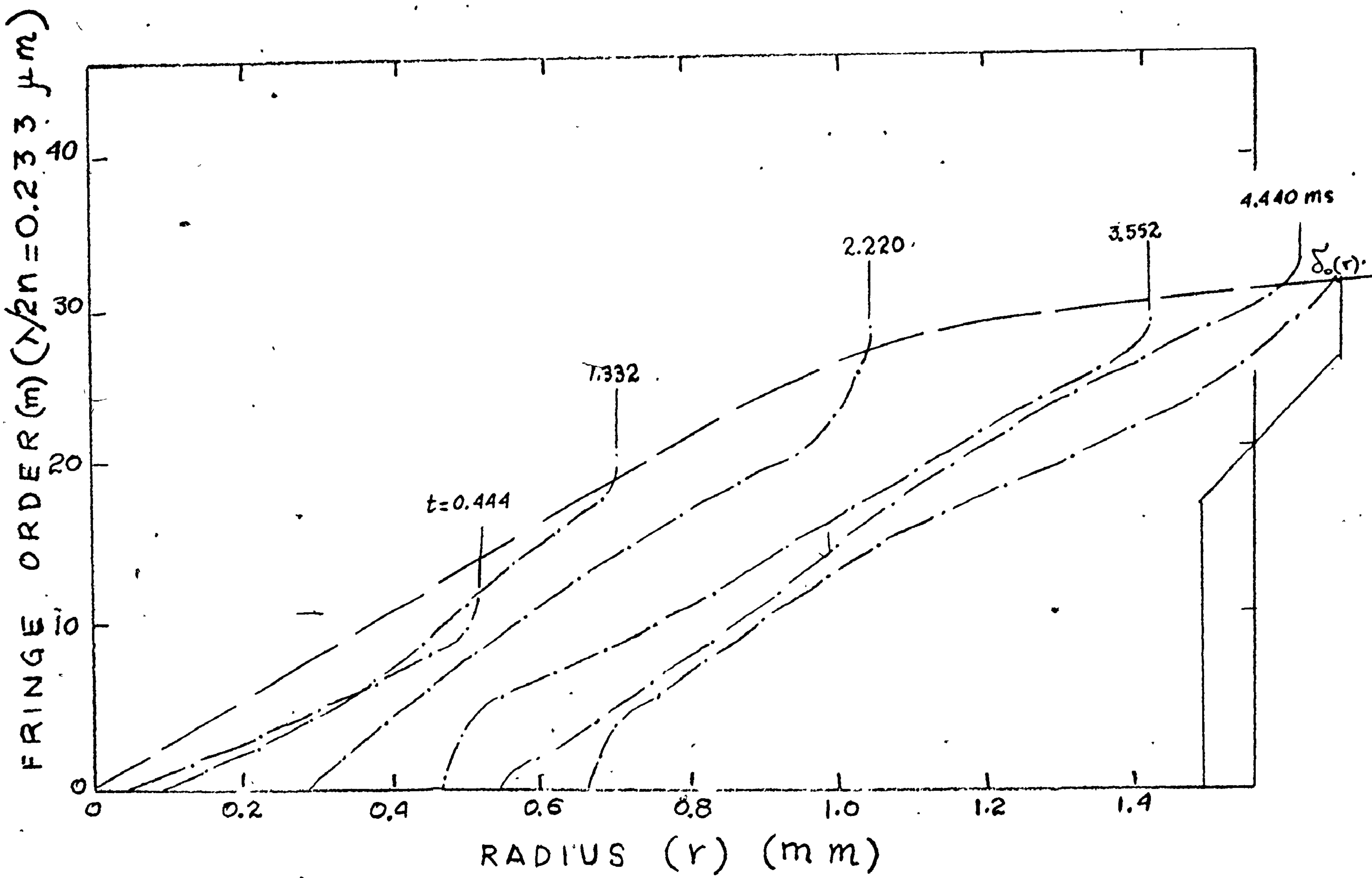

Figure 41 MICROLAYER PROFILE FOR DATA POINT (2,4)

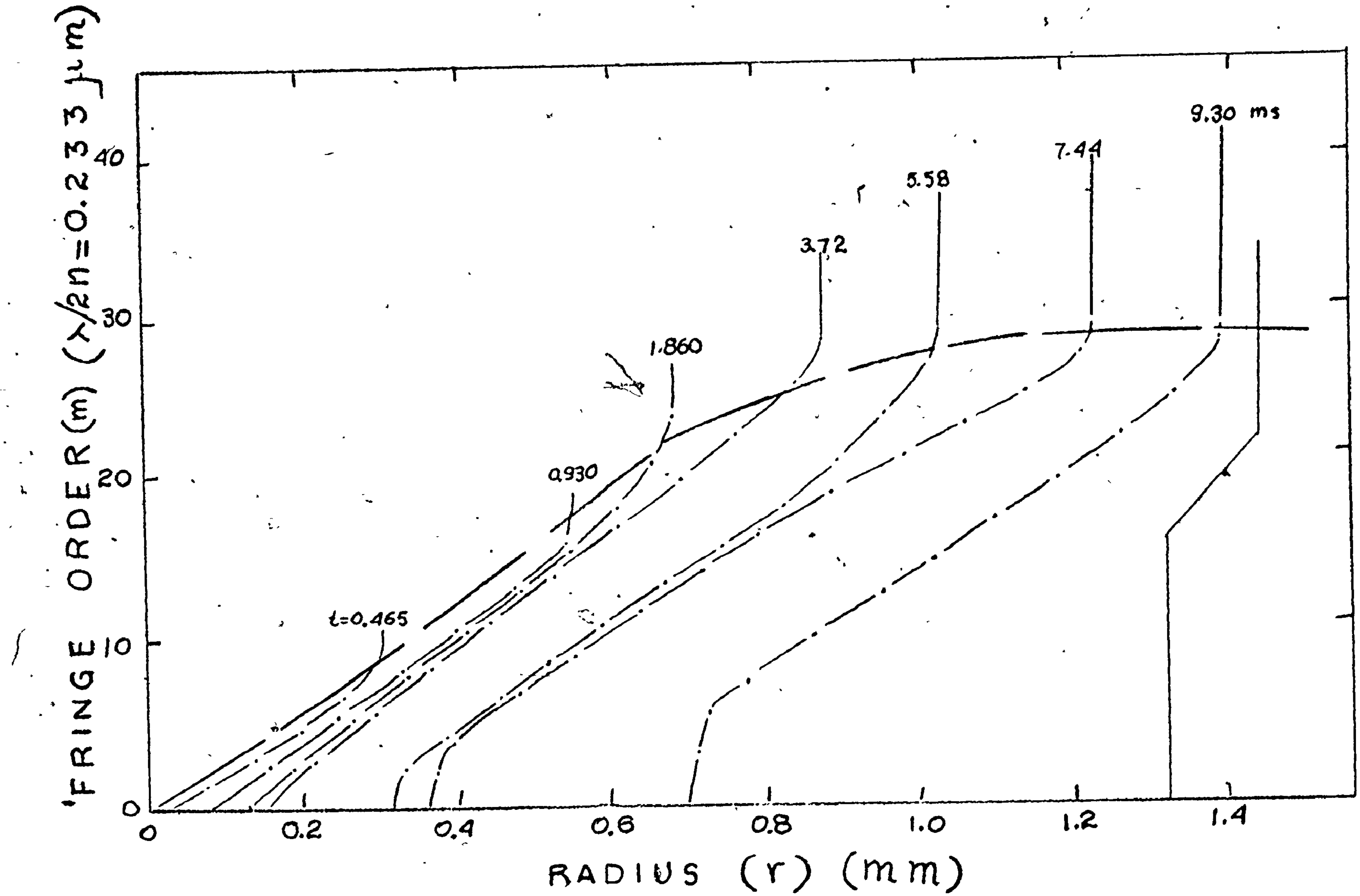

Figure 42 MICROLAYER PROFILE FOR DATA POINT (3,1)

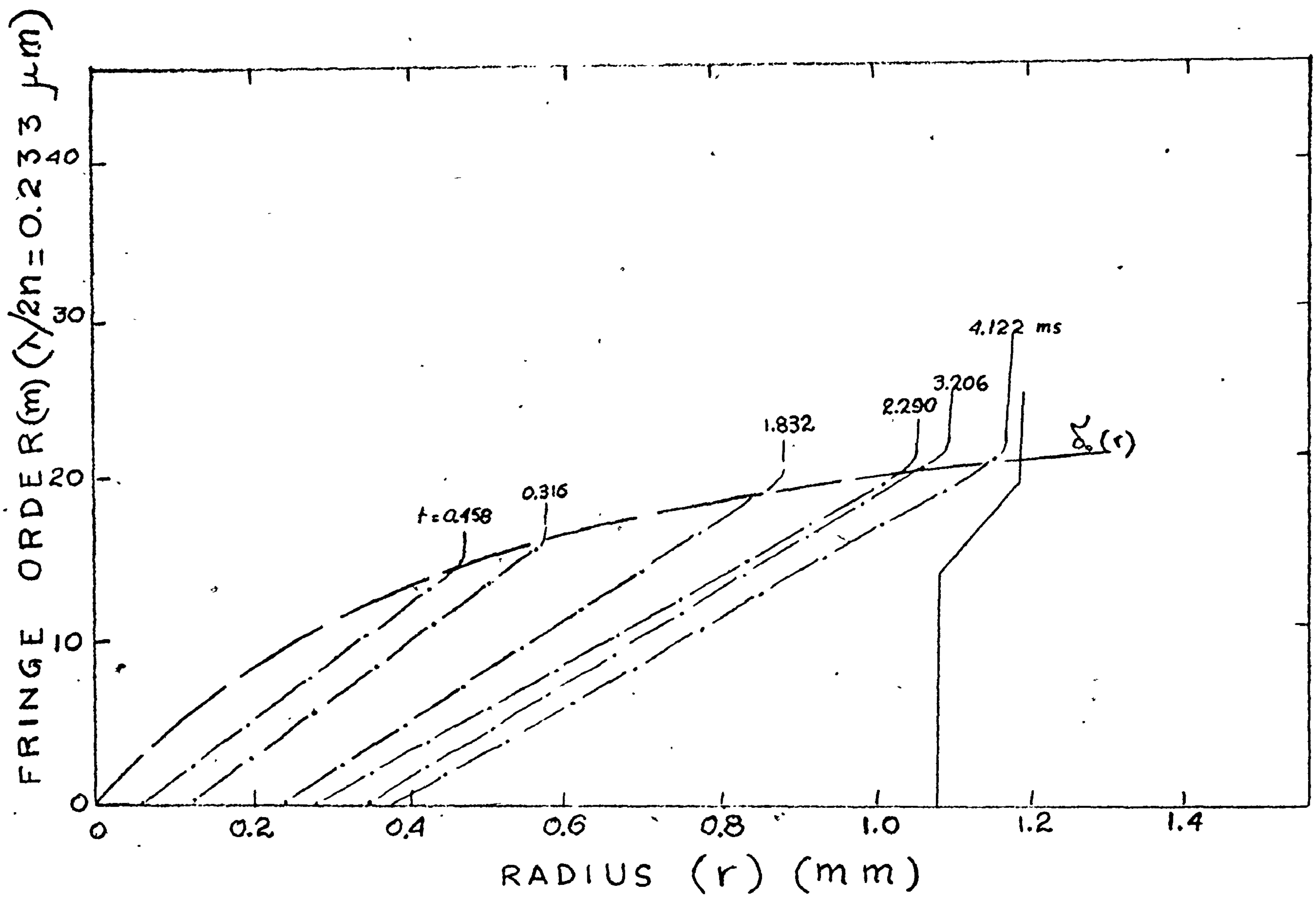

Figure 43 MICROLAYER PROFILE FOR DATA POINT (3,2)

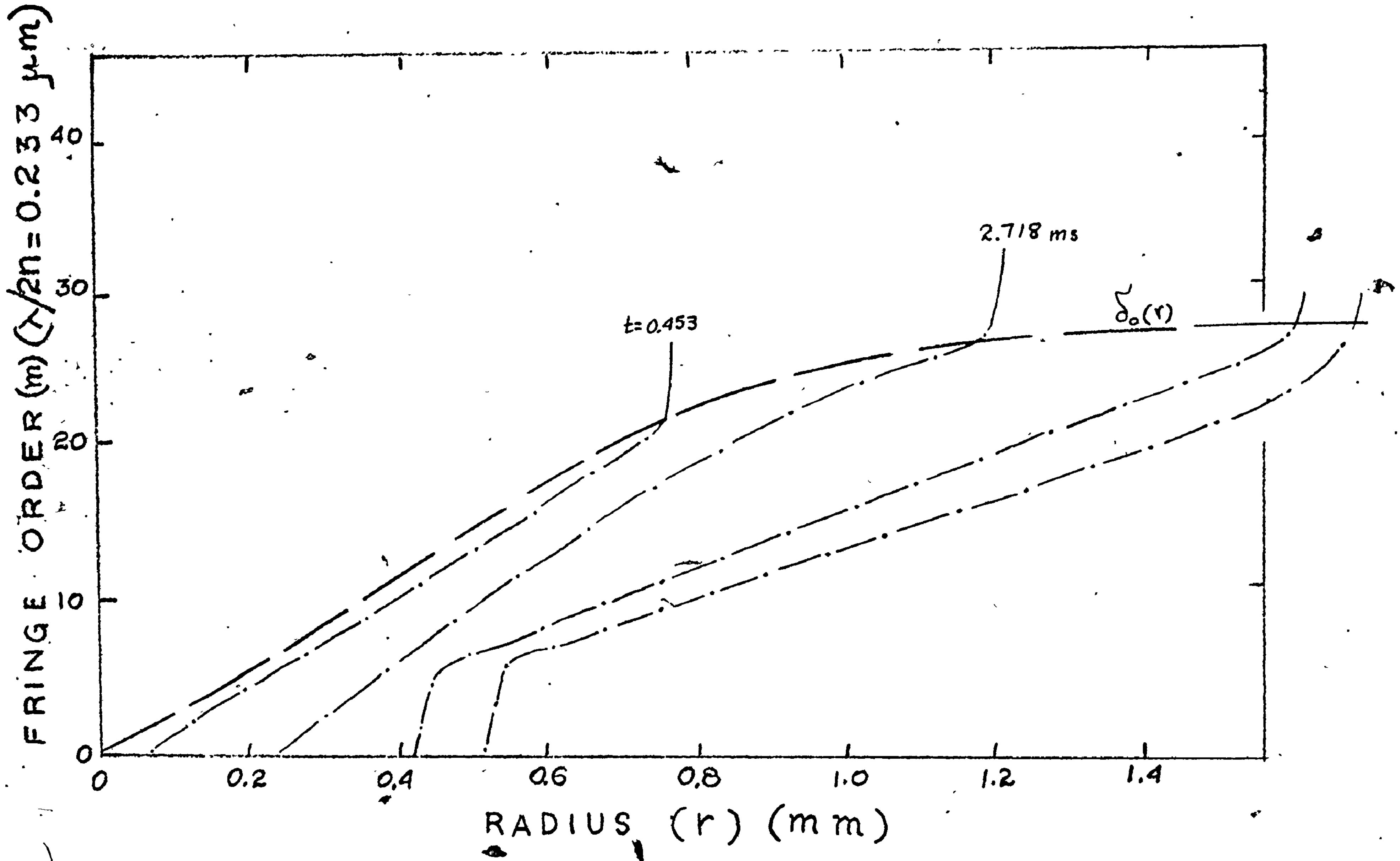

Figure 44 MICROLAYER PROFILE FOR DATA POINT (3,3)

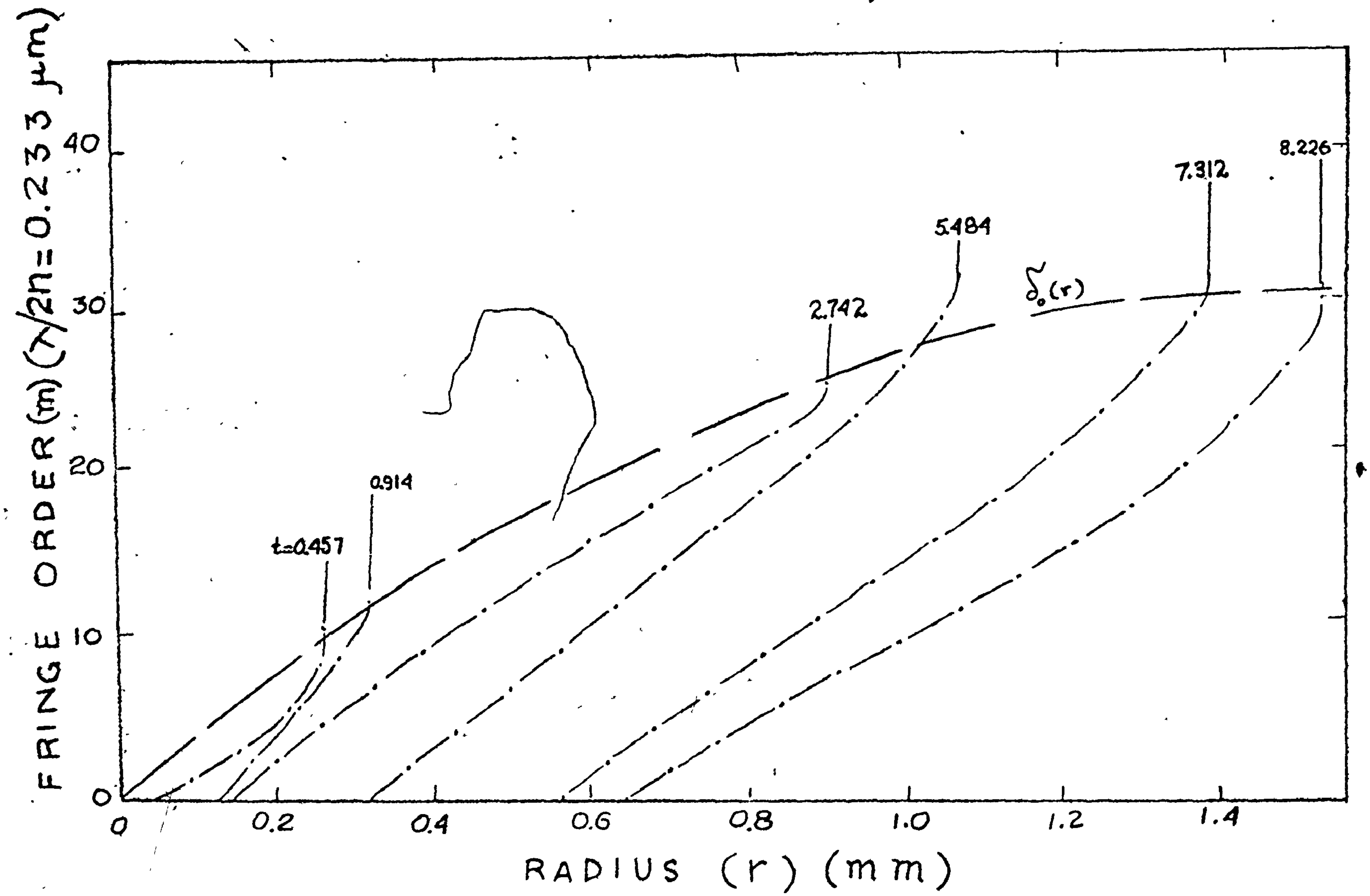

Figure 45 MICROLAYER PROFILE FOR DATA POINT (3,4)

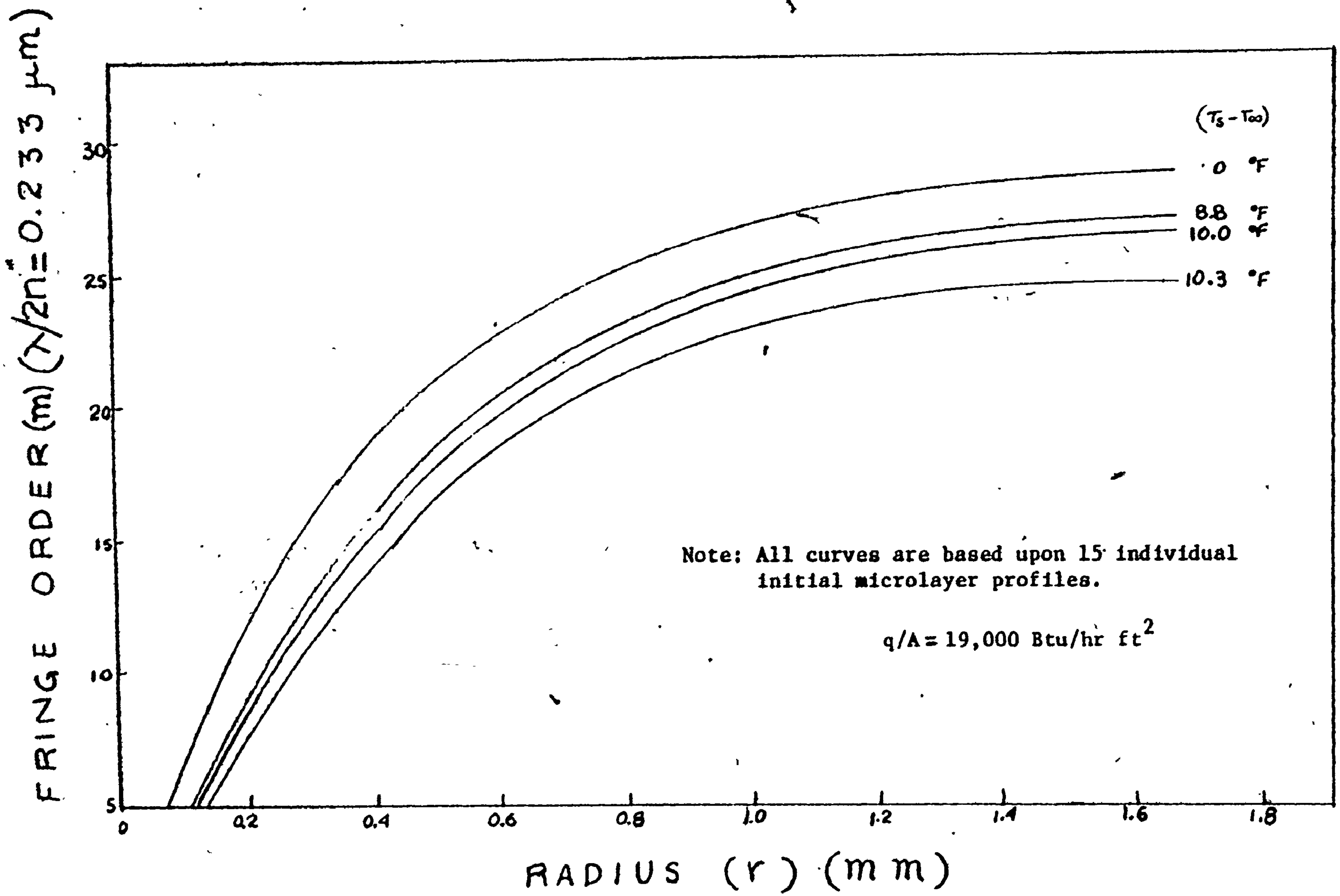

Figure 46 THE EFFECT OF SUBCOOLING ON THE INITIAL MICROLAYER PROFILES

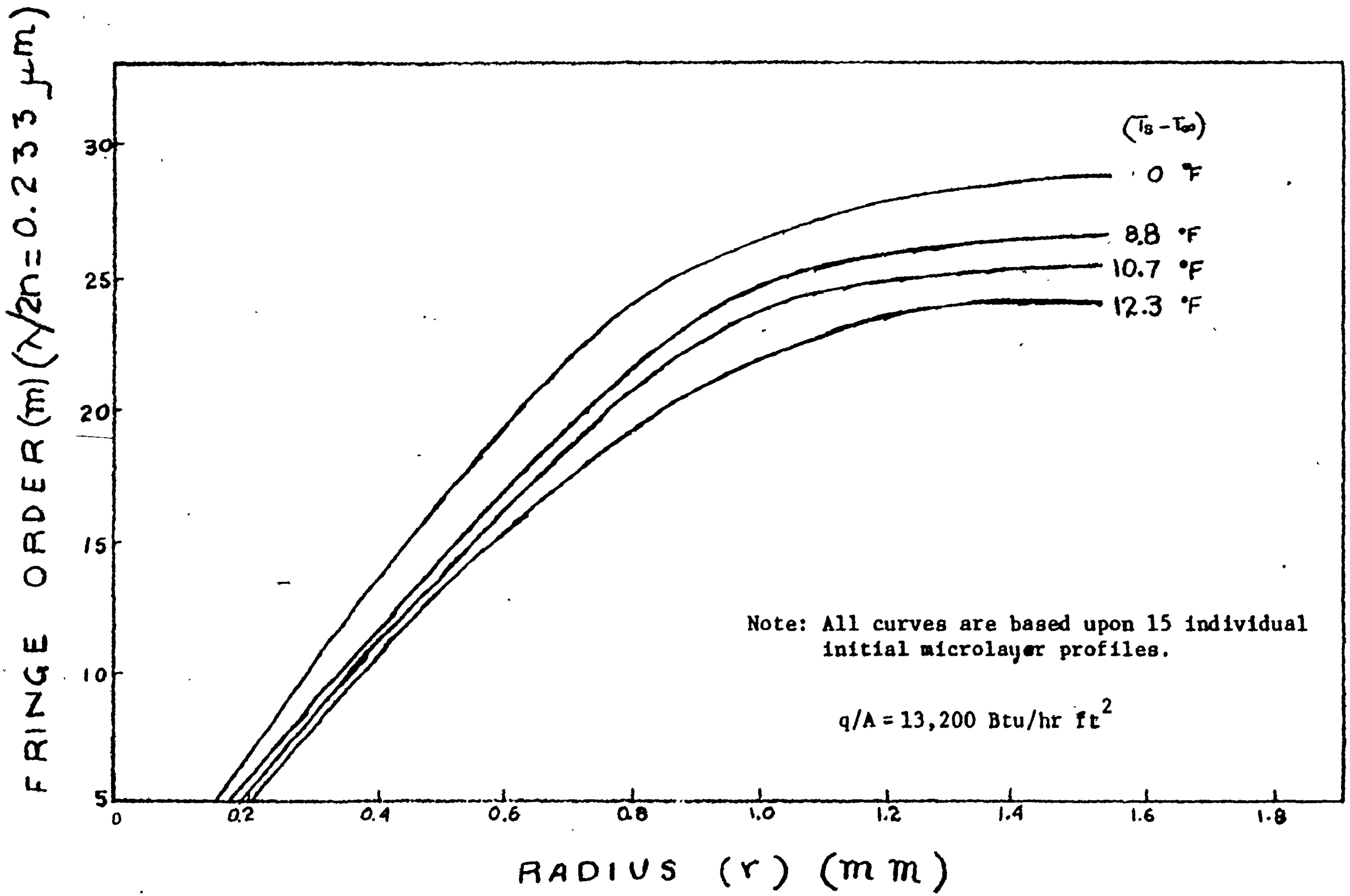

Figure 47 THE EFFECT OF SUBCOOLING ON THE INITIAL MICROLAYER PROFILES

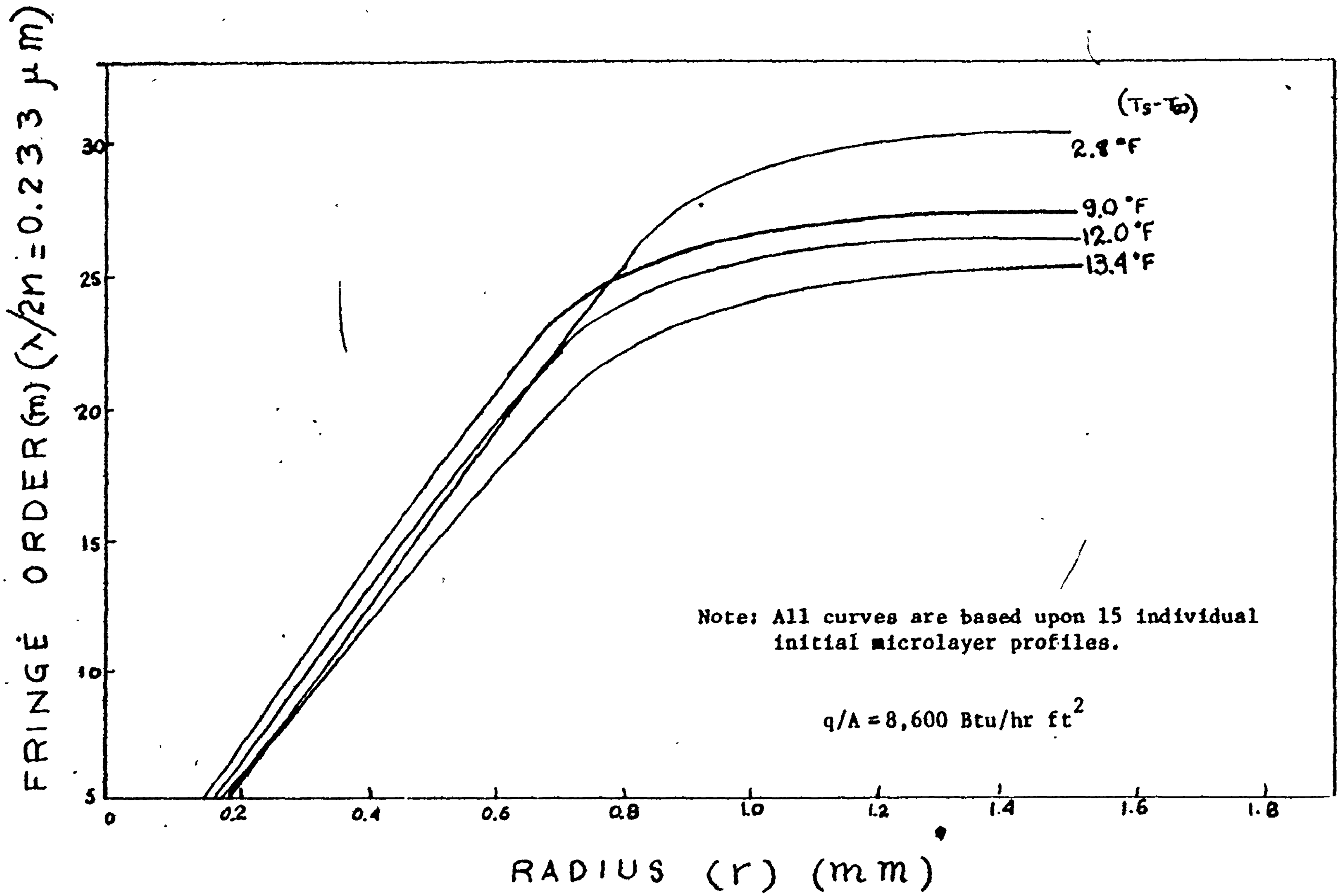

Figure 48 THE EFFECT OF SUBCOOLING ON THE INITIAL MICROLAYER PROFILES

Figures 49 to 52 present the results of the analysis which was performed to determine the percentage of heat transferred by microlayer evaporation. Figure 49 summarizes the volumes of liquid which were evaporated from the microlayer into the bubble. Each curve contains data plotted in the form of volume versus subcooling with the levels of heat flux as parameter. The amount of heat transfered through microlayer evaporation is presented in figure 50 as a function of subcooling. The levels of heat flux are again presented in such a way as to show the influence of both heat flux and subcooling upon the heat transferred by microlayer evaporation. Figure 51 presents plots of the percentage of heat transferred by microlayer evaporation as a function of subcooling. The effect of heat flux is also shown in figure 51 in parametric form. Finally figure 52 illustrates the effects of heat flux upon the heat transferred by microlayer evaporation while the influence of subcooling is shown in parametric form.

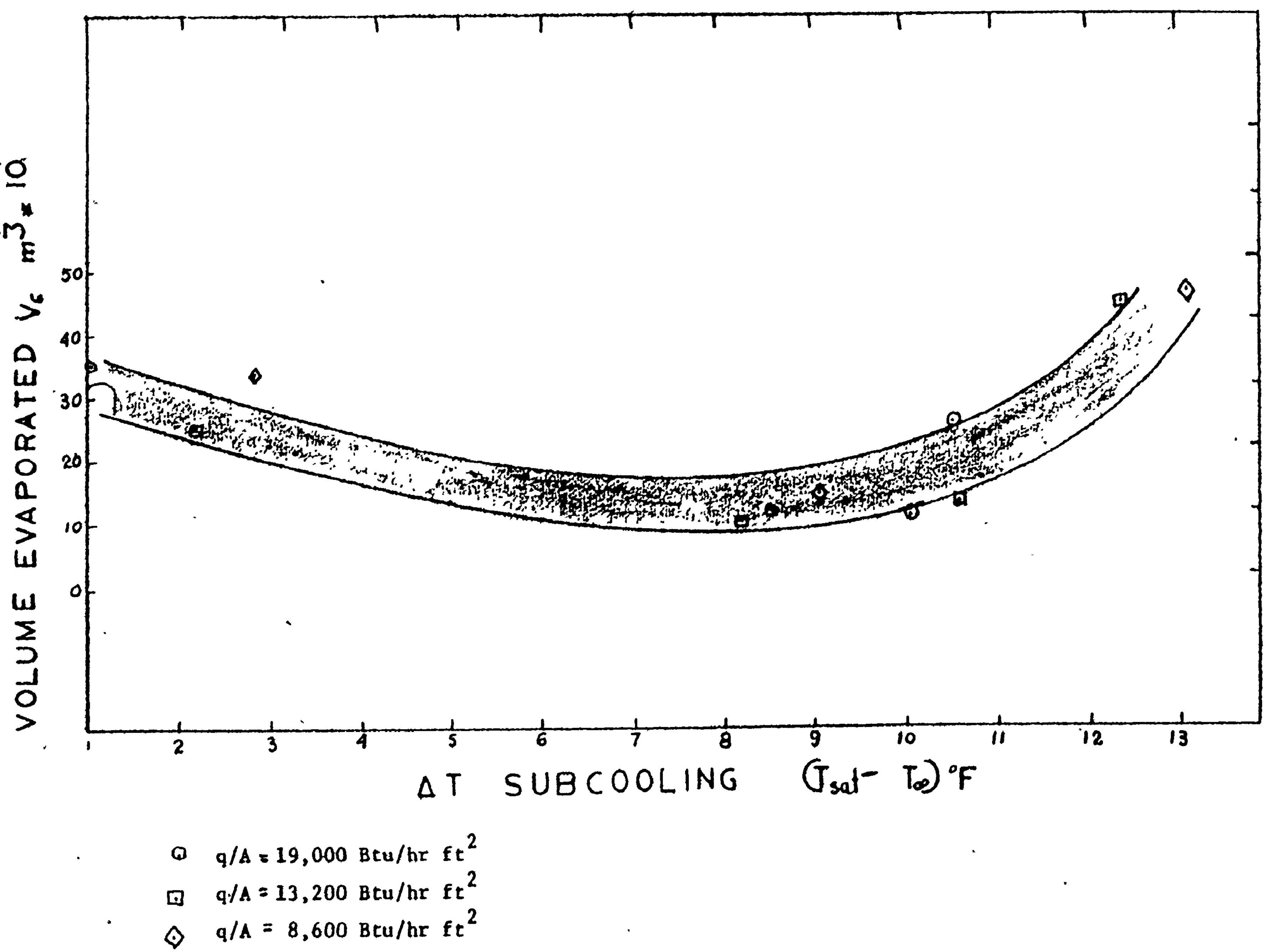

Figure 49 VOLUMES OF MICROLAYER LIQUID EVAPORATED

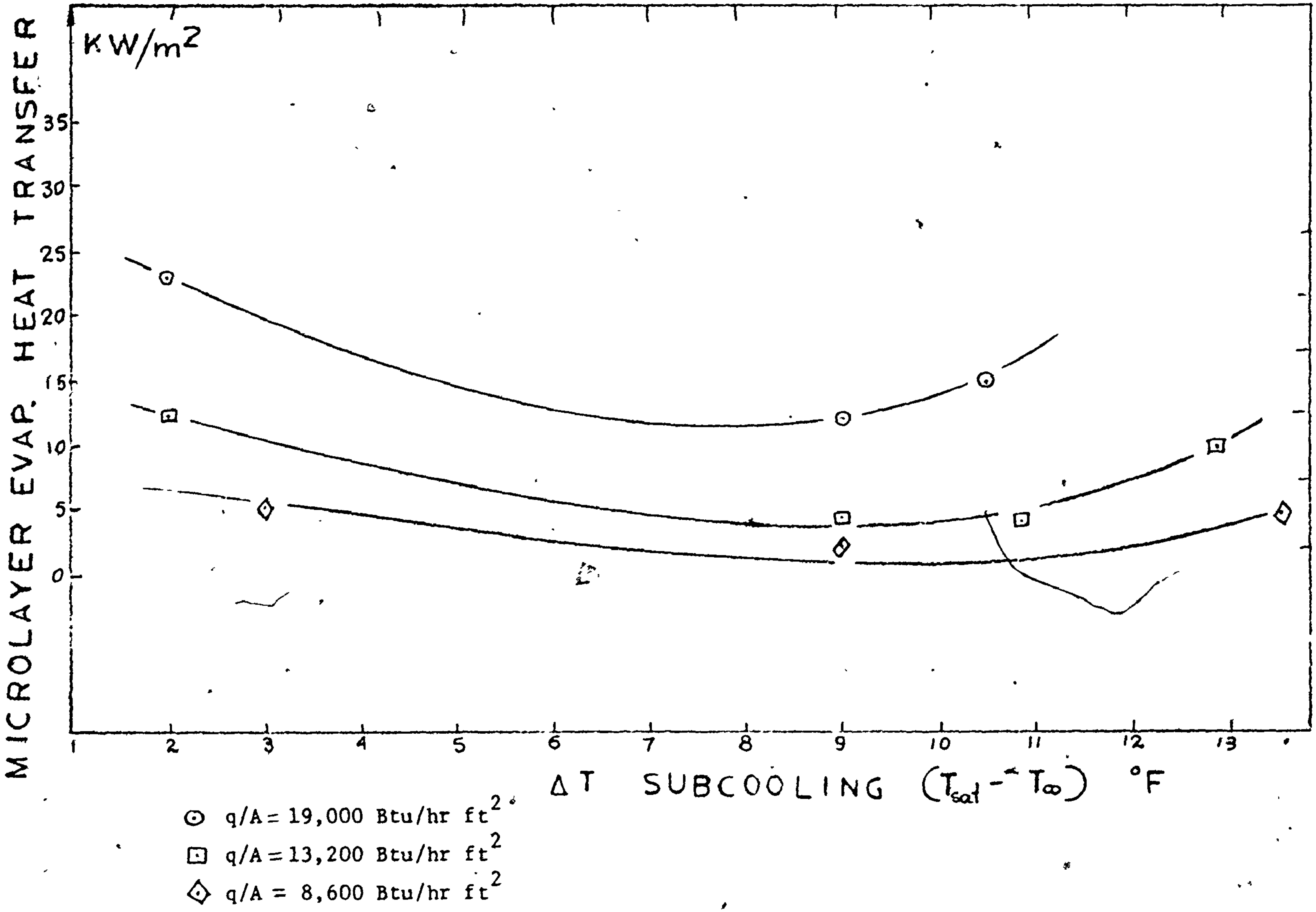

Figure 50 HEAT TRANSFERED BY MICROLAYER EVAPORATION

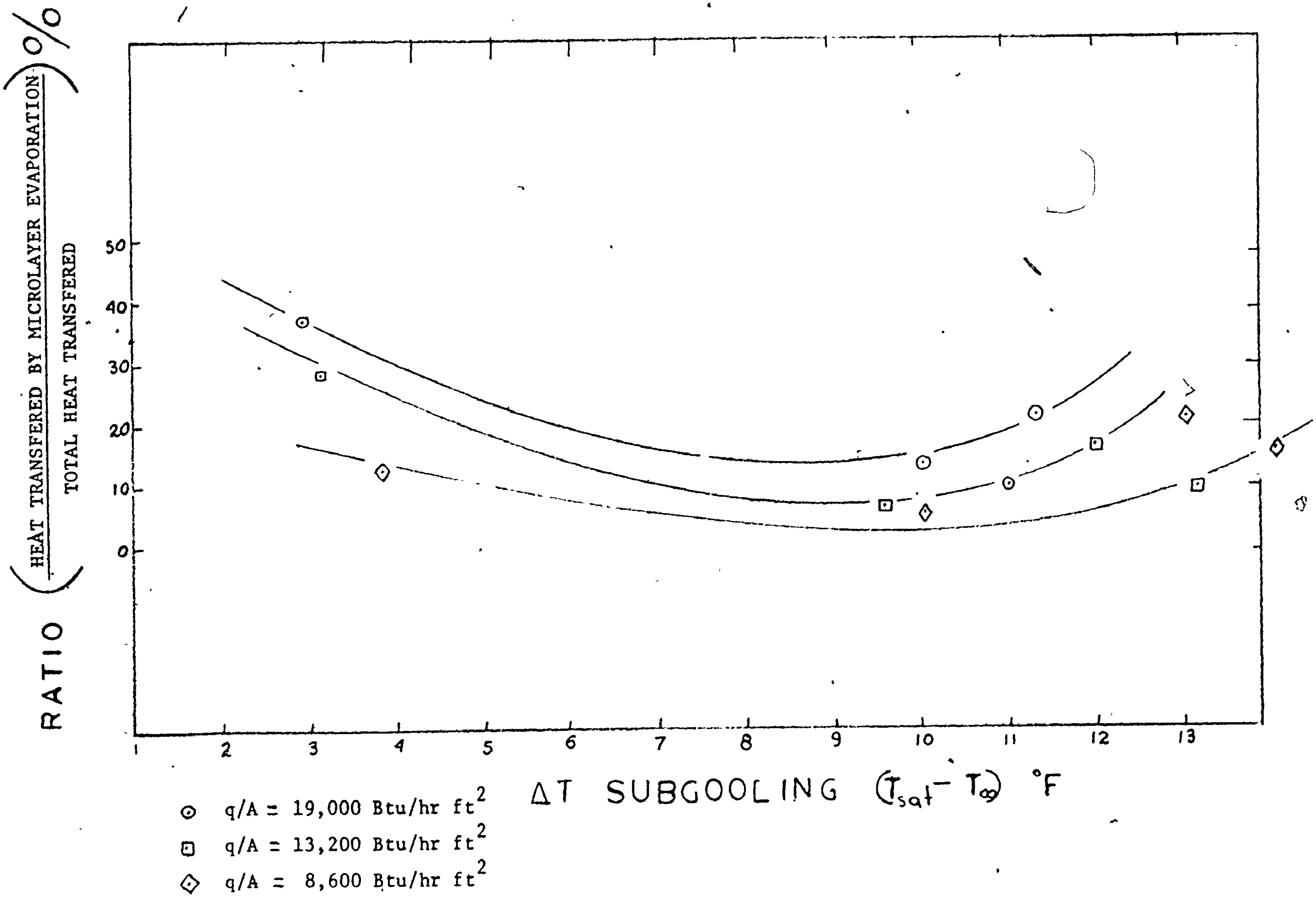

Figure 51 PERCENT OF HEAT TRANSFERED BY MICROLAYER EVAPORATION

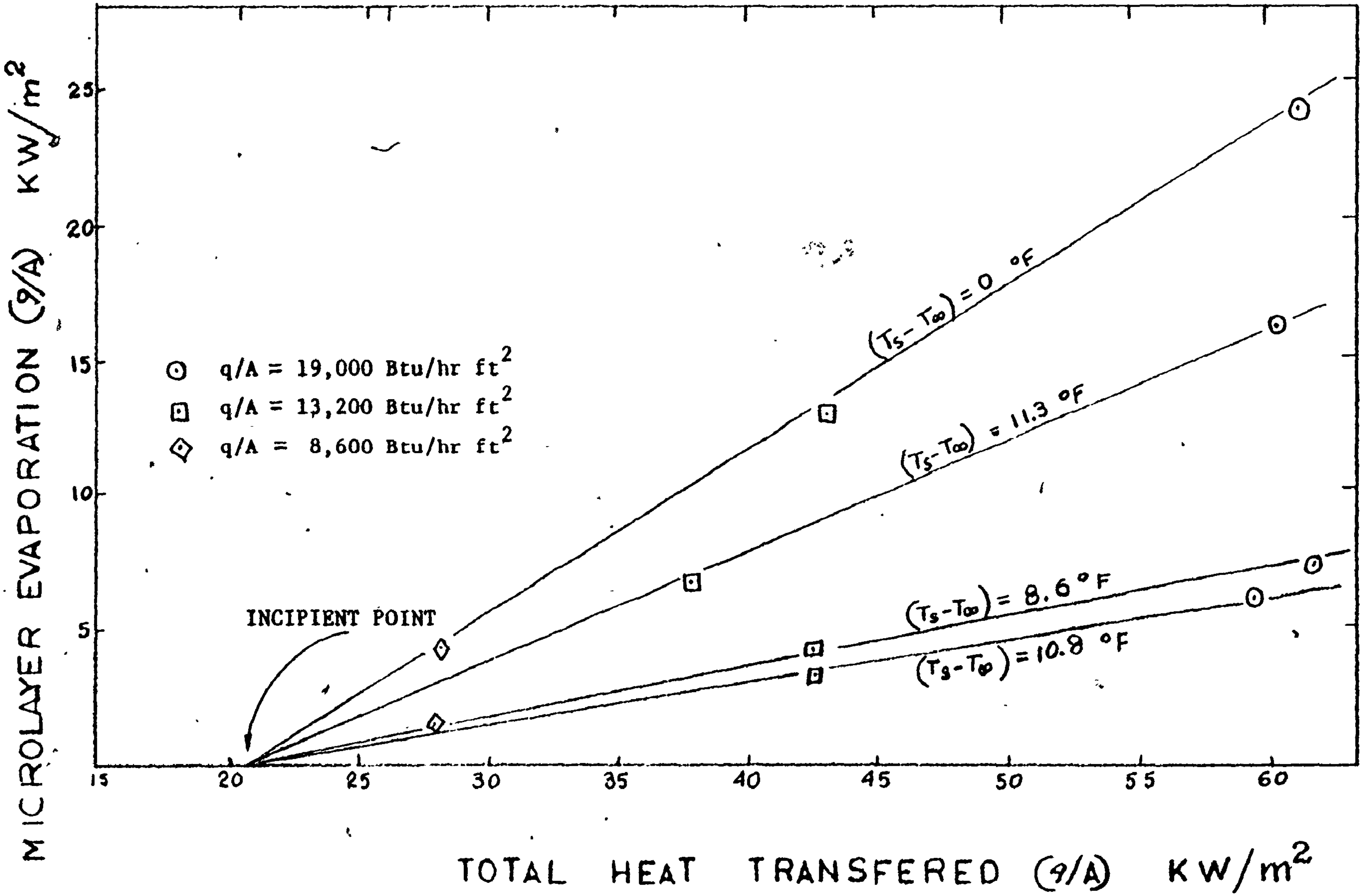

Figure 52 RATIO OF HEAT TRANSFERED BY MICROLAYER EVAPORATION vs. TOTAL HEAT TRANSFERED

CHAPTER VII

CHAPTER VII

DISCUSSION

A. Heat Transfer Results

The test procedure involving the establishment of reference test conditions before each run was explained previously. The purpose of this procedure was to obtain test results for the particular level of subcooling investigated. Figure 16 presented the two curves corresponding to minimum subcooling (i.e. Saturated boiling), and to maximum subcooling (i.e. $T_s - T_\infty$ = 13.5°F). For intermediate levels of subcooling the data points fall between the two plots.

The heat transfer results are essentially parallel to one another. The value of the slope in the Natural Convection region for both curves shown on Figure 16, depends entirely upon the physical parameters of the heated liquid and it may be verified as follows:

$$Nu = 0.16 \; (Pr \; Gr)^{1/3}$$

where by substituting the definitions for Nusselt and for Grashof numbers

$$\frac{hD}{k} = 0.16 \left[Pr \frac{g \beta \rho^2}{\mu^2} D^3 \; (T_w - T_\infty) \right]^{1/3}$$

hence $$q/A = 0.16 \left(Pr \frac{g \beta \rho^2}{\mu^2}\right)^{1/3} (T_w - T_\infty)^{4/3}$$

whereas by substituting fluid property values for dichloromethane evaluated at the saturation temperature, then

$$q/A = 22.6 \; (T_w - T_\infty)^{4/3} \quad Btu/hr\text{-}ft^2$$

Although the number of points are very few to be of significance, in Figure 17 the data contained illustrate that subcooling has a marked effect upon the superheat at constant heat flux. Also there may be noted that the value of superheat increases with increasing heat flu

The point at which the curve intersects the subcooling axes may be found as follows:

Superheat + Subcooling = Natural Convection

hence $$(Tw-Ts) + (Ts-T\infty) \cong \frac{(8600)^{3/4}}{22.6} = 86$$

B. Microlayer Evaporation Results

The profiles of the bubbles presented in Figures 18 to 29 are plotted from data obtained in the adjacent interferograms. It must be noted that the profile of the bubble cap is entirely conjectural since the depth of field of the optical system was such that only detail within the microlayer region would be visible. Occasional evidence of the cap was presented in the form of a secondary dark spot (interference) whenever a bubble was growing assymetrically. This illustrated in the second print of Figure 29. The initial growth rate was extremely rapid as evidenced by the blurred image in the first print of Figure 14. Careful examination of frames enlarged 100 times revealed the bubbles growth history in the form of interference fringes. Asymetry has commenced when the fringes are no longer concentric within the outline of the bubble. The broadening of the fringes seen in some figures is an indication of a decrease in the slope of the liquid-vapour interface. In all the prints presented, it is apparent that the dry spot beneath the bubble grows continually.

The results presented in Figure 30 demonstrate the influence of heat flux and subcooling upon the active site density. Although a small number of points were available, the curves plotted appear to have a tendency to decrease with increased subcooling. Also heat flux appears to have more influence on the active site density than subcooling.

The influence of heat flux and subcooling upon the frequency of vapour bubble emission has been illustrated in Figure 31. The curves presented show that the frequency of vapour bubble emission varies directly with heat flux and indirectly with subcooling. Decrease in frequency with increasing subcooling is explained by the fact that it takes longer periods of time for a bubble to reach departure size. The fact that the surface temperature and the temperature of the fluid adjacent, both increase with increasing heat flux, provide an explanation for the heat flux effects because bubbles grow more rapidly due to the enhancement of heat transfer in the boundary layer at the heat transfer surface. The plots shown in Figures 31 & 32 illustrate that there were no significant differences in the curves of bubble frequency (Bubbles/sec) and bubble flux density (Bubble/ft^2-sec), with heat flux when both were plotted vs subcooling

In the results presented in Figure 33 no attempt was made to indicate the influence which heat flux and subcooling may have had upon the maximum bubble size results. This is because effects due to varying heat flux were such that could not be distinguished from the uncertainty in the measurements obtained. Variation of subcooling levels indicated that a high percentage of bubbles reached a radius of 1.5mm for saturated boiling and for the maximum subcooling level investigated. On the other hand bubbles growing in the intermediate subcooling levels scarcely exceeded a radius of 1.1mm. These results however, may not necessarily be considered representative because of the relatively small samples available for examination.

The variations of the instantaneous microlayer thickness $\delta(r,t)$ were summarized in Figures 34 to 45. The numbers shown with each instantaneous microlayer profile indicate the elapsed time to the particular frame examined. Since each frame number corresponds to a time lapse of approximately 0.45 milliseconds, the development of the bubble's periphery, microlayer and dry spot may be obtained as a function of time. The bubbles depicted in these figures grew much faster at the initial stages as compared to the final. They all nucleated, reached departure size and detached in an averaged time lapse of 5.6 milliseconds.

The initial microlayer thickness $\delta_o(r)$ presented in figures 34 to 45 have been reproduced in figures 46, 47 and 48 for comparison. It is immediately apparent that for constant heat flux the microlayer thickness decreases with increased subcooling.

The discussion to this point has been concerned with the presentation of physical effects which have been observed or deduced from the results of the present investigation. The remainder of the discussion is directed towards the utilization of these results in order to obtain the percent contribution of the microlayer evaporation phenomenon to the total nucleate boiling heat transfer, for the various levels of subcooling and heat flux.

The volume of liquid evaporated from the microlayer in the time interval 0 to t is given by.

$$V_E = 2\pi \int_0^{R(t)} \left[\delta_o(r) - \delta(r,t) \right] r \, dr$$

It was calculated as a volume of revolution of the area between the initial microlayer thickness $\delta_o(r)$, the heater surface, and the last recorded instantaneous microlayer profile $\delta(r,\tau)$ at the instant of departure where $t = \tau$. Figure 49 presents the effect upon the volume evaporated by varying levels of subcooling and heat flux. Because the use of the volume of revolution method requires perfect symmetry, the most symmetric bubbles at the departure size were carefully selected, thus minimizing the error due to assymetric growth. Volume fluctuations due to varying heat flux were such that could not be distinguished from the uncertainty of the measurements obtained.

The contribution of the microlayer evaporation heat transfer to the nucleate boiling heat transfer process could be assessed once the validity of the initial microlayer profile had been established since the heat transferred may be computed by

$$\left(q/A \right)_{microlayer} = 2\pi \rho_l \, h_{fg} \, \frac{N}{A} \, f \int_0^{R(t)} \left[\delta_o(r) - \delta(r,\tau) \right] r \, dr$$

Figure 50 illustrates the effect exerted upon the microlayer evaporation heat transfer by the varying heat flux and levels of subcooling. The variation of these curves appear to be similar to the plots in figure 51 which show the percent contribution of the microlayer evaporation phenomenon to the total nucleate boiling heat transfer. Heat transferred by microlayer evaporation varies directly with heat flux. Its dependence however on the levels of subcooling indicate that there exist at least two interacting mechanisms causing the plots to decrease initially and then increase.

Finally the heat transferred by microlayer evaporation to the total heat transferred was illustrated in Figure 52. All of the curves plotted increase with increased heat supply. This is because an increase in heat flux causes an increase in bubble flux density which results in a direct increase in heat transferred by microlayer evaporation. As the heat supplied decreases the rate of heat transferred by microlayer evaporation approaches zero for all the plots which converge at the incipient point. As subcooling is increased from the saturated condition, microlayer evaporation heat transfer decreases. A minimum is reached and then microlayer evaporation begins to increase with increasing subcooling.

C H A P T E R   VIII

CHAPTER VIII

CONCLUSION

The results of the present investigation comprise a consistent set of measurements of microlayer thickness, active site density, frequency of vapour bubble emission and maximum bubble size pertaining to dichloromethane boiling on an oxide coated glass heating surface for various combinations of heat flux and subcooling.

The above results confirm that the microlayer evaporation phenomenon is a significant heat transfer mechanism. The relative significance of this mechanism to the nucleate boiling heat transfer process at the various levels of heat flux and subcooling examined, is summarized as follows:

a) Microlayer evaporation heat transfer increases directly with increased heat flux.

b) Microlayer evaporation heat transfer decreases originally with increased levels of subcooling, reaches a minimum and then increases again.

APPENDICES

A P P E N D I X   A

EXPERIMENTAL DATA

DATA FOR POINT (1, 1)

FILM DATA

L	Total film length.	3870	frames
η	Total film markings	183	dots
v	Marking frequency	100	dots/sec
n	Average number of frames	21.147	frames/dot
τ	Average time per frame	$0.473*10^{-3}$	secs/frame

POWER DATA

E	Voltage supplied	68	volts
I	Current supplied	1.52	amps
Q	Power sypplied	352.87	Btu/hr
A	Plate area	$1.82*10^{-2}$	ft^2
q/A	Power supplied per unit area	19,388.5	Btu/hr ft^2

THERMODYNAMIC DATA

T_w	Wall temperature	109.4	°F
T_∞	Bulk liquid temperature	68.0	°F
T_{sat}	Saturation temperature	69.9	°F
P_{sat}	Saturation pressure	14.0	in Hg
ΔT_{sub}	Subcooling temperature	1.9	°F
ΔT_{sup}	Superheat temperature	39.5	°F

BUBBLE DATA

F	Average number of frames between bubbles	60.4	frames
N	Number of active sites per frame	26	sites/frame
T	Average elapsed time between bubbles	0.0285	secs
f	Average bubble frequency	35	Bubbles/sec-site
φ	Bubble flux density	851,009	Bubbles/ft^2-sec

DATA FOR POINT (1 , 2)

FILM DATA

L	Total film length.	1231	frames
η	Total film markings	53	dots
v	Marking frequency	100	dots/sec
n	Average number of frames	23.226	frames/dot
τ	Average time per frame	$0.43*10^{-3}$	secs/frame

POWER DATA

E	Voltage supplied	69	volts
I	Current supplied	1.53	amps
Q	Power sypplied	360.4	Btu/hr
A	Plate area	$1.82*10^{-2}$	ft^2
q/A	Power supplied per unit area	19,803	Btu/hr ft^2

THERMODYNAMIC DATA

T_w	Wall temperature	108.2	°F
T_∞	Bulk liquid temperature	61.1	°F
T_{sat}	Saturation temperature	69.9	°F
P_{sat}	Saturation pressure	14.0	in Hg
ΔT_{sub}	Subcooling temperature	8.8	°F
ΔT_{sup}	Superheat temperature	38.3	°F

BUBBLE DATA

F	Average number of frames between bubbles	70.4	frames
N	Number of active sites per frame	26	sites/frame
T	Average elapsed time between bubbles	0.030	secs
f	Average bubble frequency	33	Bubbles/sec-site
Φ	Bubble flux density	802,380	Bubbles/ft^2-sec

DATA FOR POINT (1 , 3)

FILM DATA

L	Total film length.	1026	frames
η	Total film markings	44	dots
v	Marking frequency	100	dots/sec
n	Average number of frames	23.318	frames/dot
τ	Average time per frame	$0.428*10^{-3}$	secs/frame

POWER DATA

E	Voltage supplied	67	volts
I	Current supplied	1.51	amps
Q	Power sypplied	345.39	Btu/hr
A	Plate area	$1.82*10^{-2}$	ft^2
q/A	Power supplied per unit area	18,977	Btu/hr ft^2

THERMODYNAMIC DATA

T_w	Wall temperature	107.6	°F
T_∞	Bulk liquid temperature	59.9	°F
T_{sat}	Saturation temperature	69.9	°F
P_{sat}	Saturation pressure	14.0	in Hg
ΔT_{sub}	Subcooling temperature	10.0	°F
ΔT_{sup}	Superheat temperature	37.7	°F

BUBBLE DATA

F	Average number of frames between bubbles	80.5	frames
N	Number of active sites per frame	25	sites/frame
T	Average elapsed time between bubbles	0.0344	secs
f	Average bubble frequency	29	Bubbles/sec-site
φ	Bubble flux density	678,002	Bubbles/ft^2-sec.

DATA FOR POINT (1 , 4)

FILM DATA

L	Total film length.	1052	frames
η	Total film markings	46	dots
v	Marking frequency	100	dots/sec
n	Average number of frames	22.869	frames/dot
τ	Average time per frame	$0.437*10^{-3}$	secs/frame

POWER DATA

E	Voltage supplied	68	volts
I	Current supplied	1.51	amps
Q	Power sypplied	350.5	Btu/hr
A	Plate area	$1.82*10^{-2}$	ft^2
q/A	Power supplied per unit area	19,260	Btu/hr ft^2

THERMODYNAMIC DATA

T_w	Wall temperature	106.8	°F
T_∞	Bulk liquid temperature	56.65	°F
T_{sat}	Saturation temperature	69.90	°F
P_{sat}	Saturation pressure	14	in Hg
ΔT_{sub}	Subcooling temperature	10.3	°F
ΔT_{sup}	Superheat temperature	36.9	°F

BUBBLE DATA

F	Average number of frames between bubbles	70.5	frames
N	Number of active sites per frame	26	sites/frame
T	Average elapsed time between bubbles	0.0333	secs
f	Average bubble frequency	30	Bubbles/sec-site
φ	Bubble flux density	729,436	Bubbles/ft^2-sec

DATA FOR POINT (2 , 1)

FILM DATA

L	Total film length.	3814	frames
η	Total film markings	180	dots
v	Marking frequency	100	dots/sec
n	Average number of frames	21.188	frames/dot
τ	Average time per frame	$0.472*10^{-3}$	secs/frame

POWER DATA

E	Voltage supplied	56	volts
I	Current supplied	1.29	amps
Q	Power sypplied	246.6	Btu/hr
A	Plate area	$1.82*10^{-2}$	ft^2
q/A	Power supplied per unit area	13,550.9	Btu/hr ft^2

THERMODYNAMIC DATA

T_w	Wall temperature	107.9	°F
T_∞	Bulk liquid temperature	67.8	°F
T_{sat}	Saturation temperature	69.9	°F
P_{sat}	Saturation pressure	14	in Hg
ΔT_{sub}	Subcooling temperature	2.1	°F
ΔT_{sup}	Superheat temperature	38.0	°F

BUBBLE DATA

F	Average number of frames between bubbles	75.6	frames
N	Number of active sites per frame	23	sites/frame
T	Average elapsed time between bubbles	0.035	secs
f	Average bubble frequency	28	Bubbles/sec-site
φ	Bubble flux density	602,253	Bubbles/ft^2-sec

DATA FOR POINT (2 , 2)

FILM DATA

L	Total film length.	929	frames
η	Total film markings	44	dots
v	Marking frequency	100	dots/sec
n	Average number of frames	21.136	frames/dot
τ	Average time per frame	$0.473*10^{-3}$	secs/frame

POWER DATA

E	Voltage supplied	56	volts
I	Current supplied	1.28	amps
Q	Power sypplied	244.7	Btu/hr
A	Plate area	$1.82*10^{-2}$	ft^2
q/A	Power supplied per unit area	13,446	Btu/hr ft^2

THERMODYNAMIC DATA

T_w	Wall temperature	106.8	°F
T_∞	Bulk liquid temperature	61.7	°F
T_{sat}	Saturation temperature	69.9	°F
P_{sat}	Saturation pressure	14.0	in Hg
ΔT_{sub}	Subcooling temperature	8.2	°F
ΔT_{sup}	Superheat temperature	36.9	°F

BUBBLE DATA

F	Average number of frames between bubbles	81.314	frames
N	Number of active sites per frame	14	sites/frame
T	Average elapsed time between bubbles	0.0384	secs
f	Average bubble frequency	26	Bubbles/sec-site
φ	Bubble flux density	340,403	Bubbles/ft^2-sec

DATA FOR POINT (2, 3)

FILM DATA

L	Total film length.	1089	frames
η	Total film markings	48	dots
v	Marking frequency	100	dots/sec
n	Average number of frames	22.687	frames/dot
τ	Average time per frame	$0.440 * 10^{-3}$	secs/frame

POWER DATA

E	Voltage supplied	56	volts
I	Current supplied	1.28	amps
Q	Power sypplied	244.7	Btu/hr
A	Plate area	$1.82 * 10^{-2}$	ft^2
q/A	Power supplied per unit area	13,446	Btu/hr ft^2

THERMODYNAMIC DATA

T_w	Wall temperature	107.4	°F
T_∞	Bulk liquid temperature	59.2	°F
T_{sat}	Saturation temperature	69.9	°F
P_{sat}	Saturation pressure	14	in Hg
ΔT_{sub}	Subcooling temperature	10.7	°F
ΔT_{sup}	Superheat temperature	37.5	°F

BUBBLE DATA

F	Average number of frames between bubbles	119.6	frames
N	Number of active sites per frame	14	sites/frame
T	Average elapsed time between bubbles	0.052	secs
f	Average bubble frequency	19	Bubbles/sec-site
φ	Bubble flux density	248,756	Bubbles/ft^2-sec

DATA FOR POINT (2 , 4)

FILM DATA

L	Total film length.	1035	frames
η	Total film markings	46	dots
v	Marking frequency	100	dots/sec
n	Average number of frames	22.500	frames/dot
τ	Average time per frame	$0.444*10^{-3}$	secs/frame

POWER DATA

E	Voltage supplied	45	volts
I	Current supplied	1.01	amps
Q	Power sypplied	155.1	Btu/hr
A	Plate area	$1.82*10^{-2}$	ft^2
q/A	Power supplied per unit area	11,923	Btu/hr ft^2

THERMODYNAMIC DATA

T_w	Wall temperature	106.5	°F
T_∞	Bulk liquid temperature	57.6	°F
T_{sat}	Saturation temperature	69.9	°F
P_{sat}	Saturation pressure	14	in Hg
ΔT_{sub}	Subcooling temperature	12.3	°F
ΔT_{sup}	Superheat temperature	36.6	°F

BUBBLE DATA

F	Average number of frames between bubbles	97.92	frames
N	Number of active sites per frame	9	sites/frame
T	Average elapsed time between bubbles	0.0434	secs
f	Average bubble frequency	23	Bubbles/sec-site
Φ	Bubble flux density	193,581	Bubbles/ft^2-sec

DATA FOR POINT (3, 1)

FILM DATA

L	Total film length.	3757	frames
η	Total film markings	175	dots
v	Marking frequency	100	dots/sec
n	Average number of frames	21.468	frames/dot
τ	Average time per frame	$0.65*10^{-3}$	secs/frame

POWER DATA

E	Voltage supplied	46	volts
I	Current supplied	1.04	amps
Q	Power sypplied	163.3	Btu/hr
A	Plate area	$1.82*10^{-2}$	ft^2
q/A	Power supplied per unit area	8,974	Btu/hr ft^2

THERMODYNAMIC DATA

T_w	Wall temperature	106.5	°F
T_∞	Bulk liquid temperature	67.1	°F
T_{sat}	Saturation temperature	69.9	°F
P_{sat}	Saturation pressure	14	in Hg
ΔT_{sub}	Subcooling temperature	2.8	°F
ΔT_{sup}	Superheat temperature	36.6	°F

BUBBLE DATA

F	Average number of frames between bubbles	93.5	frames
N	Number of active sites per frame	7	sites/frame
T	Average elapsed time between bubbles	0.0434	secs
f	Average bubble frequency	23	Bubbles/sec-site
φ	Bubble flux density	150,563	Bubbles/ft^2-sec

DATA FOR POINT (3 , 2)

FILM DATA

L	Total film length.	1243	frames
η	Total film markings	57	dots
v	Marking frequency	100	dots/sec
n	Average number of frames	21.807	frames/dot
τ	Average time per frame	$0.458*10^{-3}$	secs/frame

POWER DATA

E	Voltage supplied	46	volts
I	Current supplied	1.02	amps
Q	Power sypplied	160.18	Btu/hr
A	Plate area	$1.82*10^{-2}$	ft^2
q/A	Power supplied per unit area	8,801	Btu/hr ft^2

THERMODYNAMIC DATA

T_w	Wall temperature	107.6	°F
T_∞	Bulk liquid temperature	60.9	°F
T_{sat}	Saturation temperature	69.9	°F
P_{sat}	Saturation pressure	14.0	in Hg
ΔT_{sub}	Subcooling temperature	9707	°F
ΔT_{sup}	Superheat temperature		°F

BUBBLE DATA

F	Average number of frames between bubbles	94.93	frames
N	Number of active sites per frame	6	sites/frame
T	Average elapsed time between bubbles	0.0434	secs
f	Average bubble frequency	23	Bubbles/sec-site
Φ	Bubble flux density	129,054	Bubbles/ft^2-sec

DATA FOR POINT (3 , 3)

FILM DATA

L	Total film length.	1125	frames
η	Total film markings	51	dots
v	Marking frequency	100	dots/sec
n	Average number of frames	22.058	frames/dot
τ	Average time per frame	$0.453*10^{-3}$	secs/frame

POWER DATA

E	Voltage supplied	46	volts
I	Current supplied	1.02	amps
Q	Power sypplied	160.1	Btu/hr
A	Plate area	$1.82*10^{-2}$	ft^2
q/A	Power supplied per unit area	8,801	Btu/hr ft^2

THERMODYNAMIC DATA

T_w	Wall temperature	105.0	°F
T_∞	Bulk liquid temperature	57.9	°F
T_{sat}	Saturation temperature	69.9	°F
P_{sat}	Saturation pressure	14.0	in Hg
ΔT_{sub}	Subcooling temperature	12.0	°F
ΔT_{sup}	Superheat temperature	35.1	°F

BUBBLE DATA

F	Average number of frames between bubbles	95.9	frames
N	Number of active sites per frame	7	sites/frame
T	Average elapsed time between bubbles	0.0434	secs
f	Average bubble frequency	23	Bubbles/sec-site
Φ	Bubble flux density	150,563	Bubbles/ft^2-sec

DATA FOR POINT (3 , 4)

FILM DATA

L	Total film length.	1093	frames
η	Total film markings	50	dots
v	Marking frequency	100	dots/sec
n	Average number of frames	21.860	frames/dot
τ	Average time per frame	$0.45*10^{-3}$	secs/frame

POWER DATA

E	Voltage supplied	36	volts
I	Current supplied	0.8	amps
Q	Power sypplied	98.32	Btu/hr
A	Plate area	$1.82*10^{-2}$	ft^2
q/A	Power supplied per unit area	5,402	Btu/hr ft^2

THERMODYNAMIC DATA

T_w	Wall temperature	100.9	°F
T_∞	Bulk liquid temperature	56.5	°F
T_{sat}	Saturation temperature	69.9	°F
P_{sat}	Saturation pressure	14.0	in Hg
ΔT_{sub}	Subcooling temperature	13.4	°F
ΔT_{sup}	Superheat temperature	31.0	°F

BUBBLE DATA

F	Average number of frames between bubbles	95.1	frames
N	Number of active sites per frame	4	sites/frame
T	Average elapsed time between bubbles	0.0343	secs
f	Average bubble frequency	23	Bubbles/sec-site
Φ	Bubble flux density	86,036	Bubbles/ft^2-sec

A P P E N D I X B.

BUBBLE FREQUENCY HISTOGRAMS

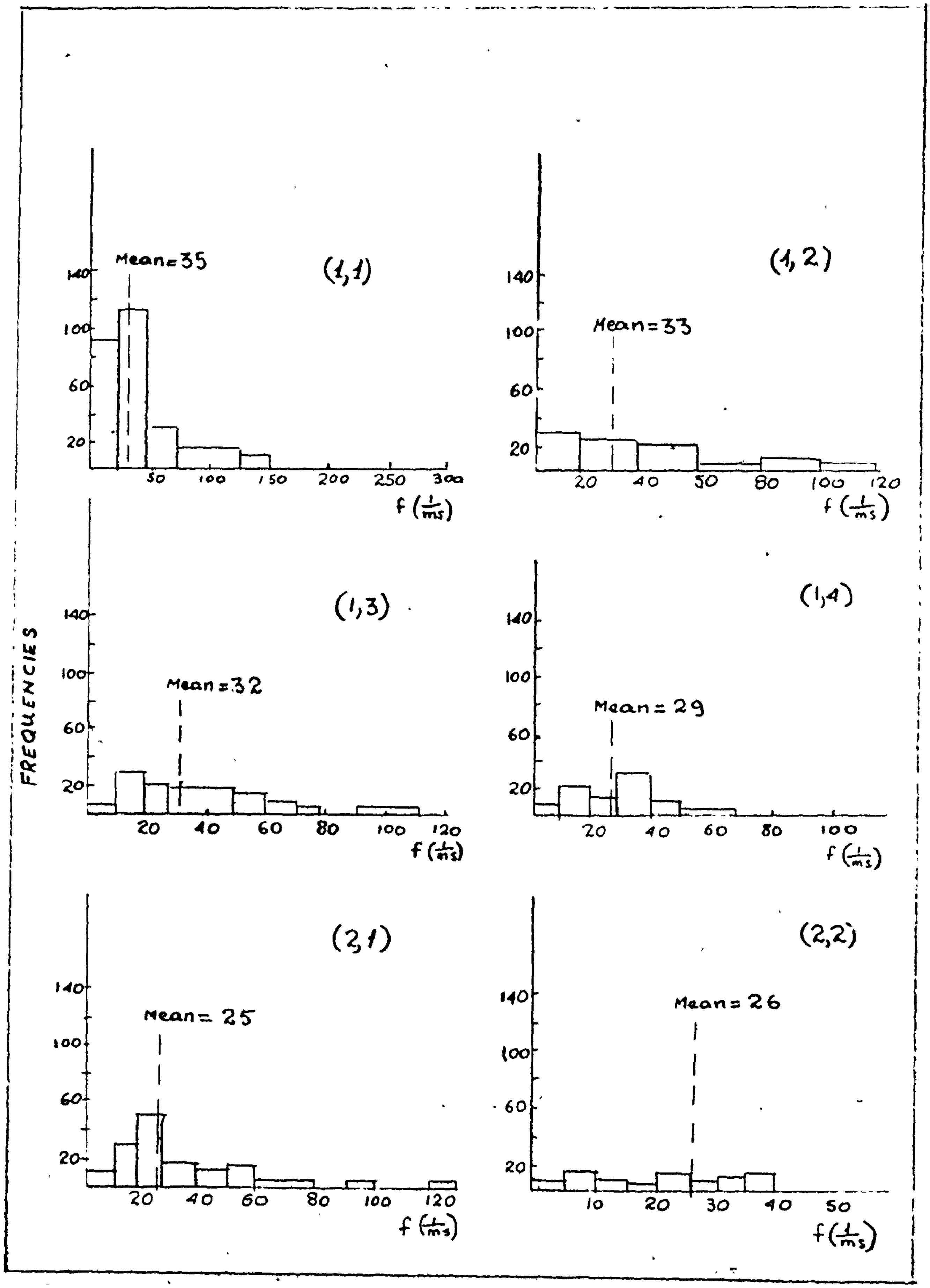
FREQUENCIES
(1,1)
Mean=35
140
100
60
20
50 100 150 200 250 300
f (1/ms)
(1,2)
Mean=33
140
100
60
20
20 40 50 80 100 120
f (1/ms)
(1,3)
Mean=32
140
100
60
20
20 40 60 80 100 120
f (1/ms)
(1,4)
Mean= 29
140
100
60
20
20 40 60 80 100
f (1/ms)
(2,1)
Mean= 25
140
100
60
20
20 40 60 80 100 120
f (1/ms)
(2,2)
Mean= 26
140
100
60
20
10 20 30 40 50
f (1/ms)

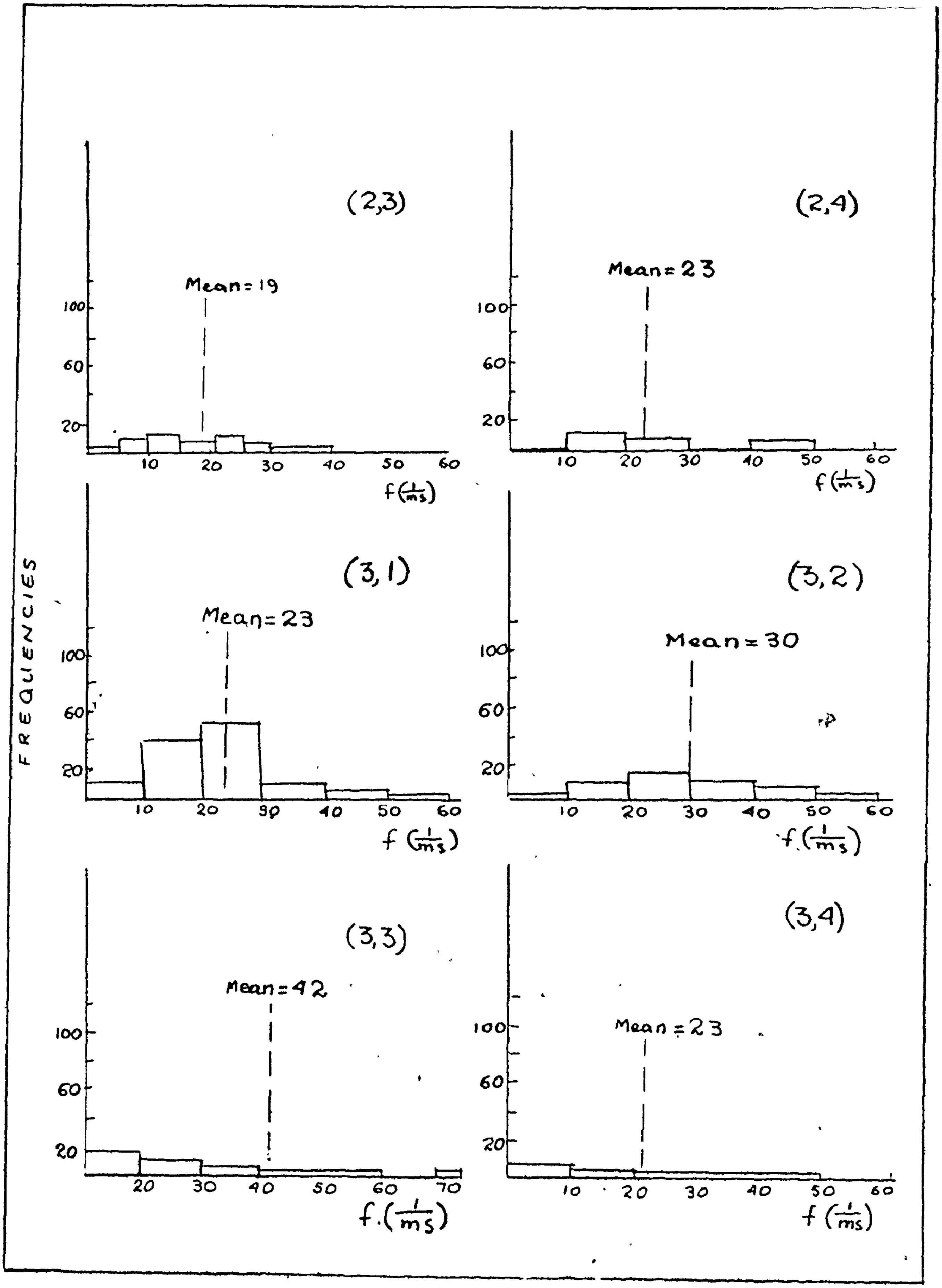

FREQUENCIES
(2,3)
Mean=19
(2,4)
Mean=23
(3,1)
Mean=23
(3,2)
Mean=30
(3,3)
Mean=42
(3,4)
Mean=23
$f\left(\frac{1}{ms}\right)$

A P P E N D I X C.

VOLUMES OF REVOLUTION

TABLE 3

VOLUMES OF REVOLUTION

		Subcooling Levels			
		1	2	3	4
Heat Flux Levels	1	1.245	0.412	0.393	0.955
	2	0.908	0.437	0.584	1.602
	3	1.180	0.578	1.868	1.525

The values contained in the above matrix are the volumes of microlayer liquid evaporated into the bubble in $ft^3 * 10^9$, given by the relationship:

$$V_E = 2\pi \int_0^{R(t)} \left(\delta_o(r) - \delta(r,\tau) \right) r \, dr$$

BIBLIOGRAPHY

1. Judd R.L. and Merte Jr. H. "Evaluation of Nucleate Boiling Heat Flux Predictions at Varying Levels of Subcooling and Acceleration", Int. Journal Heat Mass Transfer 15, 1972.

2. Snyder N.R. and Edwards D.K. "Post Conference Comments". Summary of Conference on Bubble Dynamics and Boiling Heat Transfer Held at the Jet Propulsion Laboratory, June 14, and 15, 1956. California Inst. Tech., Dec. 10, 1956 P. 38.

3. Moore F.D. and Mesler "The Measurement of Rapid Surface Temperature Fluctuations During Nucleate Boiling of Water", A.I.Ch.E. Journal 7, 1961.

4. Hendricks R.C. and Sharp R.R. "Initiation of Cooling Due to Bubble Growth On a Heating Surgace", N.A.S.A. TN D-2990, 1964.

5. Rogers T.F. and Mesler R.B. "An Experimental Study of Surface Cooling By Bubbles During Nucleate Boiling Of Water", A.I.Ch.E. Journal, Sept. 1964.

6. Sharp R.R. "The Nature Of Liquid Film Evaporating During Nucleate Boiling", N.A.S.A. TN D-1997, 1964.

7. Cooper M.G. and Lloyd A.J.L. "The Microlayer in Nucleate Pool Boiling", Int. Journal Heat Mass Transfer, 12, 1969.

8. Jawurek H.H. "Simultaneous Determination of Microlayer Geometry and Bubble Growth in Nucleate Boiling", Int. Journal Heat Mass Tranfer, 12, 1969.

9. Dzakowic G.S. and Frost W. "An Analytical Solution for the Transient Temperature of a Heated Surface During Microlayer Evaporation", A.S.M.E. 67-WA/HT-21.

10. Olander R.R. and Watts R.G. "An Analytical Expression of Microlayer Thickness in Nucleate Boiling", A.S.M.E. Trans., Journal of Heat Transfer 91, 1969.

11. Cooper M.G. and Lloyd A.J.P. "Transient Local Heat Flux in Nucleate Boiling", Proceedings, International Heat Transfer Conference 1966.

12. Robin Jr. T.T. and Snyder N.W. "Bubble Dynamics in Subcooled Nucleate Boiling Based on the Mass Transfer Mechanism", Int. Journal Heat Mass Transfer 13, 1970.

13. Judd R.L. "Influence of Acceleration on Subcooled Nucleate Boiling", Doctorate Thesis, University of Michigan 1968.

14. Judd and Voutsinos "Laser Inferomatic investigation of the microlayer Evaporation Phenomenon". ASME Trans. Journal of Heat Transfer 97, 1975.

15. National Bureau of Standards, "Reference Tables for Thermocouples", N.B.S. Publication Number 561, 1955.